Microscopic and Macroscopic Spin Current Phenomena

Benedict Andrew Murphy

Doctor of Philosophy

University of York

Physics

April 2016

Abstract

Spintronics is the field concerned with the control of electron spin. In logic devices electron charge is manipulated, in computer data storage the magnetisation of a domain is altered; spintronics offers a hybrid between the two. This could be exploited in non-volatile random access memory cells for low power data storage.

All-metal Lateral spin-valve devices were fabricated by electron beam lithography to investigate spin transport phenomena. The fabrication and measurement processes were optimised and lateral spin-valve devices were successfully fabricated with spin diffusion lengths of (200$\pm$25) nm and (310$\pm$30) nm in 100 nm and 200 nm wide Copper wires respectively. Spin filtering was previously observed by patterning nano-scale wires to be laterally asymmetric. Here, nano-scale wires were patterned to have a laterally symmetric spin diffusion path. No increase in signal due to the filtering effect was observed, thus confirming the phenomenological model put forward. Also, the spin diffusion path in a lateral spin valve was split into a ring geometry. By applying a field gradient across the ring, the operational efficiency was improved by 30%.

The observation of a mechanically induced spin current has been achieved for the first time. The design of an optical measurement system that rotates a sample at up to 200 Hz is presented here. Deviation in the moment on the surface of a paramagnetic Tungsten foil from the moment induced by the Barnett effect confirms that a spin current may be induced by mechanical rotation.

In summary, design and development of magneto-electrical and mechano-optical measurement systems has been achieved. The improvement in the operational efficiency in lateral spin-valves could be used alongside materials such as Heusler alloys to provide cheaper efficient logic devices. The observation of a mechanically induced spin current in Tungsten precedes the future study of the effect in other paramagnetic materials, such as Platinum or Palladium.

Contents

List of Tables

List of Figures

Acknowledgements

To thank everybody who has contributed and supported this work would take too long; to thank only a few would do many an injustice. Nonetheless, I would like to thank: Professor Kevin O'Grady for his experienced guidance, generosity and, of course, his wealth of anecdotes; Professor Atsufumi Hirohata for imparting a minor fraction of his excellent technical and physical knowledge to me; Dr. Andrew Vick for the many useful discussions surrounding this work and for fabricating the majority of the devices; Dr. Marjan Samiepour for her advice and device fabrication; Dr. Ranjdar Abdullah for his contributions to the electrical measurement development; Ryo Arakawa, Benny Ng, Yunqi Yao and Yuji Baba for their assistance in taking mechano-optical measurements; David Coulthard (MBE) and all other members of research services for their practical suggestions, without which this work would have been impossible; Brent Wilkinson and all of the staff in the mechanical workshop for their excellent skills in manufacturing precision components and advice in mechanical design.

On a personal level I would like to thank those around me for their support and patience. Finally I would like to thank all past and present members of the Magnetic Materials and Quantum Nanoelectronics research groups for their scientific and, of course, social input; to all future members, good luck!

This project was funded by JEOL UK and EPSRC grant number EP/I000933/1.

Declaration

I declare that the work presented in this thesis is based purely on my own research, unless otherwise stated, and has not been submitted for a degree in either this or any other university.

Papers published:

R. M. Abdullah, A. J. Vick, B. A. Murphy, and A. Hirohata, "Spin-current signal amplification by a geometrical ratchet," J. Phys. D: Appl. Phys., vol. 47, no. 48, p. 482001, 2014.

R. M. Abdullah, A. J. Vick, B. A. Murphy, and A. Hirohata, "Optimisation of geometrical ratchets for spin-current amplification," J. Appl. Phys., vol. 117, no. 17, 2015.

A. Hirohata, Y. Yamamoto, B. A. Murphy and A. J. Vick, "Non-destructive imaging of buried electronic interfaces using a decelerated scanning electron beam," Nature Commun., vol. 7, no. 12701, 2016.

B. A. Murphy, A. J. Vick, M. Samiepour and A. Hirohata, "Highly efficient spin-current operation in a Cu nano-ring," Sci. Rep., *in press*.

Chapter 1

Introduction

The study of spin transport phenomena is concerned with the field of spintronics (a portmanteau of spin transport electronics) that has emerged over the past twenty-five years. Specifically, spintronics is the study of an electron's intrinsic spin angular momentum and how this couples with its other properties. Spintronics is a field of research where technology that could be disruptive in many device industries is being developed. Well-established electronic phenomena, such as the Hall and Seebeck effects [1, 2] tend to have corollaries within the area of spintronics [3, 4] that could be used in: logic devices for computer processing; spin-valves in small scale magnetic sensors; oscillators in wireless communications and nano and micrometric heat sensors to name but a few. More closely related to this work, spintronics could provide a potential substitute in the form of magnetic random access memory, MRAM, for contemporary devices such as dynamic random access memory, DRAM, and static random access memory, SRAM. In this vein, this work is concerned with aspects of magnetoelectronics: the coupling between magnetism and its influence on electron spins in otherwise spin-neutral metallic materials.

Spin dependent transport behaviour has been a well-documented phenomenon. The founding discoveries in spintronics were the discovery of anisotropic magneto-resistance, AMR, by W. Thompson and Baron Kelvin [5] and the observation of the anomalous Hall effect by E. J. Hall [1]. These were the first observations of spin dependent behaviour in electric currents. With regards to the origin of spin, the link between magnetism and its connection to angular momentum was first put forward by Richardson [6] and the theory formalised by A. Einstein and W. J. de Haas [7]. The discoveries by Thompson and Hall were the first observations of the properties that make electronic spin a useful characteristic in electronic devices and the works by Richardson, Einstein and de Haas went some way to understanding the physical origin of the intrinsic angular momentum

known as an electron spin. This thesis is split into two parts that follow these themes. Firstly, an investigation into the fundamental side of electron spin generation and secondly, the application of electron spin phenomena into working nano-scale devices. The title of the thesis is given by the scale of the samples used to investigate these topics.

1.1 Microscopic spin currents

From the discovery of anisotropic magneto-resistance (AMR) by Thompson [5] to the first observation of the anomalous Hall effect by Hall [1]. Spin transport has contributed much to technology, in particular the data storage industry in read head sensors in hard drives. Anisotropic magneto-resistance [5] was the key parameter of read heads in hard disk drives until 1997 when giant magneto-resistance (GMR), discovered contemporaneously by A. Fert and P. Grünberg [8, 9], took over. These were the first demonstrations of spintronic devices with commercial utility. It has been a longer struggle for magneto-resistive random access memory, MRAM, which was first proposed as a potential radiation stable random access memory by Honeywell International Inc. in the mid-1980s. Following this, the need for improved data density was the driving force for the research behind logic and data storage. As this race has continued the frequency of fundamental issues due to the decrease in feature sizes has increased. The issues facing manufacturers as the bit-scale reduces include leakage current mechanisms [10] and cross-talk issues, where, for example, conventional current driven magnetisation reversal in MRAM could generate a large enough Oersted field to rewrite a neighbouring bit. These issues seem to provide a fundamental lower limit to bit size but could be overcome if alternative methods were used in place of conventional current driven methods to control the magnetisation states, *e.g.* electric-field driven and strain-controlled magnetisation [11, 12].

The discovery by Fert and Grünberg of GMR in multilayered films that were used later as spin-valves was not the first observation of spin dependent transport between spin-polarising layers. Their discovery was predated by Johnson and Silsbee [13]. The principle of operation between the two is similar. A ferromagnetic layer of some kind polarises an electron current passing into a metal. In the Johnson and Silsbee case, the electrons was taken from a relaxed and equilibrium state into a non-equilibrium state where there was an increase in density of one of the spin states. Accompanying the increase in density of one spin state was an equal decrease in the other spin state. These changes in density cause the diffusion of electrons following Fick's law [14] and due to the symmetry of the spin densities, *i.e.* they compensate, there is no net flow of charge. The spin imbalance can be subsequently detected at an analysing ferromagnetic layer in

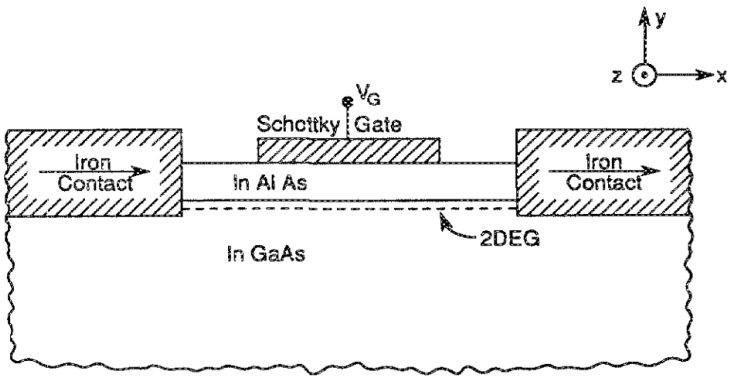

Figure 1.1: The electronic analogue of an electro-optic modulator proposed by Datta and Das [15].

the manner outlined by Datta and Das [15] by switching the magnetisation direction of the analysing layer. Here, they suggested that ferromagnetic iron contacts would work as polarisers and analysers of electrons, as shown in figure 1.1. The measurement that first observed this was made by Johnson and Silsbee and is shown in figure 1.2.

The measurement in figure 1.2 shows the voltage induced by the spin-imbalance at the analyser. This remains constant, in a "1" state, until the analyser magnetisation reverses. Then the voltage drops to a "0" state. As the field continues to change, the polarising magnetisation reverses and the voltage reverts back to the same "1" state voltage. Accurate and reproducible control of the magnetisation states of the polariser and analyser could lend these devices to being useful logic devices, as has already been mentioned. The GMR spin valve works in the same way but with the addition of a drift electron current. In the right configuration the magnetisation states in these types of devices could be stable with no power applied. This is the great advantage that spintronic devices hold over complimentary metal-oxide-semiconductor (CMOS) devices. CMOS devices require much greater power consumption due to the requirement of a "static" source of power as well as a source of power to switch states from "1" to "0". However,

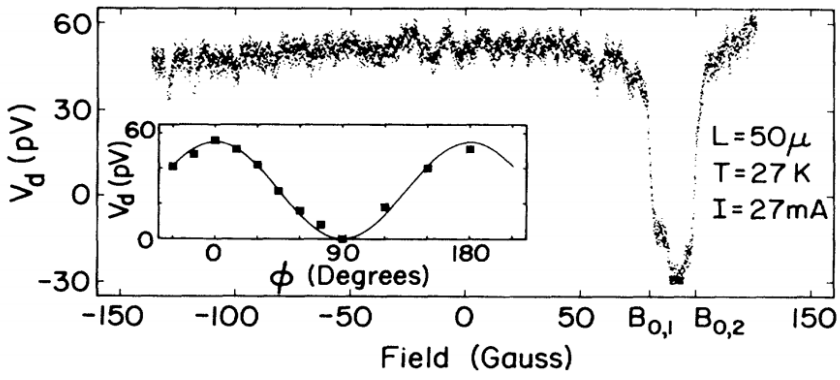

Figure 1.2: The original measurement published by Johnson and Silsbee [13].

one of the significant obstacles facing spintronic devices are the current injection and operation efficiencies. Spin injection efficiency in this manner is typically three orders of magnitude lower in systems with an accompanying charge current between the polarising and analysing layers [16].

For this first part of the thesis nanoscale fabrication methods were employed to investigate application based spintronic effects on the sub-micron scale.

1.2 Macroscopic spin currents

Spin angular momentum is an "intrinsic" quality. There is no mechanical motion to the particle that imparts this quality. However, we know that magnetism is closely related to angular momentum in form. There were two experiments that occurred over a similar period of time that proved the existence of coupling between angular momentum from mechanical rotation and the magnetic-moment angular momentum. In 1908 O. W. Richardson suggested that an object, such as an iron bar, suddenly imparted with a change in magnetisation should undergo a corresponding change in angular momentum [6]. The inverse of the effect was observed by S. Barnett, where the magnetisation of a rotating rod was observed to increase by an amount proportional to its mechanical rotation [17]. The effect was later further worked upon by Einstein and de Haas [7]. The effect of magnetisation by rotation is therefore known as the Einstein-de Haas effect, the Barnett effect (for magnetisation induced by rotation) or the Richardson effect (for rotation induced by magnetisation).

As already suggested there are often analogues of electric effects in spin systems.

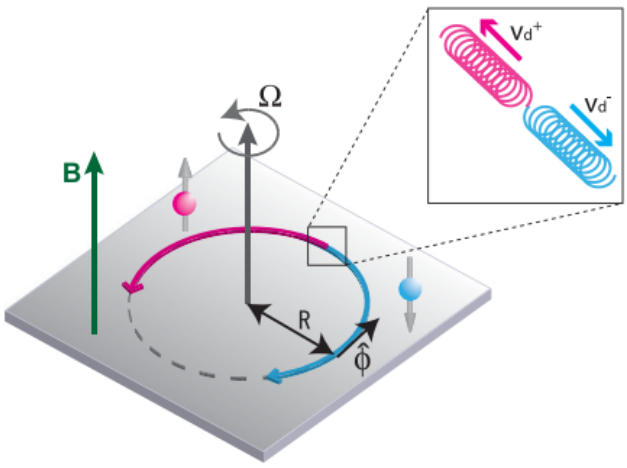

Figure 1.3: Pt foil in a rotating frame [18].

Does such an analogue exist from this magnetic phenomenon? Recently, Matsuo *et al.* predicted that it should be possible to excite a spin current in a material by rotating it [18,19] as shown in figure 1.3. They suggested that a spin current would be generated in a material based on the electric field that would be induced due to general-relativistic effects. This would generate a spin current through the spin Hall effect [20,21]. Although this spin current would not be generated through a direct coupling between rotation and the electron spin, it perhaps goes some way to explaining the nature of the spin-orbit coupling strength factor, a dimensionless quantity that relates the spin of an electron to its momentum and therefore the magnitude of the spin current generated by the Spin Hall effect [22].

As yet though, this phenomenon remains experimentally unobserved. Efforts are being made by several research groups to observe this effect. Most notably, the observation of the Barnett effect in powdered ^{29}Si and ^{115}In was achieved using nuclear magnetic resonance at up to 10 kHz [23]. However, despite the advantages of this experimental setup, this method has yet to yield a measure of the spin current induced in conduction electrons in a rotating system. Some progress has been made in observing the mechanical induction of a spin current by other means. The same group published work on the hydrodynamic generation of a spin current [24]. In this case a spin current was induced transverse to the flow of Mercury. This was the first observation of the generation of a spin current by mechanical motion.

Although an obvious on-chip application for the generation of a spin current by mechanical rotation may not be apparent, the proof that such a phenomenon exists would confirm our current understanding of spin-transport phenomena which could lead to further understanding of its origin. For this second part of the thesis, mechanical rotation methods were used to observe the generation of a spin current across a macroscopic metallic sample.

In summary, the objectives of this work were in two parts and subsequently this thesis is split into two parts to reflect this. The objectives were to:

- Investigate the electron diffusion and find, if possible, a way of enhancing the operation of spintronic devices to overcome the issue of injection efficiency;
- Develop a measurement system for the observation of a spin current induced by mechanical rotation in order to confirm the latest understanding of electron spin dynamics.

1.3 Notes on units and errors

Both the c.g.s. and S.I. systems of units are commonplace in the area of spintronics due to its overlap with the magnetic recording industry, that uses c.g.s., and semiconductor spintronics, that uses S.I.. In this thesis the c.g.s. unit system has been adopted for all equations, calculations and values. There are, however, some instances where the work has more of an overlap with fundamental Physics where the S.I. system has been adopted due to its predominance. For the most-part c.g.s. units have been used and results have been converted to c.g.s.. However, on occasion S.I. units have been used, for example in the reproduction of graphs and diagrams from other works.

Where possible the errors quoted for numerical data have been calculated using standard Gaussian error techniques [25]. Where values from the literature are quoted without error, the data was initially quoted without error and the error is unknown.

Part I

Microscopic spin current phenomena

Chapter 2

Electron spin

The structure and content of this chapter follows the relevant information from "Spin Current" edited by Maekawa *et al.* [26]. Overviews of some of the methods that are used for the generation of electron spin are covered in this chapter. The methods and fundamentals that are covered are not restricted to those used in this work.

As discussed in chapter 1, the advantage of using electron spin angular momentum as a degree of freedom rather than charge is the relatively weak interaction that electron spin experiences with its surroundings. The ratio of the transport relaxation time to the spin-flip relaxation time has been found to be of the order of 10^3 at liquid Helium temperature [27]. The relaxation lifetime that it experiences makes spin angular momentum an ideal "1" or "0" in a transistor-like device. Therefore, the dynamics of a spin and the method by which it couples with its surroundings is important for future spintronic devices. Covered in this chapter are the methods by which a spin angular momentum signal may be enhanced, manipulated or used to manipulate another structure. These topics define the functionality of the devices that have been investigated. All of the discussion in this section refers to non-local device geometry. In a non-local measurement a voltage is probed remotely from the driving current. In this study currents are applied to ferromagnetic/non-magnetic interface to inject a spin-imbalance into the non-magnet. The injecting current is drawn off in one direction and the spin-imbalance diffuses away in all directions in the absence of any electron drift current. The spin-imbalance can be detected at some distance away as a voltage at a second ferromagnetic/non-magnetic interface. The non-local geometry is described in more detail in section 2.2.5.

2.1 Principles of electron spin

Angular momentum is a strange quantity on the quantum mechanical level. Electrons have an extrinsic orbital and an intrinsic spin angular momentum. The orbital angular momentum can be thought of as the motion of the electron. The electron spin angular momentum is an intrinsic quality with two opposing states of the same magnitude: spin "up" and spin "down". An analogy for the spin angular momentum would be of a charged sphere rotating about its own axis in one direction or the other. In a solid state material the orbital and spin angular momenta sum to form a total electron angular momentum giving rise to a total dipole moment. In materials with a low atomic number, $<$30, the spin-orbit interaction is much weaker than the spin-spin interaction of neighbouring spins. Therefore, the total angular momentum of neighbouring conduction electron spins is approximated as the sum of the electron spin angular momentum by the Russell-Saunders interaction [28]. In the case of the nanoscale electronic devices that are measured in this work, the material investigated was Copper, having an atomic number of 29.

2.1.1 The spin degree of freedom

The spin degree of freedom is defined as an intrinsic angular momentum. The origin of this is unknown. However, through experimentation and with the existing formalism for electron angular momentum it can be described. The spin magnetic moment is given by [29]

$$\mu_{\mathrm{S}} = -\frac{q_{\mathrm{e}}}{2m_{\mathrm{e}}} gS \tag{2.1}$$

where q_{e} is the electronic charge, m_{e} is the electron rest mass and g is the Landé electron spin g-factor. Spin angular momentum, S, is defined as $S = \hbar\sqrt{s(s+1)}$ where the spin quantum number for an electron has a magnitude of $1/2$ with a positive or negative sign. S, the total spin angular momentum, is a combination of the x, y and z spin angular momentum components, $s_{x/y/z}$. The quantum number for an electron was determined to be non-integer in a number of experiments, notably by Stern and Gerlach [30]. Here, the application of an external magnetic field splits an electron beam into two components in the azimuthal direction of the experimental layout. If the quantum number were integer, three lines would have been observed for the s = 1, 0 and -1 states. The presence of two lines confirmed that s is non-integer, *i.e.* $1/2$. S is therefore equal to $\frac{\sqrt{3}}{2}\hbar$, where $\hbar$ is Planck's constant. For ease the spin magnetic moment is generally expressed as a

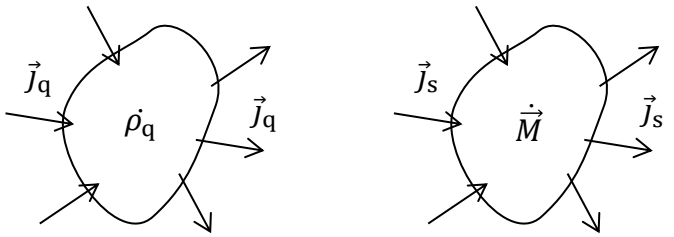

(a) (b)

Figure 2.1: An element depicting (a) charge continuity and (b) magnetisation continuity.

multiple of the Bohr magneton [31].

$$\mu_{\mathrm{B}} = \frac{q_{\mathrm{e}}\hbar}{2m_{\mathrm{e}}} \tag{2.2}$$

It is the transfer and movement of this angular momentum with which this work is concerned.

2.1.2 Defining spin current

A spin current can be formalised in the same way as a charge current. A charged region enclosed by a surface follows the charge conservation law. Any alteration to the total charge of a volume within an enclosed surface is due to the transit of charged particles or a flow of current across the surface.

$$\dot{\rho_{\mathrm{q}}} = -\nabla \cdot \mathbf{j}_{\mathrm{q}}\,, \tag{2.3}$$

where ρ_{q} is the charge density and j_{q} is the charge current density through the surface enclosing the charge distribution, shown in figure 2.1(a). In the same way that the total charge is conserved, so is the total angular momentum. The incomplete continuity equation for spin angular momentum can be written as

$$\dot{\mathbf{M}} = -\nabla \cdot \mathbf{j}_{\mathrm{s}}\,, \tag{2.4}$$

where $\dot{\mathbf{M}}$ is the change in magnetisation or magnetic-moment density and j_{s} is the spin current density, shown in figure 2.1(b). It should be noted, however, that the angular momentum is rarely wholly conserved due to spin relaxation. As a result a non-conserving

spin relaxation term is added to the end of the continuity equation.

$$\dot{\mathbf{M}} = -\nabla \cdot \mathbf{j}_{\mathrm{s}} - \frac{\mathbf{M} - \mathbf{M}_0}{\tau_{\mathrm{S}}}\,, \tag{2.5}$$

where $\mathbf{M}_0$ is the equilibrium magnetisation. A spin polarised current has two components, a charge flow and a spin polarisation so equations (2.3) and (2.4) should be combined when considering spin-electron dynamics.

Hence a spin polarised current is defined using the same laws that govern a charge current. However, there are a number of mechanisms that in analogy to a charge current act as additional or scattering potentials. As well as the extra spin relaxation term added to equation (2.4) there are other interactions, such as spin-orbit interactions that will affect the spin-dynamics.

2.1.3 The two-channel model for spin currents

A conventional current is a flow of charge with the absence of any overall spin polarisation. This will be referred to as a charge current. It was found by Matthiessen in 1864 [32] that resistivities due to impurities sum independently in metals, *i.e.* a metal with impurities "a" and "b" added to it has a resistivity given by

$$\rho = \rho_0 + \rho_{\mathrm{a}} + \rho_{\mathrm{b}} \tag{2.6}$$

and that the temperature dependent components of resisitivty behave in the same way, where ρ_0 is the intrinsic resistivity of the material and $\rho_{\mathrm{a,b}}$ is the resistivity due to the addition of impurities "a" and "b". Based on the Mott two current model [33], there are two half bands of opposing spin that behave similarly to two parallel current channels within any charge current. The proof for this was the observation that ferromagnetic, F, transition metals do not obey Matthiessen's law [34]. The spin channels are modelled as two conductors in parallel with different spin-relaxation times, $\tau_{\mathrm{S}\uparrow}$ and $\tau_{\mathrm{S}\downarrow}$, for spin up and spin down that define the spin dependent conductivity for each current channel. In addition there are spin-flip and electron-electron interaction processes that are characterised by an inter-channel spin-relaxation time $\tau_{\mathrm{S}\uparrow\downarrow}$ [35]. At low temperature the total resistivity for two opposing spin current channels sum as

$$\frac{1}{\rho(0)} = \frac{1}{\rho_{\uparrow}(0)} + \frac{1}{\rho_{\downarrow}(0)} \tag{2.7}$$

or

$$\rho(0) = \frac{\rho_{\uparrow}(0)\rho_{\downarrow}(0)}{\rho_{\uparrow}(0) + \rho_{\downarrow}(0)}\,. \tag{2.8}$$

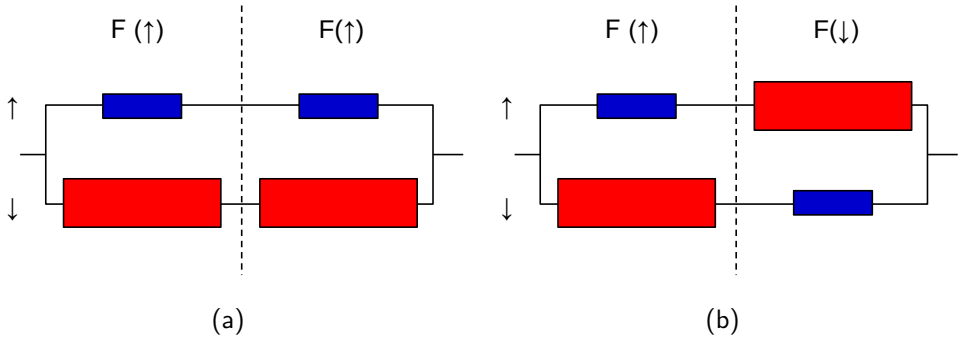

Figure 2.2: Two-channel model for ferromagnetic/ferromagnetic conductors aligned (a) parallel and (b) anti-parallel. The intermediate non-magnetic layer is not included in the schematic.

As the temperature increases the spin-flip scattering increases so a temperature dependent term and an inter-channel term are added for each channel. Spin-flip scattering events fall into two categories: those where momentum is conserved and those where it is not. Momentum-conserving scattering events are included in the additional inter-channel resistivity whereas non-conserving spin-flip events are included in the thermal term [34].

Following the seminal work by Mott [33, 36] and the subsequent work by Campbell and Fert [34, 35] the Boltzmann equations for electron transport are solved for the two channels and combined for the two current channels to give

$$\rho = \frac{\rho_{\uparrow}\rho_{\downarrow} + \rho_{\uparrow\downarrow}(\rho_{\uparrow} + \rho_{\downarrow})}{\rho_{\uparrow} + \rho_{\downarrow} + 4\rho_{\uparrow\downarrow}} \tag{2.9}$$

where ρ is the resistivity.

For a material like Cu the resistances of the two spin channels are equal. F metals, however, do not have an equal resistance for the two channels. In fact the difference in resistance for F transition metals is large owing to the presence of partly filled *d*-bands into which the electrons scatter [37]. For this system to be modelled as two independent spin channels the spin-flip scattering cross section ($\propto 1/\tau_{S\uparrow\downarrow}$) must also be low. The difference in spin dependent resistance for F transition metals is exploited in giant magneto-resistance (GMR) spin-valves. The simplest example of a GMR spin-valve is given by two transition metal F layers separated by a non-magnetic, NM, metallic conductor. Depending upon the induced magnetisation of the F layers a stack of such layers will have a resistance that can be described by figure 2.2.

For the sake of argument, consider a current passed perpendicular to the plane of the F and NM layers. Initially non-polarised, the current becomes spin polarised as it

passes through the first F layer. The current retains its polarisation through the NM layer and then enters the second F layer. If the magnetisation of the second layer is anti-parallel (AP) to the first layer, the scattering cross section is much increased due to the presence of the unfilled *d*-band that act as scattering sites. The resistor network for such a system is shown in figure 2.2(b). In the anti-parallel case the resistance for each channel is the same. Therefore for the two channels together the resistance due to this AP configuration is given by [37]

$$R^{\mathrm{AP}}_{\mathrm{total}} = \frac{R^{\mathrm{P}}_{\uparrow} + R^{\mathrm{P}}_{\downarrow}}{4}\,, \tag{2.10}$$

where $R^{\mathrm{P}}_{\uparrow,\downarrow}$ is the resistance for the majority/minority spin channel through the GMR stack when aligned parallel. For the parallel (P) case the resistance is [37]

$$R^{\mathrm{P}}_{\mathrm{total}} = \frac{R^{\mathrm{P}}_{\uparrow} R^{\mathrm{P}}_{\downarrow}}{R^{\mathrm{P}}_{\uparrow} + R^{\mathrm{P}}_{\downarrow}}\,. \tag{2.11}$$

Equations (2.10) and (2.11) are combined to give

$$\mathrm{GMR} = \frac{R_{\mathrm{AP}} - R_{\mathrm{P}}}{R_{\mathrm{P}}} = \frac{(R^{\mathrm{P}}_{\downarrow} - R^{\mathrm{P}}_{\uparrow})^2}{4R^{\mathrm{P}}_{\downarrow} R^{\mathrm{P}}_{\uparrow}} \tag{2.12}$$

where R_{AP} is the anti-parallel resistance of the GMR stack and R_{P} is the parallel resistance. It is obvious from equation (2.12) that to maximise the GMR ratio the difference between the minority and majority spin channel resistance should be maximised.

2.1.4 Spin-wave current

There are four fundamental states of magnetic response. These magnetic orderings originate from the electron band structure and the exchange energy between neighbouring atomic sites.

1. Diamagnetism arises from complete spin compensation. All of the electrons fill the bands in spin pairs. The magnetisation of a diamagnetic material is anti-parallel with an applied magnetic field. In analogy with Lenz's law the electron orbitals change slightly to oppose the applied magnetic field in the classical model. All materials are diamagnetic, however, the response is exceedingly small, of the order of 10^{-6} cm^3/g in water for example.

2. Paramagnetism is a result of partially filled bands. Therefore, there is a spin imbalance per atomic site. The magnetisation of a paramagnetic material aligns

parallel with an applied magnetic field. Whilst there is a fixed moment on an atom there is no innate magnetisation due to thermal disorder.

3. Ferromagnetism has the same spin imbalance observed in paramagnetic materials. However, in this case an exchange energy described by Heisenberg's Hamiltonian

$$\mathcal{H} = -J_{\mathrm{ex}} \sum s_{\mathrm{i}} \cdot s_{\mathrm{j}} \tag{2.13}$$

where J_{ex} is the exchange energy coefficient and $s_{\mathrm{i/j}}$ is the spin operator of an atom at position i/j. For the F case $J_{\mathrm{ex}} > 0$ so the energy of the system is minimised by the parallel alignment of neighbouring atomic moments.

4. Antiferromagnetic materials also arise from uncompensated spins generally in the *d*- or *f*-band which is partially filled. However, the exchange energy coefficient for AF materials is negative, $J_{\mathrm{ex}} <$0, and so the anti-parallel alignment of neighbouring sites is preferred.

In the same way that the exchange energy in equation (2.13) determines the alignment of the atomic moments in F and AF materials, it will also affect the alignment of overlapping electron spins. This can cause collective electron spin behaviour, a spin current carried by a spin wave. To begin with the Hamiltonian for a lone spin under the effect of a magnetic field only can be written as

$$\mathcal{H} = -\mathbf{M} \cdot \mathbf{H}_{\mathrm{eff}} \,, \tag{2.14}$$

where M is the magnetisation and H is the field strength. This simply says that to minimise the energy the spin moment aligns with the applied magnetic field direction. The magnetisation of two neighbouring spins follows the standard commutation relation for angular momentum. Combining this with the Heisenberg equation of motion, the following is obtained,

$$\frac{dM}{dt} = \gamma \mathbf{M} \times \mathbf{H} \,, \tag{2.15}$$

where γ is the gyromagnetic ratio. Equation (2.15) describes the motion of the electron spin. In an applied field a spin will precess around the magnetisation and gradually relax into an equilibrium position where it is aligned. The rate at which this energy minimum is achieved is determined by local conditions, such as other localised magnetic moments in the vicinity.

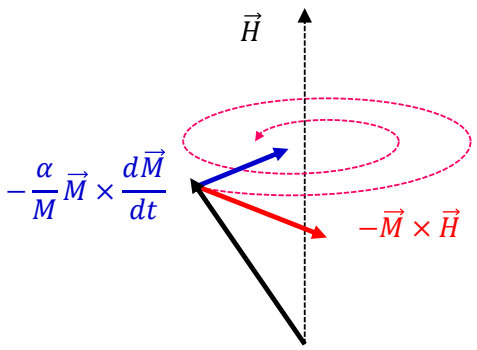

Figure 2.3: Magnetic damping due to the LLG equation.

To describe this relaxation mathematically the Gilbert term is added to the equation of motion for the electron, and so equation (2.15) becomes

$$\frac{dM}{dt} = \gamma \mathbf{M} \times \mathbf{H} + \frac{\alpha_0}{M} \mathbf{M} \times \frac{d\mathbf{M}}{dt}\,, \tag{2.16}$$

where α_0 is a dimensionless damping constant. Equation (2.16) is known as the Landau-Lifshitz-Gilbert (LLG) equation. Terms acting on a precessing spin moment are shown in figure 2.3. It can be shown that for a ferromagnetic interaction, *i.e.* $J_{\mathrm{ex}} > 0$, in the application of a steady state field does indeed give rise to F alignment [26].

The significance of the LLG equation is that in the F coupling case the angular momentum can be passed between neighbouring spins as a spin wave or magnon. For the simple situation where only the immediate neighbour has any effects upon a spin, the Hamiltonian is written as

$$\mathcal{H} = -2J_{\mathrm{ex}} \sum_{\langle \mathrm{i,j} \rangle} \mathbf{s}_{\mathrm{i}} \cdot \mathbf{s}_{\mathrm{j}} - g\mu_{\mathrm{B}} H \sum_{i} s_{\mathrm{i}z}\,. \tag{2.17}$$

Here g is the Landé g-factor, μ_{B} the Bohr magneton and $s_{\mathrm{i}z}$ is the i'th azimuthal spin component (s_z). This representation defines the fundamental mathematics that causes a spin wave to move through a system of interacting spins. This spin wave carries angular momentum, proven experimentally by the detection of this spin wave in even an F insulator [38].

2.1.5 Spin-transfer torque

Spin-transfer torque (STT) must be considered for a spin current that is passing through a sample in which there are discontinuities or non-uniformities in the spin-angular momentum. This occurs in a number of systems when packets of electron angular momen-

tum are moving through regions of alternating magnetism due to physical or magnetic structural effects. In the case where two magnetic layers with opposing magnetisations have a current applied the magnetisation of the first layer acts as a filter and a spin polarised current enters the second layer. If the magnetisation and the spin angular momentum are not co-linear then the magnetised body absorbs some of the spin angular momentum carried by the current. A torque is applied to the vector of the spin-angular momentum packet, and so necessarily an equal and opposite torque is applied to the magnetised body it is passing through [39]. An additional term needs to be applied to equation (2.16) to account for this effect upon the spin dynamics.

2.2 Generation, injection and detection

2.2.1 Application of a magnetic field

By far the most direct way to introduce a spin polarisation into a material is by the application of a magnetic field. The simple valence band picture for a material like Nickel depicts the density of states for the 3*d* and 4*s* shells. The 4*s* shell, shown in figure 2.4(a), is much narrower and initially spin balanced. The 3*d* shell has uncompensated spins and is depicted as being much broader. Upon the application of a magnetic field, more electrons populate the spin-polarisation state aligned with the magnetic field as shown in figure 2.4(b). However, the spin majority conduction channel is not necessarily the same spin channel as dominates the magnetisation. The spin majority is the channel that has the highest density of states at the Fermi level. This need not only occur in ferromagnetic materials of course, the application of a magnetic field will also introduce

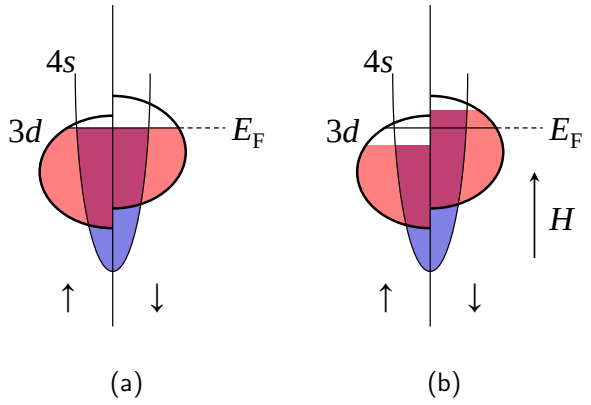

Figure 2.4: Bulk valence band diagrams for (a) zero applied field and (b) non-zero applied field.

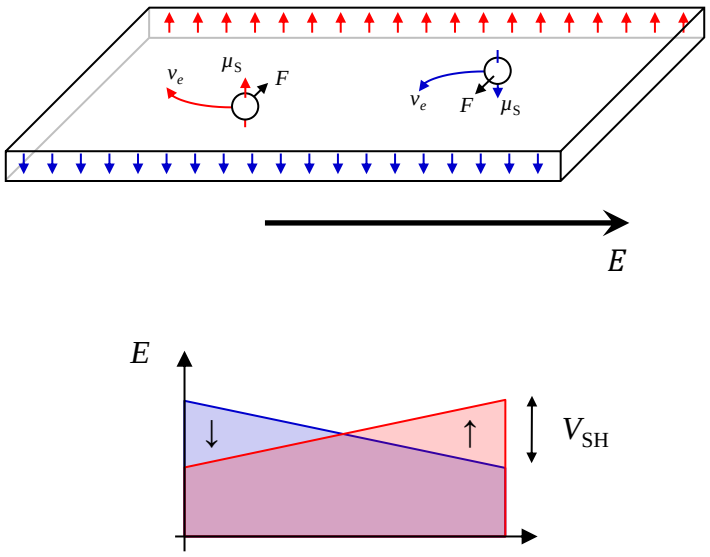

Figure 2.5: Spin Hall effect due to an applied electric field with the spin dependent potential across the element, adapted from ref. [21].

spin polarised electrons to a non-magnetic material [40].

2.2.2 Application of an electric field

The application of an electric field in a material induces what is known as the spin Hall effect. In fact, the spin Hall effect arises from the same mechanisms that cause the anomalous Hall effect in F metals, first observed in 1881 by Hall [1]. It was first predicted to occur in semiconductors in the seminal work by Dyakanov and Perel in 1971 [20], and observed optically by Kato *et al.* in 2004 [3]. With the spin Hall effect electrons of an opposite spin are subject to opposing transverse forces and so a spin splitting is observed as shown in figure 2.5.

The extrinsic spin Hall effect is due to side-jump and Mott skew scattering mechanisms [27]. These occur at non-magnetic impurities which gives rise to local electric fields $\mathbf{E} = (1/q_e)\nabla u(\mathbf{r})$ where q_e is the electronic charge and u is the potential due the impurity. An electron passing through the vicinity of the impurity feels an effective field

$$\mathbf{B}_{\text{eff.}} = -\frac{1}{m_e c}\hat{\mathbf{p}} \times \mathbf{E}\,, \tag{2.18}$$

where m_e is the mass of the electron, c is the speed of light in a vacuum, $\hat{\mathbf{p}}$ is the momentum operator and $\mathbf{E}$ is the electric field. This gives a spin-dependent angle of scattering in the system. Additionally in a scattering event where there is some

momentum exchange, a side jump mechanism provides a transfer of momentum in the transverse direction as shown in the element in figure 2.5. There is therefore a resulting spin-dependent motive force upon the electrons, causing them to move in opposite directions. As a result a gradient in the chemical potential for each spin is produced, shown to the left of figure 2.5. The strength with which this occurs is governed by the phenomenological spin-orbit coupling constant, η_{SO}.

The gradient of the spin density can be measured as a voltage in ferromagnetic materials as there is already a native spin polarisation. However, in materials where there is no innate spin polarisation the voltage difference for each spin channel cancels. The spin polarisation can be probed by using a ferromagnetic detector circuit as described later in section 2.2.5 or by optical means. The first observation by optical means was by Kato *et al.* [3] where the surface of a 77 µm $\times$ 300 µm Gallium arsenide mesa was probed with a linearly polarised laser beam. An alternating E-field was applied for lock-in detection and the field swept to induce a Hanle effect for spin density observation. The spatial spin-density plot showed clearly a separation of spins perpendicular to the applied E-field.

2.2.3 Application of a thermal gradient

Spin caloritronics is the control of spin currents with thermoelectric currents and the reverse. This area is of interest due to the thermodynamic limit of nano-electronic devices, where Joule heating threatens to destroy progress in semiconductor and metal logic devices. As with the application of an electric field (above in section 2.2.2), there are many coupling mechanisms between electron spin, charge and heat [41].

Of particular relevance is the injection of a pure spin current into a metal lateral spin-valve [42]. Here, an F material was exploited to inject a spin current into an adjacent NM material in a similar geometry to that conventionally used for electrical injection, discussed later in section 2.2.5 and chapter 4. Heat driven spin diffusion is observed in the NM channel. In keeping with the two-channel model for conduction the Seebeck coefficient, $C_{\mathrm{S}(\uparrow/\downarrow)}$, is spin dependent in an F material. The spin current in the F and NM is described by

$$j_{\mathrm{S}(\uparrow/\downarrow)} = -\frac{1}{\rho_{\uparrow/\downarrow}}\left(\frac{1}{e}\nabla\mu_{\uparrow/\downarrow} + C_{\mathrm{S}(\uparrow/\downarrow)}\nabla T\right), \tag{2.19}$$

where the spin dependent quantities are denoted by j_{S} for the current density, $\rho_{\uparrow/\downarrow}$ for the resistivity, $\mu_{\uparrow/\downarrow}$ for the chemical potential and T is the temperature.

2.2.4 Optically induced spin polarisation

Optically induced spin-polarisation occurs in semiconductors by photo-excitation. Photo-excitation is the application of an exciting photon wave-packet to promote an electron from one state to another. The energy (wavelength) of the wave-packet needs to be matched to the band-gap of the semiconductor. Spin-polarised electron-hole pairs are produced and can be detected as an electrical signal [43]. A direct band gap semiconductor such as Gallium arsenide has a band gap of 1.43 eV at room temperature corresponding to the Planck-Einstein relationship to a wavelength of 867 nm. The valence band electrons splits into ℓ =2 degenerate fourfold $P_{3/2}$ and twofold $P_{1/2}$ states. The conduction band splits into ℓ =1 twofold degenerate $S_{1/2}$ states as shown in figure 2.6. Photo-excitation occurs when the selection rule $\Delta m_j = \pm 1$ is satisfied. Producing spin-polarised electron-hole pairs is simply a case of matching the energy gap and applying a right handed, σ^+, or left handed, σ^-, circularly polarised light, illustrated in figure 2.6.

Semiconductors have been extensively studied in optically operated spintronic systems due to the large typical spin diffusion lengths of 2 μm in Gallium arsenide [44] and the ease therefore of optically pumping such a device. The reciprocity of the photo-excitation effect was observed by Fiederling *et al.* and Ohno *et al.* in 1999 [45,46]. However, the diffusion lengths in metals are typically an order of magnitude smaller [47–49]. Optically induced spin polarisation in metal systems generally falls under the study of electron dynamics in pump-probe experiments.

In a pump-probe experiment a short, typically at or below the picosecond timescale is applied to a material. The optical absorption of the pulsed light causes intense local heating, but their main effect is still photo-excitation. The dissipation of this heat is governed by electron-electron interactions, and hence the electron transport properties of a material can be investigated by this method.

A magneto-optical interaction that does not result in heating of the surrounding medium is the inverse Faraday effect, where a static magnetisation $\mathbf{M}$ is induced in a material by the application of an oscillating external field

$$\mathbf{M} = \frac{\chi_{\mathrm{O}}}{16\pi}[\mathbf{E}(f) \times \mathbf{E}^{\star}(f)] \tag{2.20}$$

where χ_{O} is the magneto-optical susceptibility of the material, $\mathbf{E}$ is the electric field and $\mathbf{E}^{\star}$ its complex conjugate. It was shown by Kimel *et al.* [50] that the local magnetisation of a material could be altered by the application of a circularly polarised light pulse and that as equation (2.20) indicates the handedness of the polarisation determined the direction of the induced magnetisation. Further to this the manipulation of spin wave

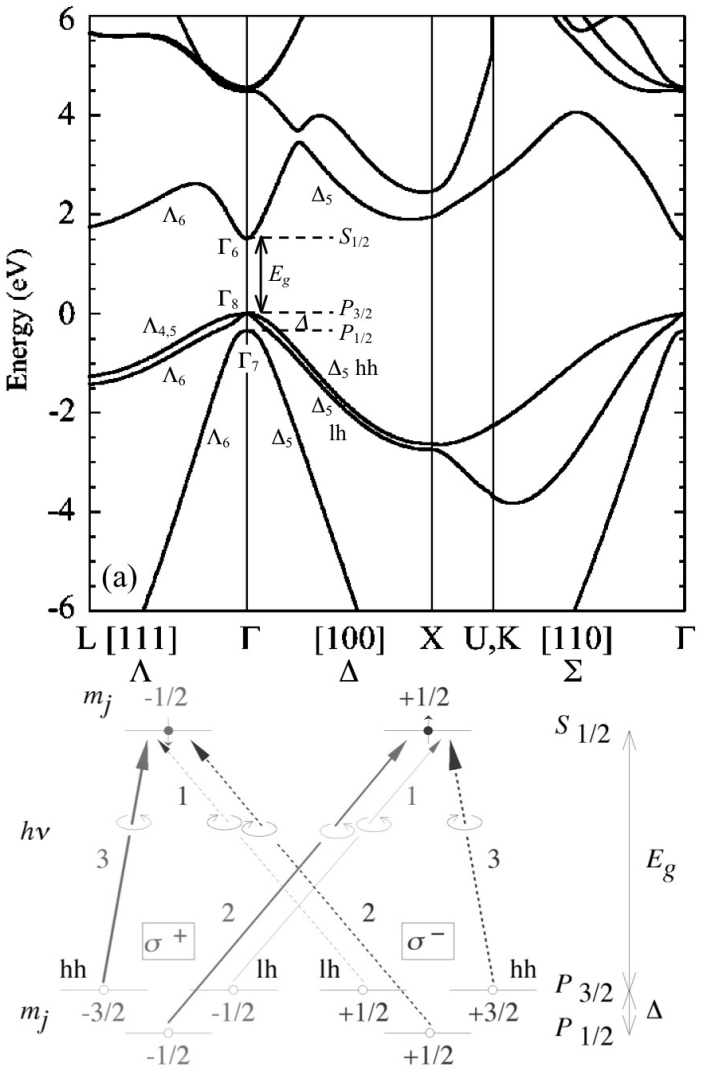

Figure 2.6: Band diagram of GaAs showing the direct band-gap transition and the allowed transitions for the right (solid lines) and left (dashed lines) circularly polarised light, taken from ref. [43].

currents has been demonstrated by Satoh *et al.* [51] in AFs.

2.2.5 Electrical injection and detection

In the two-channel model a ferromagnetic (F) conductor is pictured as two resistors in parallel. The resistance of each channel varies depending on the material and consists of a spin majority (lower resistance) and a spin minority (higher resistance) path for electrons. A current passing through two F conductors can be pictured as shown in figures 2.2(a) and 2.2(b). The two-channel model is used to explain spin-dependent behaviour in spin-valves. Spin-valves are stacks of at least two F layers that are separated by a non-magnetic conductor. The resistance of a spin-valve is dependent upon the relative

magnetisation direction of the magnetic layers and the two-channel model for a spin-valve is shown in figure 2.2. Conventionally the spin current in a spin-valve is accompanied by a charge current. To separate the charge current from the pure spin current the stack can be spread laterally across a substrate. This is known as a lateral spin-valve (LSV) and is shown in figure 2.7(a). An LSV consists of an F injector, an intermediate non-magnetic spin channel and an F detector.

If a positive potential is applied to the injector circuit, shown in figure 2.7(a), electrons will flow from the non-magnetic NM to the F wire. Due to the difference in the resistance of the spin channels a proportion of the electrical current in the F wire will be spin polarised. The magnitude of the majority spin current, I_{S}, in the F wire is given by

$$I_{\mathrm{S}} = \alpha I \tag{2.21}$$

where α is the spin polarisation of the material. The spin polarisation arises from filled and unfilled electron states in the *d*-band for majority and minority spins. To a lesser extent, hybridisation of the *s*-band electrons with the *d*-band also contributes to the spin polarisation. The spin polarisation (α) of a material is defined by its density of states,

$$\alpha = \frac{N_{\uparrow}(E_{\mathrm{F}}) - N_{\downarrow}(E_{\mathrm{F}})}{N_{\uparrow}(E_{\mathrm{F}}) + N_{\downarrow}(E_{\mathrm{F}})} \tag{2.22}$$

where $N_{\uparrow/\downarrow}(E_{\mathrm{F}})$ is the spin dependent density of states at the Fermi surface. If $N_{\uparrow/\downarrow}(E_{\mathrm{F}})$ is *d*-like the material will have a high degree of spin polarisation. If, however, $N_{\uparrow/\downarrow}(E_{\mathrm{F}})$ is *s*-like or has some *s*-*d* hybridisation the spin polarisation will be reduced. The spin polarisation for Permalloy has been reported to be (37$\pm$5)% [52].

Due to this flow of partially spin polarised current a spin imbalance is created in the NM near the interface between the F and NM. The simplest way to picture the spin channel chemical potential in the region of the interface is by splitting the current, I, into two components.

$$I = I_{\mathrm{S}} + I_{\mathrm{C}} \tag{2.23}$$

where I_{S} is the spin polarised charge current component and I_{C} is the non-polarised charge current component. The chemical potential of each spin channel must vary with x as shown in figures 2.7(b) to 2.7(d) as the current is conserved across the interface. Figure 2.7(b) shows the potential drop across the interface due to the conductivity mismatch between the F and NM sections. Figure 2.7(c) shows the potential drop due to the difference in the resistances for the individual spin channels in the region of the interface.

The accumulated spin splitting potential is considered classically where the spin

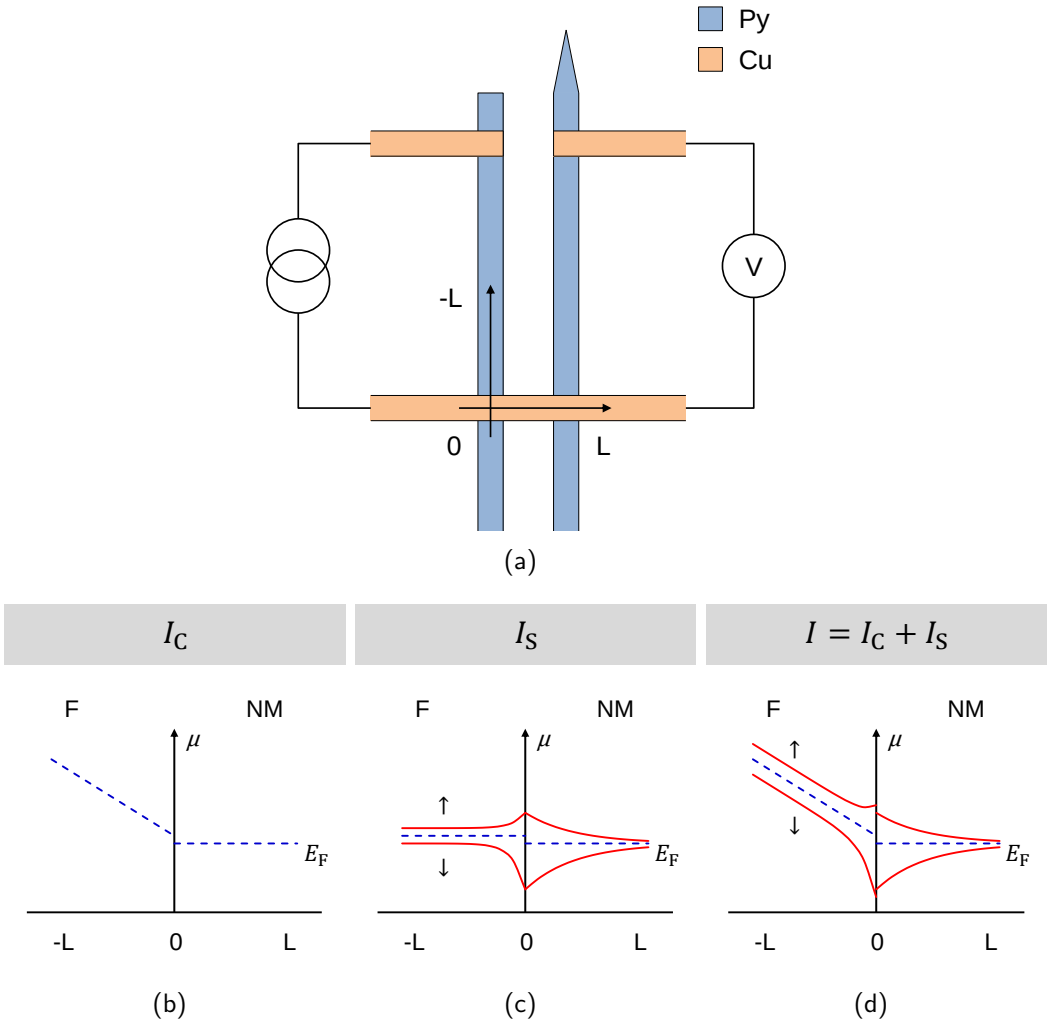

Figure 2.7: (a) A cartoon of a lateral spin-valve and (b) the spin independent, (c) spin dependent and (d) combined Fermi levels in the region of a ferromagnetic/non-magnetic interface.

imbalance diffuses away in all directions. The rate of diffusion is defined by the spin diffusion length, λ_S,

$$\Delta\mu_S = \mu_\uparrow e^{-x/\lambda_S} - \mu_\downarrow e^{-x/\lambda_S} \tag{2.24}$$

and is discussed in more depth in section 2.3. As well as a voltage drop due to conductivity mismatches between the materials for the spin channels, there is a further phenomenon known as "spin accumulation" in the region of the interface. The spin accumulation effect at a boundary was first described by Dyakonov and Perel [20]. The discontinuity of the spin flux in the spin density equation causes there to be an "accumulation" of spin at the interface. Although this was originally used to describe the case where there is an abrupt, infinite barrier/boundary this can also be applied to the cases where there is simply a conductivity mismatch which manifests as a potential barrier to the same effect. In the ideal case where the interface is transparent this effect is

negligible.

2.3 Spin diffusion

A spin imbalance may be injected from a ferromagnetic wire into a non-magnetic wire as described in section 2.2.5. A spin imbalance is observable as a potential difference due to the difference in chemical potential between the spin dependent channels. The discussion given in this section will summarise the derivation of the measured voltage made by Jedema *et al.* [48] in the pseudo-one dimensional case and consider its validity. The work by Jedema *et al.* was a continuation of the work originally performed by Johnson and Silsbee in 1985 [13]. Jedema *et al.* fabricated lateral spin-valve, LSV, structures with Copper and Aluminium as the spin-diffusion channel. From these devices they measured the spin diffusion length and fitted the data using a simple one-dimensional diffusive model.

2.3.1 The spin diffusion equaton

The introduction of a spin imbalance into a non-magnetic metal, *e.g.* Copper, nanowire where the electrons are in thermal equilibrium results in the diffusion of spin-polarised electrons. The system is modelled as a resistor network as shown in figure 2.8(a), obeying the principles of the two-channel model for spin-polarised current discussed in section 2.1.3. In figure 2.8(a), the blue(red) resistors represent the spin majority(minority) spin channels. In the ferromagnetic wires (labelled F_1 and F_2) the spin majority channel has a lower resistance. In the non-magnetic channel (labelled NM) the resistances of the spin channels are equal. The grey resistors represent spin-flip scattering, the process by which spin polarised electrons scatter from majority to minority or vice versa over the length of the diffusion channel. The grey resistors are schematic and spin-flip scattering will occur indiscriminately and independently of the position or magnitude of the spin-imbalance and so can scatter from one channel to the other at any point along the channel. But for the purposes of illustration the spin-flip scattering resistor is placed between the injection and detection points of alternative spin channels. In the non-magnetic channel the electrons flow in opposite, compensating directions due to an additional chemical potential in one spin channel and the equal reduction in chemical potential in the other as shown in figure 2.8(b). Electron diffusion follows the Einstein

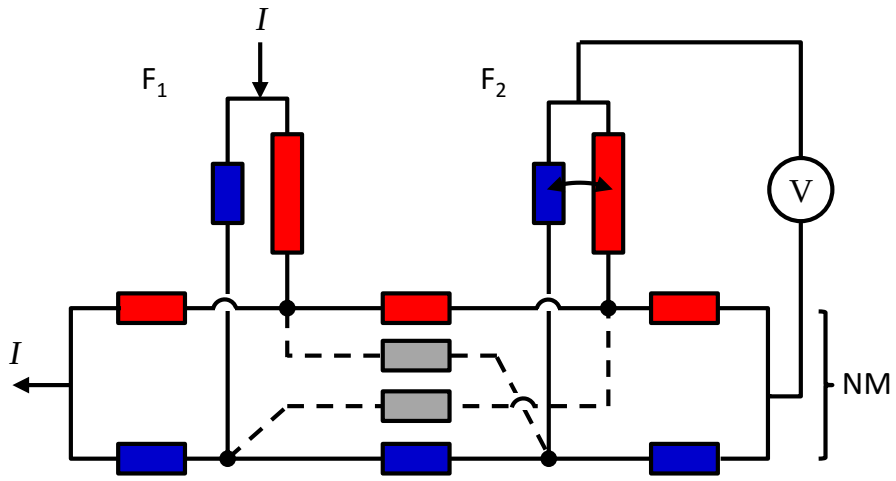

(a)

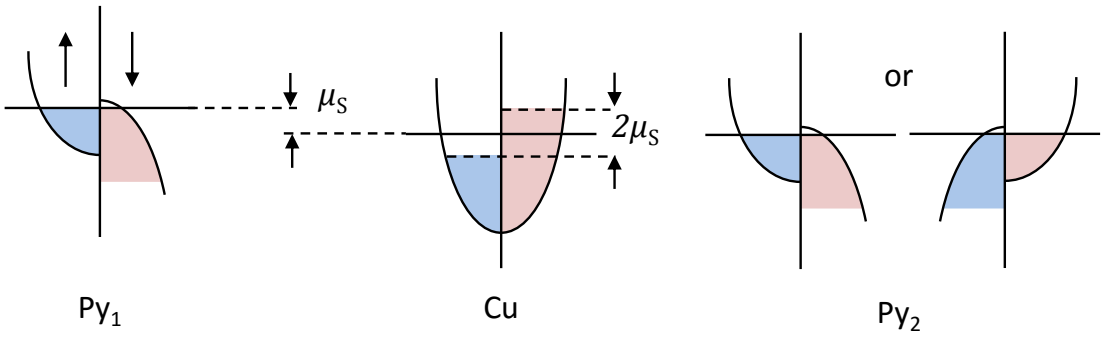

(b)

Figure 2.8: (a) A lateral spin-valve modelled as a resistor network following the two-channel model (see section 2.1.3) and (b) a band diagram representation of the spin imbalance induced by a ferromagnetic (Permalloy) injector, its transition along a non-magnetic wire and subsequent detection.

relation for the kinetic theory of electrons [53, 54],

$$D = \frac{1}{\rho {q_\mathrm{e}}^2 N_{\uparrow/\downarrow}(E_\mathrm{F})}\,, \tag{2.25}$$

where D is the electron diffusion constant, ρ is the resistivity, q_e the electronic charge and $N_{\uparrow/\downarrow}(E_\mathrm{F})$ is the density of states. The equation of motion for the electrons is given by

$$D\frac{\partial^2(\mu_\uparrow - \mu_\downarrow)}{\partial x^2} = \frac{(\mu_\uparrow - \mu_\downarrow)}{\tau_\mathrm{sf}}\,, \tag{2.26}$$

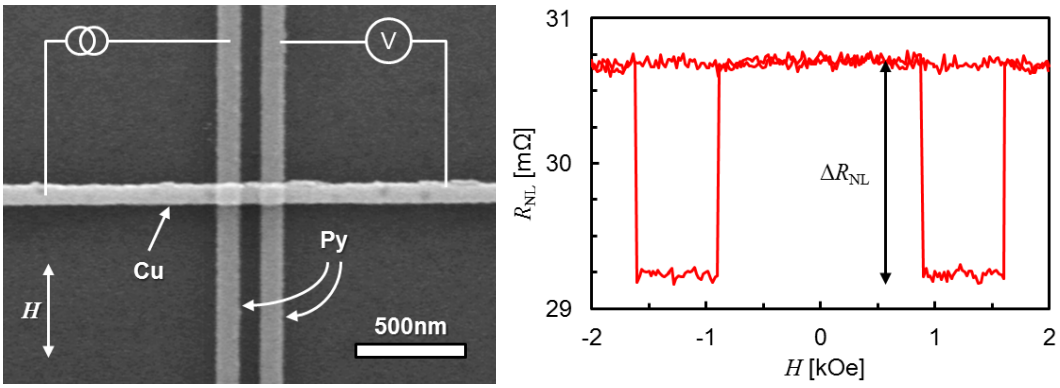

(a) (b)

Figure 2.9: (a) A typical lateral spin-valve device and (b) a characteristic non-local signal.

where D in this case is the spin-averaged diffusion constant, $\mu_{\uparrow(\downarrow)}$ is the chemical potential for the spin up (down) channel and τ_{sf} is the spin averaged relaxation time. The general solution to equation (2.26) is [55]

$$\mu_{\uparrow(\downarrow)} \propto \rho_{\uparrow(\downarrow)} \exp(-x/\lambda_{\mathrm{S}}) \,, \tag{2.27}$$

where $\mu_{\uparrow(\downarrow)}$ is the spin up (down) chemical potential, $\rho_{\uparrow(\downarrow)}$ is the spin up (down) resistivity, x is the distance and λ_{S} is the spin diffusion length which is equal to $\sqrt{D\tau_{\mathrm{sf}}}$ [54].

Equation (2.27) defines the spin dependent chemical potential a distance x away from the origin: the injection point. Attention is now turned to the detection of this voltage by a second ferromagnetic detection wire in an arrangement shown in figure 2.9(a). The voltage that is measured across the interface of the Copper channel and the Permalloy is a result of the spin imbalance in the Copper channel and the relative polarisation of the Permalloy detector relative to the injector. As an external field is swept, the injector and detector bars change from a parallel to an anti-parallel alignment, shown in figure 2.8(a) as the reversal of the spin dependent resistivities in the detector wire. The spin imbalance in the Copper channel moves from having a relatively higher chemical potential to a relatively lower chemical potential in the spin majority channel compared to the detector. The voltage measured in the parallel case, as given by Jedema *et al.* [48], is

$$V = -jq_{\mathrm{e}} \frac{\alpha_{\mathrm{F}}^2 \rho_{\mathrm{N}} \lambda_{\mathrm{S(N)}} \exp(-L_{\mathrm{F-F}}/2\lambda_{\mathrm{S(N)}})}{2(D_{\mathrm{s.d.p}}+1)[D_{\mathrm{s.d.p}} \sinh(L_{\mathrm{F-F}}/2\lambda_{\mathrm{S(N)}}) + \cosh(L_{\mathrm{F-F}}/2\lambda_{\mathrm{S(N)}})]} \,, \tag{2.28}$$

where j is the current density, q_{e} is the electronic charge, $\rho_{\mathrm{F(N)}}$ is the resistivity of the ferromagnetic (non-magnetic) wire, $L_{\mathrm{F-F}}$ is the distance between the ferromagnetic injector and detector wires and λ_{SN} is the spin diffusion length in the non-magnetic wire.

α_{F} is the spin polarisation in the ferromagnetic injector and is defined as

$$\alpha_{\mathrm{F}} = \frac{\rho_{\downarrow} - \rho_{\uparrow}}{\rho_{\downarrow} + \rho_{\uparrow}}\,, \tag{2.29}$$

where $\rho_{\uparrow(\downarrow)}$ is the resistivity of the spin up (down) channel. $D_{\mathrm{s.d.p}}$ is a spin transport prefactor defined as

$$D_{\mathrm{s.d.p}} = \frac{\rho_{\mathrm{N}}\lambda_{\mathrm{S(N)}}}{\rho_{\mathrm{F}}\lambda_{\mathrm{S(F)}}}(1-\alpha^2)\,, \tag{2.30}$$

where $\rho_{\uparrow(\downarrow)}$ is the resistivity of the spin up (down) channel. The ratio between the spin dependent resistivities, α, is also known as the spin asymmetry component, which for Permalloy is 0.7 [56].

Now, equation (2.28) is the case for transparent interfaces, where it is assumed that there is no spin resistance asymmetry at the interface. This, in actuality, is unlikely to be the case. As the interface in such devices is highly unlikely to be atomically flat there will be canting of the magnetic moments at the interface of the atomic sites in the Permalloy. This non-uniform magnetisation topology at the interface leads to two factors that are not taken into account in equation (2.28). Firstly, that there is a spin-resistance asymmetry at the interface and secondly, that the spin-resistance asymmetry is uniform across the interface.

In the geometry that is presented in this work and through the experimental work undertaken it is not possible to distinguish the effects of a non-transparent interface from the bulk spin-resistance asymmetry. The interface is approximately one-dimensional, in that there is some finite width to the spin dependent electronic band structure across the interface, with a spin scattering asymmetry. Therefore, the spin polarisation, α, is replaced in equation (2.28) by P_{i}, the spin polarisation injection efficiency in the Copper at the injection interface, to give:

$$V = -jq_{\mathrm{e}}\frac{P_{\mathrm{i}}^2\rho_{\mathrm{N}}\lambda_{\mathrm{S(N)}}\exp(-L_{\mathrm{F-F}}/2\lambda_{\mathrm{S(N)}})}{2(D_{\mathrm{s.d.p}}+1)[D_{\mathrm{s.d.p}}\sinh(L_{\mathrm{F-F}}/2\lambda_{\mathrm{S(N)}})+\cosh(L_{\mathrm{F-F}}/2\lambda_{\mathrm{S(N)}})]}\,. \tag{2.31}$$

With regards to accounting for the uniformity of the spin-resistance asymmetry at the interface, this is very hard to do. The uniformity of the spin-scattering asymmetry is linked to the uniformity of the current density at the interface. It should not be assumed that the current density at the interface is uniform, in fact this is likely to be higher at the shortest current path, as it should not be assumed that the spin scattering is uniform. However, the focus of this work is on spin transport in the spin channel between the ferromagnetic contacts and so although the polarisation of the spin current at the Permalloy/Copper interface is considered, it is the spin diffusion length that is

the figure of most interest in this study.

2.3.2 Observation of spin diffusion

When the two ferromagnetic wires switch to an anti-parallel state the chemical potential between the spin imbalance and the detector wire inverts as shown in figure 2.8(a). As the external field is swept the typical non-local signal is shown in figure 2.9(b). The voltage in the anti-parallel case is equal, but opposite in magnitude, to equation (2.33). Therefore the detected change in non-local resistance is

$$\Delta R_{\mathrm{NL}} = \frac{(P_{\mathrm{i}}^2 \rho_{\mathrm{N}} \lambda_{\mathrm{S(N)}}/a_{\mathrm{N}}) \exp(-L_{\mathrm{F-F}}/2\lambda_{\mathrm{S(N)}})}{(D_{\mathrm{s.d.p}}+1)[D_{\mathrm{s.d.p}} \sinh(L_{\mathrm{F-F}}/2\lambda_{\mathrm{S(N)}}) + \cosh(L_{\mathrm{F-F}}/2\lambda_{\mathrm{S(N)}})]}\,, \qquad (2.32)$$

where P_{i} is the spin polarisation injection efficiency in the Copper channel at the interface, $\rho_{\uparrow(\downarrow)}$ is the spin dependent resistivity, $D_{\mathrm{s.d.p}}$ is the spin diffusion prefactor, defined in equation (2.30), a_{N} is the cross-sectional area of the non-magnetic wire, $L_{\mathrm{F-F}}$ is the distance between the ferromagnetic injector and detector wires and λ_{SN} is the spin diffusion length in the non-magnetic channel.

The fundamental assumption of the derivation was that the transport could be considered diffusive which only holds when the mean free path is smaller than the dimensions of the system. For Copper the mean free path in thin films was found to be 55 nm at room temperature [57]. Jedema *et al.* also assume that the resistivity of the wires is uniform along their length. Roughness and other asperities at the surface preclude this. The model assumes that the interfaces are transparent, that the spin-flip resistance is continuous across the interface and that the current density is uniform across the interface. These assumptions are unlikely to be true. However, a complete model where the effects are accounted for would be impossible given current knowledge. Although techniques such as suspended mask fabrication allow for the successive deposition of wires without breaking ultra-high vacuum for clean interfaces [58, 59], effects due to non-uniform current densities, pin-hole transmission and sample defects are difficult to take into account.

There are three physical certainties that are not accounted for in the models [48, 58]: the first is that the diffusion of the spin-current is three dimensional, secondly that there is a finite interfacial spin-flip resistance and thirdly that the spin injection current is non-uniform at the interface. An attempt to model spin diffusion in three dimensions was made by Hamrle *et al.* [56], who found significant turbulent flow of the electrons in the independent spin channels. However, on taking the difference between the independent spin channels to calculate the pure spin current they found that there

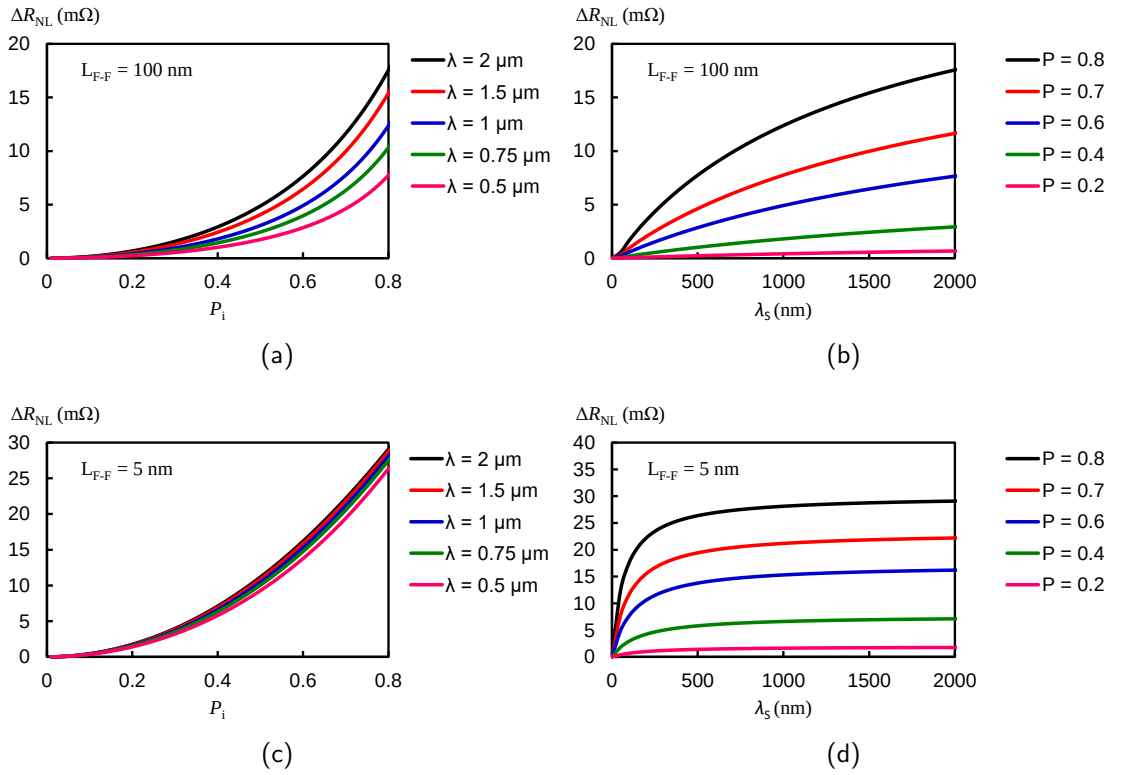

Figure 2.10: The dependence of R_{NL} as a function of (a) spin polarisation injection efficiency, P_{i} and (b) spin diffusion length, λ_{S} at $L_{\mathrm{F\text{-}F}}$ =100 nm and (c) spin polarisation injection efficiency, P_{i} and (d) spin diffusion length, λ_{S} at $L_{\mathrm{F\text{-}F}}$ =5 nm.

was little improvement to the voltage values calculated in comparison to experiment [56]. Therefore, it is sufficient to consider the spin diffusion equation in the form in equation (2.32). Taking equation (2.32) and applying hyperbolic trigonometric identities to the equation yields the equivalent equation

$$\Delta R_{\mathrm{NL}} = \frac{4P_{\mathrm{i}}^2 R_{\mathrm{F}}^2}{(1-P_{\mathrm{i}}^2)R_{\mathrm{N}}} \frac{\exp(-L_{\mathrm{F-F}}/\lambda_{\mathrm{S}})}{[1+\frac{2R_{\mathrm{F}}}{(1-P_{\mathrm{i}}^2)R_{\mathrm{N}}}]^2 - \exp(-2L_{\mathrm{F-F}}/\lambda_{\mathrm{S}})}, \tag{2.33}$$

where P_{i} is the spin polarisation injection efficiency in the Copper channel at the interface, $L_{\mathrm{F-F}}$ is the distance between the ferromagnetic injector and detector wires and λ_{S} is the spin diffusion length in the non-magnetic channel. $R_{\mathrm{F(N)}}$ is the spin resistance of the ferromagnetic (non-magnetic) wire. This is the resistance between spin channels in the respective materials, *e.g.* the effective resistance to spin flipping from spin majority to minority in Copper, and is defined mathematically as

$$R_{(\mathrm{F/N})} = \frac{\rho_{(\mathrm{F/N})}\lambda_{\mathrm{S(F/N)}}}{a_{(\mathrm{F/N})}} \tag{2.34}$$

where $\rho_{(\mathrm{F/N})}$ is the resistivity, $\lambda_{\mathrm{S(F/N)}}$ is the spin diffusion length and $a_{(\mathrm{F/N})}$ is the cross-sectional area of the ferromagnetic/non-magnetic wires.

To illustrate the effect of key terms within equation (2.33) and its form, plots of the change in non-local resistance as a function of spin injection efficiency, P_{i}, and spin-diffusion length are shown in figure 2.10. As can be seen, equation (2.33) consists of a pre-factor that is dominated by P_{i} and determines the magnitude of the spin imbalance that is injected at the interface, as would be expected from the spin injection efficiency term. The rest of the formula is exponential in form, with a decay with distance from the injection point that is dependent on λ_{S}.

There are diminishing returns for increases in λ_{S} shown by the change in non-local resistance, ΔR_{NL}, levelling out in figure 2.10(d). Yet the opposite is true for P_{i} in figure 2.10(c). Furthermore, there is practically no increase in ΔR_{NL} when $\lambda_{\mathrm{S}} \gg L_{\mathrm{F\text{-}F}}$ as is shown in figures 2.10(c) and 2.10(d) which shows that in the low length limit that the polarisation efficiency is the dominating factor. However, this limit has yet to be achieved in non-local spin valves where the geometry tends to be lateral in nature with a separation between electrodes of the order of hundreds of nanometres. In this higher length scale limit λ_{S} plays a more important role in the magnitude of R_{NL} at the detection electrode.

2.4 Spin amplification by spin channel filtering

It was found computationally and experimentally by Abdullah *et al.* [60, 61] that the introduction of certain geometries into a non-magnetic nanowire altered the scattering cross section for electrons travelling in opposite directions. In the compensated, two-channel model of electron diffusion in a lateral spin-valve this results in "spin filtering" of one of the spin channels. The approach taken by Abdullah *et al.* was to model the electron diffusion as summarised here along with a phenomenological discussion of the experimental consequences.

2.4.1 Geometric effect on a spin-polarised current

As discussed in section 2.3.1 spin diffusion is governed by the spin diffusion equation. The time dependence is included to give the complete expression,

$$\frac{\partial n_{\mathrm{e}}(\mathbf{r},t)}{\partial t} = D\nabla^2 n_{\mathrm{e}}(\mathbf{r},t) - \frac{n_{\mathrm{e}}(\mathbf{r},t)}{\tau_{\mathrm{S}}}\,, \tag{2.35}$$

where n_{e} is the electron density, $\mathbf{r}$ is the position in three dimensions, t is time and τ_{S} is the diffusion length. Time dependence is included as it was found by Zhu *et al.* [62] that

in addition obeying Fick's law in the diffusive manner outlined by Valet and Fert [63] spin imbalance also possesses wave-like characteristics that in a high frequency regime will affect the spin dynamics. When time dependence is incorporated into the diffusion equation there are second order time-derivatives that are not present in the steady state. These second order derivatives show that the spins take a finite time to adjust to the local spin density gradient. This leads to the addition of a wave-like characteristic to the diffusive transport characteristics [62]. This would become of importance if a nanosecond pulsed injection/detection system were employed.

The model assumed a 100% spin-polarised current at the origin of the spin channel. This would be more appropriate for a half-metallic metal where there is a band gap at the Fermi level in one spin direction. Such work has been done, and it has been shown that there is an improved injector polarisation [64]. However, the spin polarisation of the ferromagnetic injector was limited to 74% [64]. Even if a ferromagnetic injector of an exceptionally high spin polarisation were used, a spin injection efficiency of 100% would still be difficult to achieve. Nonetheless, as a model of the spin transport behaviour it suffices. The system was modelled as two-dimensional. An increase in electron density was introduced at the origin at t =0 as a delta function. The boundary conditions used for solving equation (2.35) were

$$\mu_{\mathrm{S}}(x, y, t) = \delta_{\mathbf{r}}\,, \tag{2.36}$$

$$\frac{\partial \mu(\mathbf{r}, t)}{\partial \mathbf{e}} = 0\,, \tag{2.37}$$

$$\text{and } \mu(\mathbf{r} = \pm\infty, t) = 0\,, \tag{2.38}$$

where μ is the chemical potential, δ is the Kronecker delta (equal to unity at $\mathbf{r} = 0$) and $\mathbf{e}$ is the unit vector normal to the boundary surface of the channel. These boundary conditions can be applied without loss of generality to any spin channels injected with a pulsed spin imbalance. The first boundary condition describes the injection of a delta-like pulse. The second states that the spin imbalance diffuses homogeneously in all directions. The third term states that the spin imbalance reduces to zero at an infinite distance from the origin. To avoid interference by electron reflection at the detector interface, the diffusion length at the interface was set to five times that in the spin channel.

Using finite element modelling software various geometries were applied to the mesh of the Copper spin channel as shown in figure 2.11. The spin imbalance was injected at $\mathbf{r} = 0$ and the chemical potential was calculated at the detection terminal. A full discussion of the validation of the model and the choice of mesh distribution is given in ref. [65].

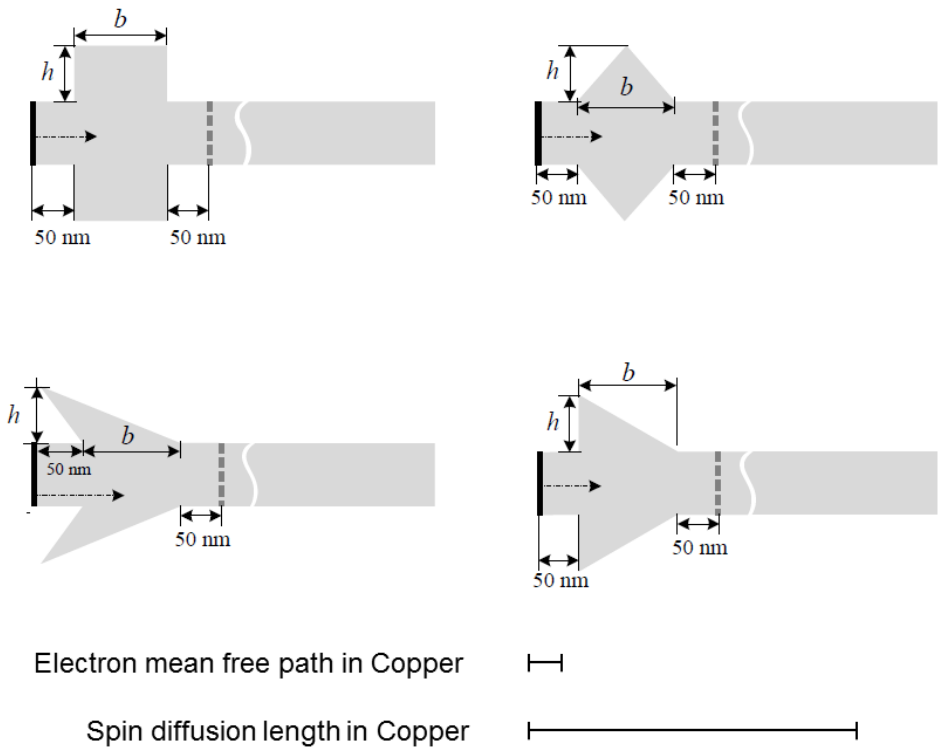

Figure 2.11: Geometries introduced in to the spin channel, reproduced from ref. [65], including the electron mean free path and spin diffusion lengths in Copper for comparison (values are approximate).

2.4.2 Implementation of the two-channel model

The charge current in the spin channel is given by

$$j_{\mathrm{C}} = j_{\uparrow} + j_{\downarrow}\,, \tag{2.39}$$

where $j_{\mathrm{C}/\uparrow/\downarrow}$ represents the charge current density, the spin up current density or the spin down current density. The charge current must be set to zero. For the final calculation a compensating pulsed current was introduced at the opposite end of the channel. So for a spin imbalance injected at the left of a configuration shown in figure 2.11 the spin majority pulse was introduced at the left of the channel and the spin minority at the right. For a spin imbalance injected at the right of the geometry the spin majority pulse was introduced at the right and the spin minority at the left. All of the calculations of diffusion were made independently.

In a diffusive regime the spin current at any given point is proportional to the gradient of the electron density [14]. As a spin-polarised packet of electrons travels along a wire a sudden increase in the wire width, as in figure 2.11, decreases the electron density

and thus the effective resistance increases. For a spin-polarised packet of electrons travelling in the opposite direction the same is the case. If the rate of change of wire width is different, however, this will have a direct effect upon the diffusion current. Therefore, only an asymmetrical geometry filters one of the spin channels if they are travelling in opposite directions, as is the case in a charge-current compensated spin-channel. In the calculation the difference in the voltages after passing through the central shape was calculated. This is not quite the same as the voltage observed as a result of the spin imbalance. The voltage due to the spin imbalance is proportional to the difference between the electron densities where the potentials are of *opposite* sign.

$$\Delta\mu_{\mathrm{S}} \propto j_{\uparrow} - j_{\downarrow}\,,\,. \tag{2.40}$$

The geometries in figure 2.11 were investigated and optimised. Repeating patterns, *i.e.* a sequence of multiple geometries in the spin channel, were investigated but the spin signal decreased by up to 40% as a result. Of the geometries studied it was found that there was a maximum amplification for a triangular geometry as shown in the bottom right of figure 2.11. Turbulent flow at the corners of the arrow was observed in the finite element model, which is likely to be associated with the amplification effect. It is also worth mentioning that the amplification of the voltage at the detector is compensated by an increase in the current path as a result of the geometry. It is therefore very important to match the amplification geometry with a channel length tuned to the spin diffusion length ($L_{\mathrm{F-F}} < \lambda_{\mathrm{S}}$).

In the steady state when $t \to 0$, equation (2.35) can be rewritten as

$$D\Delta\mu_{\mathrm{S}}(x,y) = \frac{\mu_{\mathrm{S}}(x,y)}{\tau_{\mathrm{S}}}\,, \tag{2.41}$$

where the boundary conditions, equations (2.37) and (2.38), still hold and are reproduced below with the new boundary condition for the injected current.

$$\mu_{\mathrm{S}}(x,y,t) = \mu_{\mathrm{S0}}\,, \tag{2.42}$$

$$\frac{\partial\mu(\mathbf{r},t)}{\partial\mathbf{e}} = 0\,, \tag{2.37}$$

$$\text{and } \mu(\mathbf{r} = \pm\infty, t) = 0\,. \tag{2.38}$$

where μ_{S0} is the chemical potential of the electron packet introduced at the origin. Similar turbulent electron flow was observed in the triangular geometry as for the time dependent case.

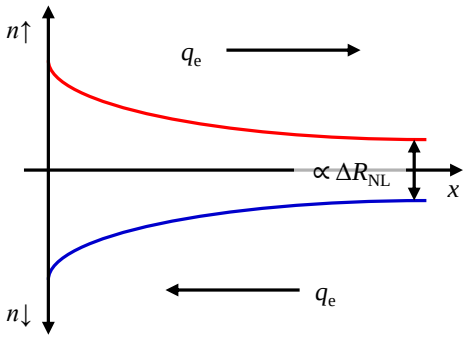

Figure 2.12: Spin up and spin down electron density in a lateral spin-valve wire.

This model should therefore give a qualitative indication of the geometrical effect of the channel on a spin current. It should be emphasised that the model is *not* quantitative. In reality a positive spin-majority electron density is introduced at the left of the channel along with a negative spin-minority electron density which drive the compensating charge currents as shown in figure 2.12. In the model, a positive spin-minority electron density was introduced at the right of the channel. In experiment the measured voltage is the difference between the chemical potentials as shown in figure 2.12 and equation (2.40).

In the corresponding experimental work [60] samples were fabricated by electron beam lithography using Permalloy as the injector and detector pair for which the spin polarisation, α, is 0.7 [56]. Vacuum was also broken between deposition stages so there is likely to have been a spin-flip resistance at the interface due to surface oxidation.

The samples were measured in the manner outlined in figure 2.9(a) and section 3.4.

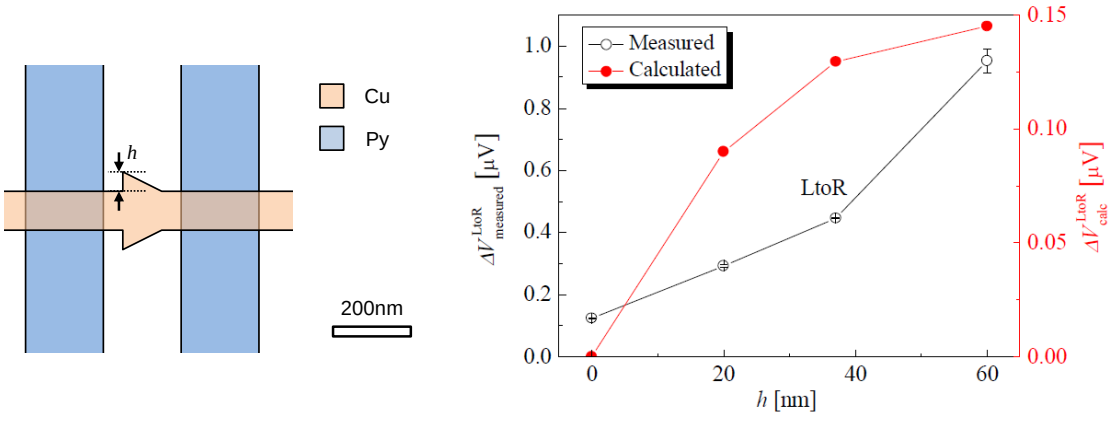

(a) (b)

Figure 2.13: (a) Schematic of the arrow device and (b) a plot of the measured non-local voltage in one direction (black axis and open circles), compared to the calculated value (red axis and closed red circles), taken from ref. [60].

There is significant discrepancy between the predicted and measured values (almost an order of magnitude). However, the trend of an increase in spin current amplification by spin filtering for a non-symmetrical triangular shape in a spin channel is confirmed, with the measured spin signal increasing by a factor of 7 as can be seen in figure 2.13(b). To confirm that the effect is geometrical in origin, measurements need to be taken of samples that are symmetric.

In symmetric geometries it is expected that there will be no amplification by spin filtering. It must be proven that there is direction dependent resistivity for the compensating spin-channels. Electrical measurements comparing the difference between signals obtained when injecting from the left and measuring at the right and vice versa are discussed in section 5.2.

2.5 Spin interference

This section is geared towards the magnetic gate operation of a lateral spin-valve structure. The discussion is based on the Hanle effect which may be used to measure the spin diffusion length in semiconductors, Graphene or metal systems [13, 66, 67]. The dynamics of electron spins in the presence of a magnetic field has been discussed in section 2.1.4. A packet of spin polarisation, a spin-imbalance, behaves as a single body by the Russell-Saunders interaction [28]. It is the behaviour of this single body of electron spins in the presence of a magnetic field that is discussed in this section.

2.5.1 The Hanle effect

The Hanle effect is the application of a magnetic field to a spin imbalance that acts to push the imbalance back into equilibrium with its surroundings. A spin imbalance in a semiconductor or Graphene system behaves in a very similar way to that in a metal system. The electron and hole pairs can be treated in the same way as the compensating charge current channels in a metal spin-valve, albeit with different carrier mobilities and inter-channel relaxation mechanisms. Therefore, without loss of any generality, the discussion that follows can be applied to a spin imbalance in any material.

In a Hanle device, the magnetic field, $\mathbf{B}$, applied to induce the Hanle effect, the electron spin vector, $\mathbf{S}$, and the direction of electron diffusion will conventionally be orthogonal to each other as shown in figure 2.14. With the application of a magnetic field an electron has an additional precession. This precession has the well-known cy-

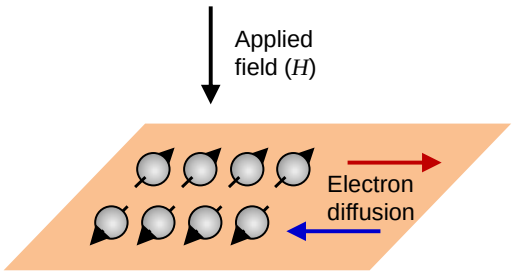

Figure 2.14: Geometry of the applied field, electron spin and electron diffusion for the Hanle effect.

clotron/Larmor frequency given by

$$\omega_{\mathrm{C}} = \frac{\mu_{\mathrm{B}} g B}{\hbar}\,, \tag{2.43}$$

where μ_{B} is the Bohr magneton, g is the Landé g-factor, B is the magnetic field strength and $\hbar$ is the reduced Planck constant. The introduction of this additional precessional term to the Landau-Lischfitz-Gilbert (LLG) type of dynamics discussed in section 2.1.4 causes the electrons to dephase at an increased rate [54, 68].

As a result of this Hanle dephasing an additional term must be added to equation (2.26), the spin diffusion equation as reproduced below, to form

$$\begin{aligned} D\frac{\partial^2(\mu_\uparrow - \mu_\downarrow)}{\partial x^2} &= \frac{(\mu_\uparrow - \mu_\downarrow)}{\tau_{\mathrm{sf}}} \\ D\frac{\partial^2(\mu_\uparrow - \mu_\downarrow)}{\partial x^2} + \omega_{\mathrm{C}} \times (\mu_\uparrow - \mu_\downarrow) &= \frac{(\mu_\uparrow - \mu_\downarrow)}{\tau_{\mathrm{sf}}}\,, \end{aligned} \tag{2.44}$$

where D is the spin-averaged diffusion constant, $\mu_{\uparrow(\downarrow)}$ is the chemical potential for the spin up (down) channel, τ_{sf} is the spin averaged relaxation time and ω_{C} is the cyclotron frequency. Following on from this, the Hanle effect may be considered as perturbation of the spin diffusion length. The spin diffusion length holds a Lorentzian relationship with the applied magnetic field, given by the real component of augmented spin diffusion length,

$$\lambda_{\mathrm{w}} = \frac{\lambda_{\mathrm{S}}}{\sqrt{1 + \mathrm{i}\omega_{\mathrm{C}}\tau_{\mathrm{sf}}}}\,, \tag{2.45}$$

which on multiplying the top and bottom by the complex conjugate, becomes

$$\mathrm{Re}\lambda_{\mathrm{w}} = \frac{\lambda_{\mathrm{S}}}{\sqrt{1 + (\omega_{\mathrm{C}}\tau_{\mathrm{sf}})^2}}\,, \tag{2.46}$$

where λ_{S} is the spin diffusion length in the absence of an applied field, ω_{C} is the cyclotron frequency defined above in equation (2.43) and τ_{sf} is the spin averaged relaxation time,

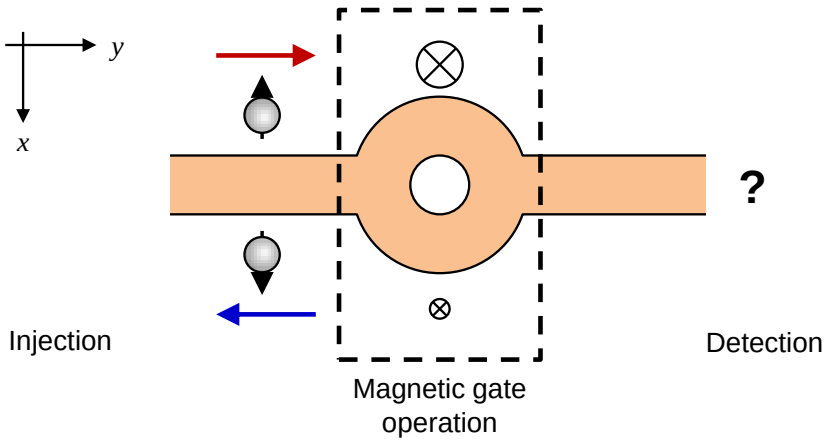

Figure 2.15: Diagram of the proposed magnetic three-terminal non-local device channel.

equivalent to $\frac{1}{\tau} + \frac{1}{\tau_S}$. Equation (2.45) is substituted into equation (2.33) to give the non-local resistance in the presence of a field in the z-direction.

$$R_{NL}(B_\perp) = \pm\frac{\alpha_1\alpha_2 D\rho_N}{a_N}\int_0^\infty \Phi(t)\cos(\omega_L t)\exp\left(-\frac{Dt}{{\lambda_S}^2}\right)\mathrm{d}t \tag{2.47}$$

where

$$\Phi(t) = \frac{1}{\sqrt{4\pi Dt}}\exp\left(-\frac{L_{F-F}^2}{4Dt}\right). \tag{2.48}$$

Finding the analytical solution to equation (2.47) is difficult, yet was found by Sasaki *et al.* [69] to be

$$\begin{aligned} R_{NL}(B_\perp) =& \frac{\alpha^2\rho_N\sqrt{D\tau}}{2a_N}\exp\left(-\frac{L_{F-F}}{\sqrt{D\tau}}\right)(1+{\omega_L}^2\tau^2)^{-1/4} \\ &\times\exp\left\{-\frac{L_{F-F}}{\sqrt{D\tau}}\left[\sqrt{\frac{1}{2}(\sqrt{1+{\omega_L}^2\tau^2}+1)}-1\right]\right\} \\ &\times\cos\left[\frac{\arctan(\omega_L\tau)}{2}+\frac{L_{F-F}}{\sqrt{D\tau}}\sqrt{\frac{1}{2}(\sqrt{1+{\omega_L}^2\tau^2}-1)}\right] \end{aligned} \tag{2.49}$$

where $\alpha_{01/2}$ is the spin polarisation of the injector/detector, D is the diffusion constant, ρ_N is the resistivity, a_N is the cross-sectional area of the Copper wire, ω_L is the Larmor frequency, t is time, λ_S is the spin diffusion length in the Copper wire, L_{F-F} is the distance between the ferromagnetic injector and detector, and τ is the spin averaged relaxation time.

2.5.2 Magnetic field controlled logic

Lateral spin-valve devices with conventional metal spin-diffusion channels are in essence two-terminal devices. The operation of these devices requires the application of an external magnetic field to align the magnetisation of the injecting ferromagnetic wire, for example using the demagnetising field that is sensed to detect bits of data on a hard disk could be used to reverse the magnetisation of the ferromagnetic injector in analogy with the free layer in the read head in a hard disk drive [70–73]. The device geometry proposed here would allow for the three-terminal operation of a lateral spin-valve device by an additional local magnetic field. The local magnetic field could be used to manipulate spins in different channels that, on recombination, could interfere in some way. The spin channels would have differing spin diffusion lengths and so upon recombination the spin signals "interfere". The concept of a spin interference device is not new. In 1990 Datta and Das [15] proposed that spin interference of this nature could occur with materials with a differing spin-orbit coupling strength or interaction. However, it is crucial to achieve spin interference efficiently within a short distance, a few microns in the device proposed by Datta and Das [15].

In the specific geometry, discussed in more detail in section 4.4, the non-magnetic spin channel diverges into two channels and then recombines between the ferromagnetic injection and detection wires as shown in figure 2.15. Rather than altering the spin-orbit interaction in the medium, the proposed device has a magnetic field gradient across the rings in the x direction in figure 2.15. Due to this gradient, spin imbalances of the same magnitude will be affected differently depending on which half of the ring they diffuse through. The imbalances are affected by the field that is perpendicular to their motion and spin as described above in section 2.5.1.

2.6 Interaction with magnetised bodies

Spin torque is the term applied to the reversing force that acts on a magnetised body due to a spin current. This effect is the transfer of angular momentum mediated by the flow of electrons. As such the spin torque applied to a magnetised body is proportional to the spin-polarised current [74, 75].

This effect has largely been investigated with a spin current perpendicular to a multi-layer stack in the presence of a net charge current as well as a spin transfer torque. In this section deeper discussion than that given in section 2.1.5 of the origins of spin-transfer torque and the application of the effect to lateral spin-valve structures is presented.

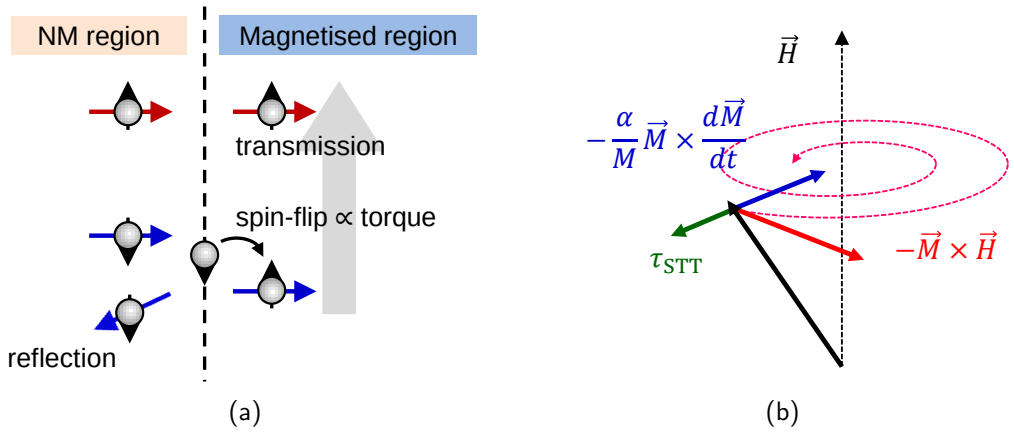

Figure 2.16: (a) Origin of the spin-transfer torque effect and (b) the governing forces of LLG dynamics with the additional sin-transfer torque term.

2.6.1 Slonczewski spin transfer torque

After the simultaneous discovery of giant magneto-resistance by Fert and Grünberg [8,9] followed the work by Slonczewski [75], proposing that a spin-polarised current could be used to affect the magnetisation of a magnetised body. There are two components to a current considered here: a purely spin-up and a purely spin-down component, that in passing through a non-magnetic medium into a magnetised region undergo one of three processes. If, for the sake of argument, the orientation of the magnetisation of the second layer is along the same axis as the electron spin as shown in figure 2.16(a), the electrons will either be transmitted, reflected or undergo a spin-flipping process. Electrons that are polarised parallel to the magnetisation will transmit across the interface. Some of the electrons that are polarised anti-parallel to the magnetised surface will be reflected. A portion of the anti-parallel electrons will undergo a spin-flipping process. It is these electrons that are responsible for the application of a switching torque to the magnetised surface [76]. These three processes can be considered as three separate current channels via analogy to the two-channel model as discussed in section 2.1.3. Due to the spin-flipping there is a voltage drop across the interface. The voltage drop due to the spin-flipping correlates to the critical switching voltage of the magnetised layer and is dissipated either as heat or a torque [76]. To approach the critical switching voltage the current density of the spin-flipping should be increased. This may be achieved by increasing driving the current with a field, by increasing the current density, or by increasing the spin-imbalance in the non-magnetic layer.

The torque due to a portion of the spin-flipped electrons can be added to the LLG equation to represent the dynamics of the spin angular-momentum. The torque term is simply added as a vector that affects the precession of the spin moment and the LLG

equation as shown in figure 2.16(b) and

$$\frac{dM}{dt} = \gamma \mathbf{M} \times \mathbf{H} + \frac{\alpha_0}{M} \mathbf{M} \times \frac{d\mathbf{M}}{dt} \tag{2.16}$$

becomes

$$\frac{dM}{dt} = \gamma \mathbf{M} \times \mathbf{H} + \frac{\alpha_0}{M} \mathbf{M} \times \frac{d\mathbf{M}}{dt} + \tau_{\mathrm{STT}}\,, \tag{2.50}$$

where M is the magnetisation and H is the field strength, γ is gyromagnetic ratio, α_0 is a dimensionless damping constant and τ_{STT} is the additional Slonczewski spin-transfer torque term.

2.6.2 Spin torque oscillators

Spin-transfer nano-oscillators (STNOs) can be used as tuneable microwave radiation emitters and detectors. An informative review into the fundamentals of STNOs is given in ref. [77]. STNOs employ a magnetic layer where the magnetisation is driven into oscillation by a spin polarised current (emitter) or incoming electromagnetic radiation (detector) [77]. In an STNO the magnetisation of a free magnetic layer precesses around the magnetisation direction of a pinning magnetic layer. The two layers are separated by a thin (generally $<$1 nm) layer of metal or insulator, in analogy to giant (GMR) and tunnel magnetoresistive (TMR) stacks. The precession of the free magnetic layer is either driven by the application of a driving spin transfer torque by the application of a current across the stack or detected by the change in voltage induced through the precession by the well-known GMR or TMR effects. STNOs have been extensively investigated in the local regime, where a spin-torque is applied through the application of a spin-polarised electronic drift current. However, these devices are restricted to a high-frequency, typically 1-10 MHz [78], operating bandwidth. In order to achieve oscillation at lower frequencies, from essentially DC up to the MHz and even GHz range, a lateral non-local spin transfer nano-oscillator could be used.

It was shown by Kimura *et al.* [79] that the magnetisation of a ferromagnetic nanoparticle could be reversed by the application of a spin transfer torque. This was carried out using the geometry shown in figure 2.17. A spin imbalance was injected into the Copper channel, carried in the direction of the Permalloy ellipse by a pulsed drift current of 13.3 mA. The drift current was drawn off at a cross geometry as shown in figure 2.17, to allow the subsequent diffusion of the spin imbalance in all directions. The spin imbalance was then detected using the Permalloy ellipse which was coupled electrically to the gold wires as a detector. Gold was used as a material due to its short spin diffusion length of (86$\pm$10) nm [80]. The short diffusion length gives rise

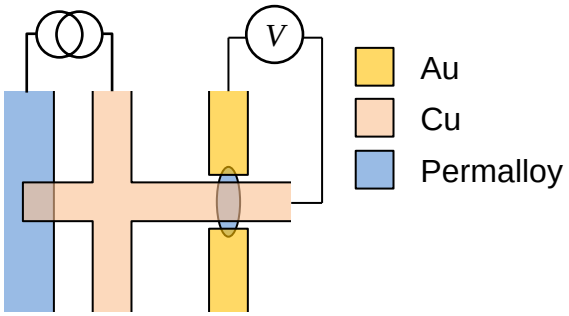

Figure 2.17: Diagram of the geometry used by Kimura *et al.* [79] to detect the switching of a ferromagnetic element by a non-locally induced spin-transfer torque.

to a relatively lower spin resistance which acts as a sink – enhancing the spin current absorption into the Permalloy ellipse [49].

In a similar experiment, Buhl *et al.* also demonstrated the switching of a ferromagnetic ellipse by a spin-transfer torque [81]. However, the transit of the spin-polarised current in the region of the ellipse was *not* induced in a non-local manner. Rather than incorporating the ferromagnetic ellipse into the detector circuitry of a lateral spin-valve, they patterned an ellipse to sit on top of a Copper nanowire in between a ferromagnetic injector and detector pair. In this case, however, the detector was used as a second injector. The advantage of this geometry is that in a non-local experimental set-up, lateral spin-valve behaviour may be investigated to confirm the presence of a spin imbalance in the Copper channel. Cobalt-Iron was the ferromagnetic material of choice due to its high moment, with a Ruthenium capping layer to prevent oxidisation. The Copper layer was therefore laid beneath the injector pair. The magnetic structure of the device was configured so that the ferromagnetic injector pair were magnetised in oppose directions, with the magnetisation of the ellipse aligned parallel to the ferromagnetic wires. A global supporting field, *i.e.* a uniform field applied to the entire sample, was applied parallel to the wires to support a bi-stable injector configuration and magnetise the ellipse in the plane of the substrate. The magnetisation of the ellipse was switched by the application of a pulsed current through the Copper channel. It was shown by scanning transmission X-ray microscopy that the magnetisation of the ellipse switched due to the spin-polarised current in transit under the ferromagnetic ellipse.

The observation of a non-locally induced STNO has been observed [82] but this was on a relatively large ($>$1 μm) scale. Here, Demidov *et al.* applied a DC current into the central region of a Permalloy disc. Owing to the large resistance of the disc the current was localised to the central region, between two lithographically defined point contacts.

The precession of the magnetisation was probed some distance ($>$1 μm) away from the injection current. Therefore the spin-torque driving any oscillations was non-local. This provides proof that, in concept, the precession of a magnetic body can be driven by a non-local spin current. However, the observation of such a phenomena in an LSV-like geometry is yet to be realised.

In summary, there are a large variety of ways to introduce spin polarisation into a system. Although the field of spintronics is developing, with new methods of generating a spin current still being discovered, the fundamentals of the physics should not be unfamiliar to those who are familiar with magnetism and electronics. And so, methods of generating a spin current generally have an analogue with an already well established electron charge or magnetic phenomena. This chapter has summarised the basic physics and the present state in relevant works of the functional devices that were investigated in this work. Currently the largest obstacle to the demonstration of an all-metal LSV device for on-chip functionality is the poor injection and operation efficiencies that are otherwise avoided in current CMOS technology. One method of overcoming this barrier would be the improvement of device characteristics by the selection of highly spin polarised materials, such as Heusler alloys [83], as the injector and detector materials. However, through the structural effects described in this chapter it should be possible to not only improve the operational efficiency of such devices but introduce novel functionality to LSV devices.

Chapter 3

Experimental methods

Electronic spin is a quantum mechanical phenomenon. Although it may correlate to form an ensemble of spins, the length scale over which this occurs is of the order 1 μm [26]. For the investigation of any such small scale phenomena the size of the investigative system, the devices, should be below this limit. Ideally they should be of the order of a few hundred nanometres. Not only are the length scales small in magnitude, the energy scales are also small. For illustration, it is well known that the spectral lines of hydrogen are closely spaced doublets. The splitting corresponds to an energy difference of approximately 8×10^{-24} J (5×10^{-5} eV) between the electron spin up and spin down states. This gives some feeling for the magnitude of the phenomenon that it is hoped can be observed. As a consequence of the magnitude of even correlated electron phenomena, one must be mindful of noise and any erroneous current discharge that may affect the measurement or even destroy the devices.

3.1 Device fabrication

3.1.1 Lithographic process

Nano-scale features can be fabricated by an electron-beam lithographic processes. Lithography is the use of radiation to draw customised shapes in radiation sensitive resists. There are two forms of lithographic process; an additive "lift-off" process and a reductive etching process. The lift-off lithography process involves depositing a polymer resist layer onto a substrate and making a stencil through which, for example, a metallic layer can be deposited. The polymer stencil may then be removed by a solvent to leave the metallic nano-features on the substrate.

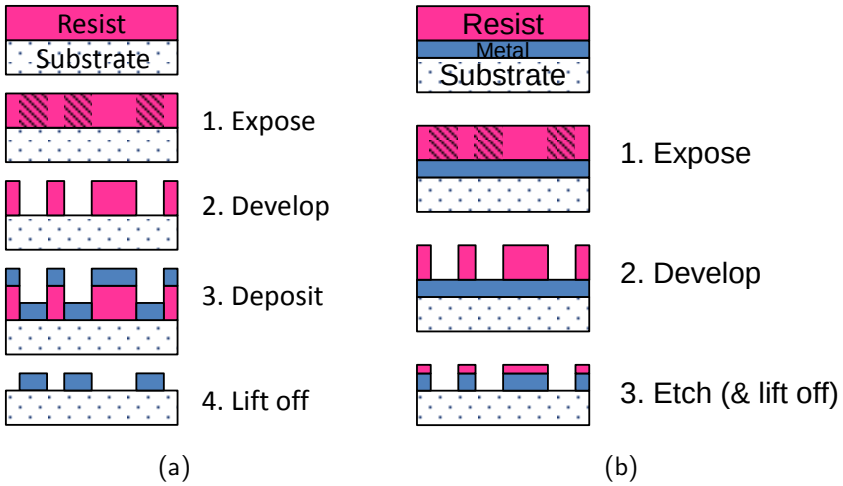

Figure 3.1: (a) The lift-off lithography process and (b) the reductive etching lithography process. The shaded regions are those exposed to radiation.

The two forms of lithography are outlined in figure 3.1. Both lithographic schemes involve changing the chemical structure of a polymer resist so as to make them more or less soluble in a solvent. By its nature, lithography therefore requires specific resists for specific radiation – see table 3.1. For the lift-off process, exposure to radiation breaks non-soluble long chain polymers into shorter soluble chains, *i.e.* radiation causes chain scission. This type of resist is known as a positive resist. For reductive etching lithography, exposure to radiation causes cross linking of long chain polymers. This causes the area exposed to radiation to become less soluble. This radiation and chemical sensitivity allows the selective removal by a developing agent – see table 3.1 – to create troughs through which a metal layer can be deposited directly onto the surface of the substrate as shown in figure 3.1. This is an inherently dirty process compared to normal high vacuum or ultra-high vacuum thin film metallic deposition processes. Therefore, care must be taken to limit contamination of the surfaces.

Lift-off lithography was the preferred process used in this study. Generally positive resist processing results in a higher contrast than negative resist processing [84]. For the style and nature of the devices planned, reductive fabrication also requires more complex processing techniques. In addition to the versatile electron beam evaporation deposition system, it requires equipment such as reactive ion etching chambers and end

Layer	Resist	Developing agent	Lift-off agent
Nano-features	1:1 ZEP:Anisole	N50	Cyclopentanone
Cr/Au contacts	LOR3A/S1813	MF319	Acetone

Table 3.1: List of resists, developing agents and lift-off agents used for device fabrication in this study.

point detection.

3.1.2 Electron beam lithography (EBL)

The advantages of EBL are the sub-5 nm resolution of features that can be achieved [85] and that the technology for achieving a probe that can do so already exists. A scanning transmission electron microscope (STEM) column produces a highly focussed electron beam with a Gaussian profile. The electron beam penetrates the resist layer and a number of scattering events occur. This causes the exposed area to be larger than the probing beam itself leading to a reduction in contrast in the resist layer.

As electrons pass through the resist elastic forward scattering events cause the beam to broaden. After the resist layer the electron beam enters the substrate. Backscattered electrons from the interaction volume within the substrate cause what is known as the proximity effect [86], where backscattered electrons from one feature react with the resist to reduce the contrast in a neighbouring feature. The solution is the use of a high energy electron beam ($\leq$50 kV). Firstly, the broadening due to forward scattering in the resist is reduced. Secondly, given that the interaction volume is proportional to the cube root of the beam energy the interaction volume within the substrate is increased. By increasing the interaction volume in the substrate the density of the cloud of backscattered electrons decreases. This diminishes the contrast reduction in neighbouring features as shown in figure 3.2(a).

A base electron beam dose of 1.9 C/m^2 was set as the standard, idealised for a range of 50% filled patterns in 1:1 Chloromethyl Acrylate Copolymer : Methoxybenzene resist (ZEP-520A:Anisole). The filled patterns were chessboard and line patterns with features down to 50 nm. Depending upon the feature proximity, size and shape the dose was adjusted. Typically for the devices produced in this study 1.5 times the base dose was used. A resist dependent pre-exposure bake was used to evaporate any excess solvent in the resist. After the exposure step the resist was baked again to generate cross-linking to harden further the unexposed resist. By this method the contrast between those areas that were and were not exposed was improved. The exposed resist was then developed by placing the sample in a bath of n-Amyl Acetate (N50) developing solvent, see table 3.1. The resist dependent developing agent removes the resist material that has been made more soluble by the irradiating electron beam. To improve the possible feature sizes at this stage the samples were placed for $<$5 s in an ultrasonic bath at the lowest power setting for a part of the development step. This helps to break additional bonds in the polymers that have been weakened by radiation. As a result broadening of the channel towards the top of the resist due to long development times was reduced. A metal or

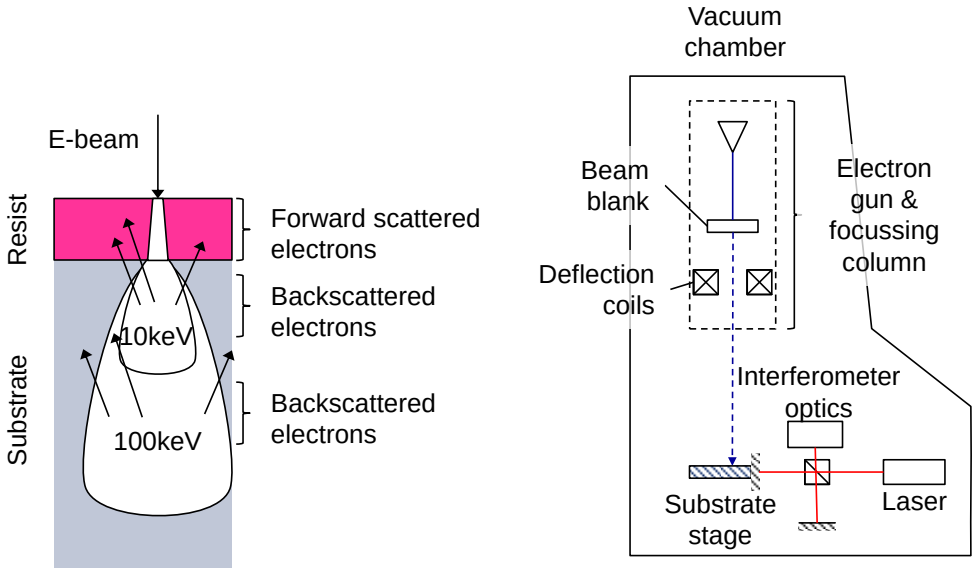

(a) (b)

Figure 3.2: (a) Diagram of the electron beam interaction volume and (b) simplified drawing of the JEOL JBX-6300FS EBL system.

other material may now be deposited onto the substrate. The final processing stage is the lift-off of the remaining resist, taking any superfluous metal with it. The lift-off agent is, again, resist dependent. A short ($\simeq$5 s) burst in an ultrasonic bath helped to remove any remaining metal. This process was repeated for as many layers as necessary for the required nano-structure.

3.1.3 EBL system specifications

The system used for the exposure step was a JEOL JBX-6300FS EBL system, a representation of which is shown in figure 3.2(b). The system specifications are outlined in table 3.2. The JEOL JBX-6300FS is capable of writing features down to 5 nm. Although the EBL system is very sophisticated, it is in principle simple. The system consists of

Electron gun type	Schottky
Acceleration voltage	Up to 100 kV
Max. wafer size	200 mm
Max. field size	200 µm$\times$200 µm
Overlay accuracy	$\leq$9 nm
Field stitch accuracy	$\leq$9 nm
Scan speed	Up to 50 MHz

Table 3.2: Summary of the EBL system specifications [87].

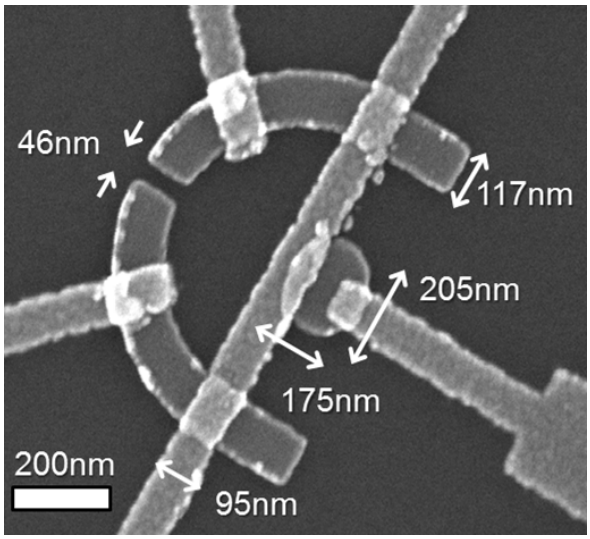

Figure 3.3: Scanning electron micrograph of a typical device to illustrate the dimensions that can be achieved. The device was fabricated by Dr. A. J. Vick and measured as part of this work.

electron beam column lifted almost directly from a scanning transmission electron microscope (STEM). A Schottky emitted electron beam is focussed through a series of magnetic lenses onto a substrate that is mounted on a stage. On the surface, at the four corners of the substrate global alignment marks were used. These were typically 800 μm × 5 μm. The coordinates of the alignment marks were inputted so that the system could automatically locate local alignment marks of smaller scale. These were typically 40 μm × 10 μm and more centrally located. The beam passes in a raster pattern over the mark at a scan speed of up to 50 MHz, correcting for rotation and position. This allowed for an overlay accuracy of $\leq \pm 9$ nm – a necessity for device fabrication. A typical device can be seen in figure 3.3. The Permalloy horseshoe and ellipse were the first features to be deposited and the straight Copper contacts were overlaid. Here the uniformity of feature sizes across a wafer of devices varied by no more than 5% . The observed overlay accuracy across different batches of the same device is observed to be of the order ± 5 nm.

3.1.4 Electron beam evaporation

Electron beam evaporation is an established form of metallic deposition. A crucible of material is placed in the path of an electron beam under the influence of an accelerating voltage in the range 5-10 kV. This leads to temperatures in the region of 3000 K, enough to evaporate most metals. Further discussion of the thermodynamic and atomistic processes are given by Maissel and Glang [88] but will not be discussed here.

During electron beam evaporation a localised electron beam is steered onto a source metal by permanent magnets so that only the metal is heated to evaporation temperatures. Evaporated materials are deposited on everything within the evaporation cone of the metal at a higher rate, typically 0.2 nm/s, and with a lower kinetic energy than sputtering. This reduced the damage caused by heating the resist layer during deposition, for example the deformation temperature for Polymethyl methacrylate (PMMA) is approximately 250 K (80°C). Heating to above these temperatures would cause cracking in the resist, reducing the minimum feature size and inhibiting a clean lift-off stage. The system used for metallic deposition was an Oerlikon Leybold Vacuum Univex 350. The system was operated at a base pressure of 5×10^{-5} Pa and deposited materials at a typical pressure of 1×10^{-4} Pa. The standard structure for the e-beam lithographically defined structures was 30 nm thick Permalloy and 70 nm thick Copper. The Copper layer led away to peripheral contact pads. From these contact pads optically defined layered contacts of 5 nm thick Chromium underneath 145 nm thick Copper lead to the edge of the sample (see section 3.2.2).

3.2 Optical lithography and sample preparation

Generally three devices were patterned at the centre of a 3 mm × 3 mm sample by EBL. As the final Copper device layer was patterned and deposited peripheral, 10 µm square contact pads were also patterned, as shown in figure 3.4. This section describes the steps that were required to prepare the devices for operation and measurement. The samples were prepared so that they could be mounted in chip carriers. By preparing the

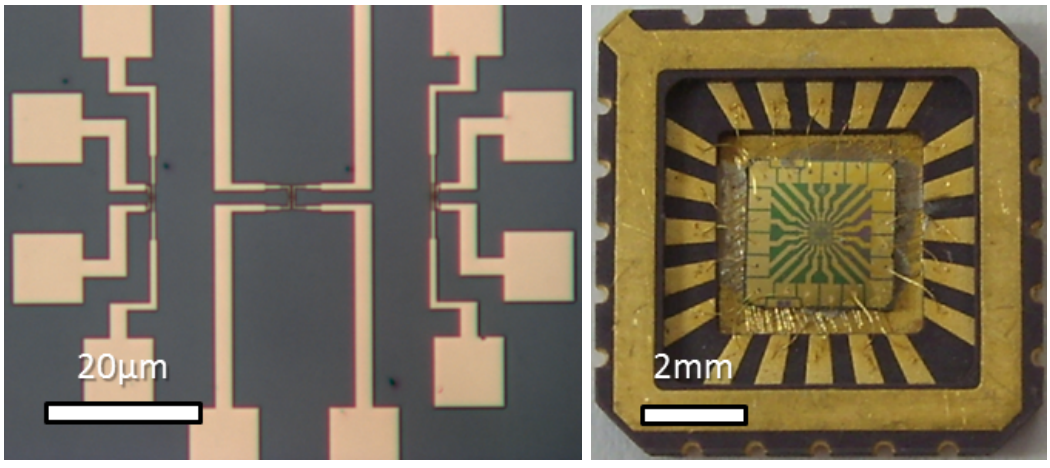

(a) (b)

Figure 3.4: (a) Optical microscope image of the device with a peripheral contact layout and (b) sample mounted in a chip carrier.

samples in this manner a wider range of variables were at hand. Using a 20-pin chip carrier and socket the samples could be measured in vacuum, at low temperature and under a variety of external magnetic fields.

3.2.1 Optical lithography of contacts

From the peripheral contact pads further contacts and wires branched out to the edge of the 3 mm square sample. The optical radiation that was used was in the ultra-violet region of the spectrum with a wavelength range between 350 and 450 nm. The feature size was therefore limited in this process to roughly 500 nm. The optical lithography step was used for the fabrication of the large Chromium (5 nm)/Gold (145 nm) wires and contacts to which wires could be bonded. Chromium was used as the base layer for these bonds as it improved adhesion to the substrate. An EVG 610 semi-automated bond alignment system was used in which the fine rotation and $x-y$ alignment were adjusted by manual, precision micrometer control. The contacts were deposited by electron beam evaporation as explained in section 3.1.4. Table 3.1 gives the resist and developer used for the Chromium/Gold contacts.

3.2.2 Wire bonding and sample mounting

Nine samples were patterned onto 16 mm^2 SiO_2 substrates which were cut by diamond scribe and fractured into 3 mm square samples. The samples were typically covered by a protective resist layer during scribing. The samples were subsequently mounted into chip carriers, as in figure 3.4(b), using Silver paint. Around the edge of the carriers were Gold contact pads to which contact with the sample was made by 25 μm diameter Gold wire. The wires were bonded by wedge bonding, as opposed to ball bonding which uses a high voltage to weld the wire to the sample thus damaging the samples. A wedge bonder uses heat, ultrasonic power and force to bond the wires to the edge of the chip carrier and the sample contact pads. Once the samples had been wire bonded to chip carriers they were mounted in a chip carrier to undertake electrical measurements.

3.3 Sample probe

From initial trials it became apparent that the nano-devices that were fabricated were susceptible to electrical damage. The electrical damage could be from a static discharge or simply from the steady state application of a probing voltage. For example, the

application of a 1 mV potential difference across a 100 nm gap produces an electric field of 10 kV/m. The electric field will be increased around corners and sharp features. In general the dominant discharge process from an anode is by gas multiplication. However, at lower pressures and smaller feature sizes the dominant process becomes field emission from asperities and corners on the anode surface [89]. Therefore, a vacuum compatible probe was designed for sample testing. The chip mounted samples were placed in a 20-pin chip holder as shown in the inset in figure 3.5. In this manner the devices were mounted, tested, removed and replaced with ease. A diagram of the vacuum probe design is shown in figure 3.5 where the cavity was pumped down to a typical pressure of 5×10^{-6} Pa during electrical measurements.

Other steps were taken to counteract the destruction of samples by static discharge. Antistatic wristbands connected to ground were worn to avoid this whilst handling the devices. During the fabrication process the LOR3A layer was left on as an electrically insulating barrier between wires. This did, however, render the devices invisible under SEM. 90° corners were avoided in device design to reduce breakdown by field emission. As well as this a vacuum probe was made to ensure that there could be no electrical breakdown as described by the Townsend regime [89], where avalanche multiplication occurs in the presence of a sufficient electric field.

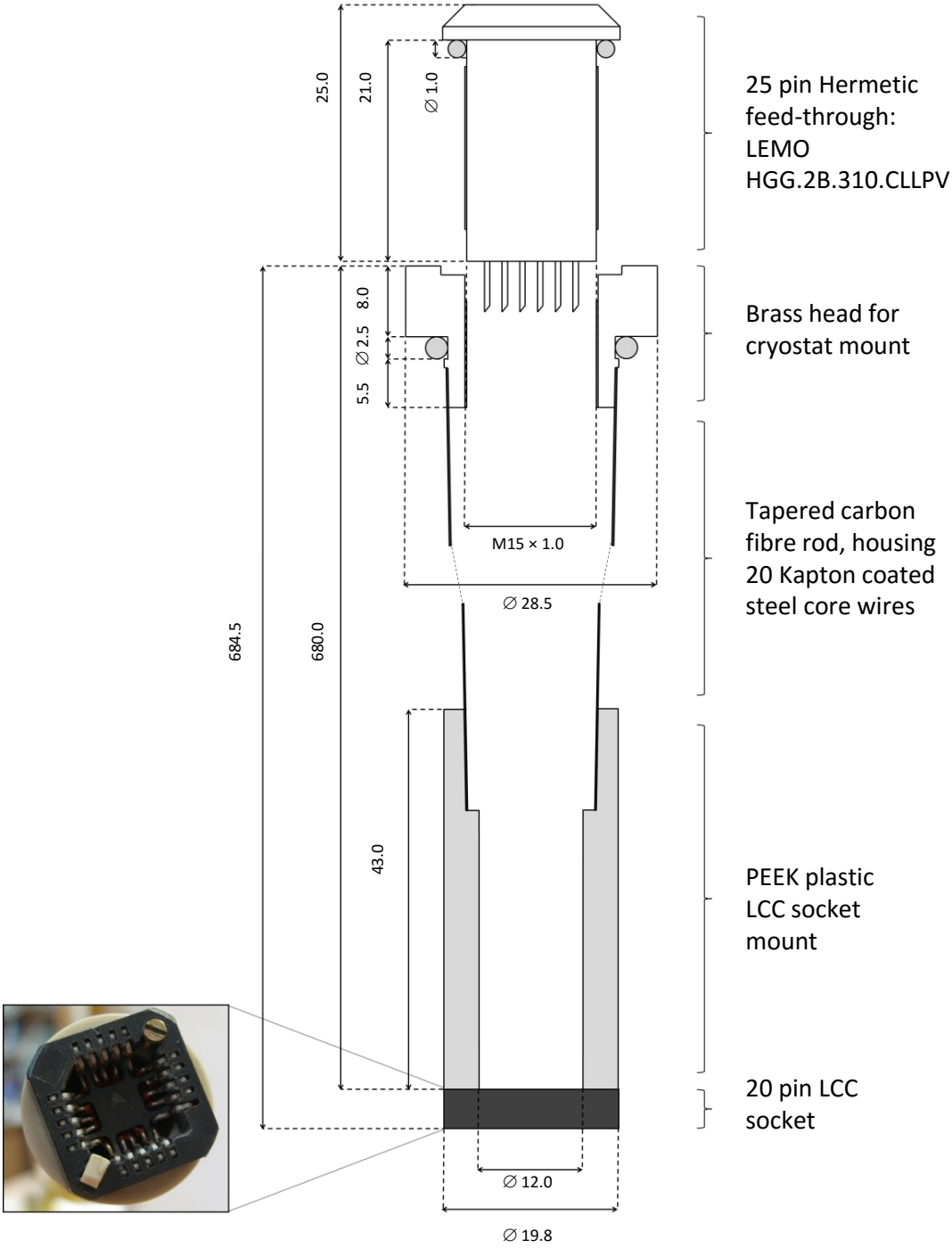

Figure 3.5: Vacuum probe design. The inset shows the twenty-pin leadless chip carrier socket. A LEMO® hermetic feed-through was used with a Brass, Carbon fibre and Polyether ether ketone (PEEK) composite rod which terminated in a leadless chip carrier (LCC) socket. The probe was designed as part of this project and was manufactured in the workshop at York.

3.4 Electrical measurement

For spintronic device applications [70–73] the magnitude of the measured spin current must be maximised. This can be achieved in two ways: by optimising the growth conditions and the materials used at the accumulative interface or by reducing the dimensions of the system being studied. The latter was taken as the intended approach.

3.4.1 Sources of error

There are two main systematic errors that were considered when designing the experimental set-up. In any electrical measurements it is impossible for the equipment itself to be remote from the measurements. This manifests as a parasitic resistance. The resistance of the coaxial/triaxial leads and junctions in the circuit that connect to the device contribute to this. There is also a systematic offset due to the Galvani potential. Considering two metals with different chemical potentials, at the interface of these metals the Fermi levels are shifted to meet at an equipotential. However, outside the interfacial region the chemical potential for each material is likely to be different. This will result in an offset voltage. The Galvani potential is especially apparent in a non-local measurement regime.

Sources of noise

To reduce the sources of random error consideration was paid to their origin. Johnson-Nyquist noise is generated by thermal agitation of electrons within a resister irrespective of the voltage applied [90]. The root mean square (r.m.s.) noise voltage is given by

$$V_{\mathrm{j}} = \sqrt{(4k_{\mathrm{B}}TR\beta)} \tag{3.1}$$

where k_{B} is the Boltzmann constant, T is the temperature, R is the resistance and β is the bandwidth of the measurement. Substituting in the values; $T = 300$ K, $R = 100\ \Omega$ and $\beta = 10$ kHz the r.m.s. voltage is found to be 130 nV. Realistically, a 20 Hz low pass filter could be used for measurements taken at temperatures as low as 77 K. The Johnson-Nyquist noise level would in this case be reduced to 3 nV.

Beyond the characteristic thermally induced Johnson-Nyquist noise is a $1/f$ noise, also known as "pink noise". As the former implies this is a noise that varies as the approximate reciprocal of the frequency at which the measurement is taken. The relationship is given by equation (3.2), where γ is a system dependent constant that ranges

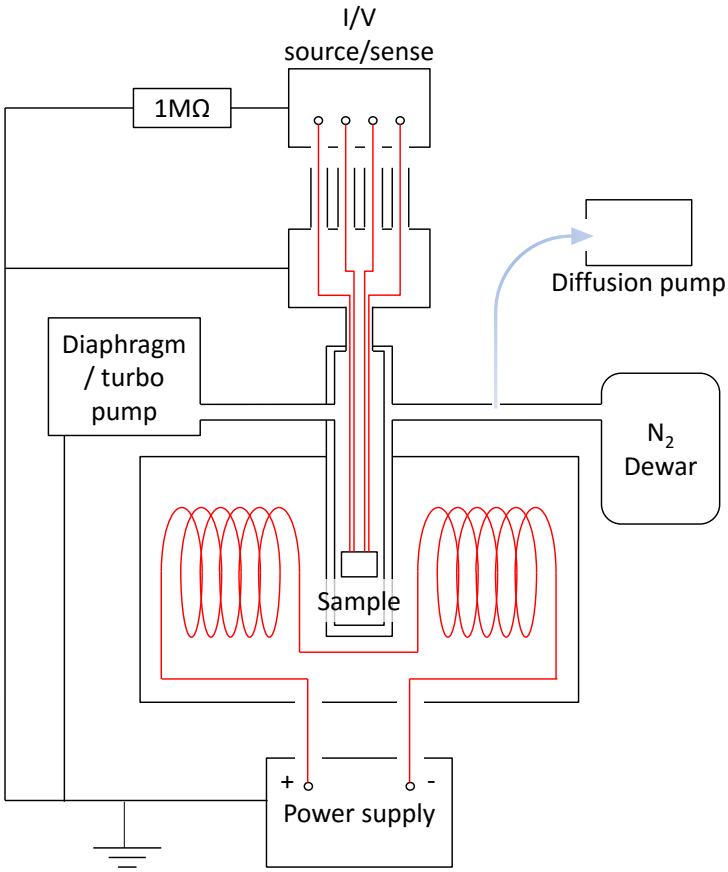

Figure 3.6: Block diagram of the device electrical measurement system.

between 0.8-1.4 [91].

$$V_{1/f} \propto \sqrt{(f^{-\gamma})} \tag{3.2}$$

$1/f$ noise has its origins in surface and bulk effects. In the materials deposited the noise will be from the bulk as well as the contact, injection and detection interfaces [92],

Shot noise originates from the discrete nature of a charge current. For macroscopic conduction this discrete nature is insignificant, *i.e.* the charge passing per unit time is immense compared to the unit electronic charge. In contrast with Johnson-Nyquist noise and $1/f$ noise which are frequency and temperature dependent, shot noise by mark of being discrete, is not so. One would not expect there to be any shot noise in the ballistic regime [93]. The only variable that can be changed to reduce the effect of shot noise upon a measurement is the charge carrier density. Increasing the magnitude of the current or reducing the system size to a scale where the transport will be ballistic counteracts the shot noise effect.

Transient and parasitic signals

The measurement system was set up as shown in figure 3.6 in an attempt to reduce transient and parasitic signals. The block diagram indicates how the system was grounded. Transient signals are due to high voltage impulses and pass through the ground of the measurement system. The source of the high voltage could be from a switch on laboratory equipment that shares the same ring main or from a higher voltage piece of equipment that is electrically further away but shares the same electrical ground at some point. To avoid damage from transient signals the devices were isolated fully from ground. An alternative method would be to attach a protection resistor to the device under test. Further efforts were made to reduce parasitic signals known as ground loops. If different parts of the system are connected to different potentials this will cause a current to flow. Everything in the system had a common ground or earth point to eliminate these. All of the I/V source/sense equipment used a built in 1 MΩ resistor between the measurement circuit and ground. This high resistance minimised any parasitic currents from ground loops and damaging discharge current from transient signals in the ground that could have affected the device under test through the current source.

3.4.2 DC local electrical measurement

For the four point interfacial resistance measurements a Keithley 2635 current source/voltmeter was used. There was no need to reduce the bandwidth or temperature for this measurement as typical interfacial resistances were tens of Ohms in magnitude. This, coupled with the current levels of up to 100 μA that could be supplied, allowed the measurement of resistance with a low signal to noise ratio. The resistance measurement was set up as shown in figure 3.7.

The first priority for characterisation of the devices was to confirm the presence of Ohmic contacts between the Permalloy and Copper layers. A simple sweep of the current and measurement voltage drop across solely the interfacial region determines the resistance of the interface. This is conventionally known as a four point probe technique and is a technique that was used to overcome the parasitic resistance from the measurement leads contributing to the resistance. A current was applied across the region as shown in figure 3.7, where the lead resistances are labelled in the diagram, and the voltage drop across the interface was measured to determine the resistance, R_{x}. As long as the lead resistances, R_1–R_2, are equal and smaller than R_{x} by two orders of magnitude or so, *i.e.*

$$R_1 \approx R_2 \approx R_3 \approx R_4 \ll R_{\mathrm{x}}\,. \tag{3.3}$$

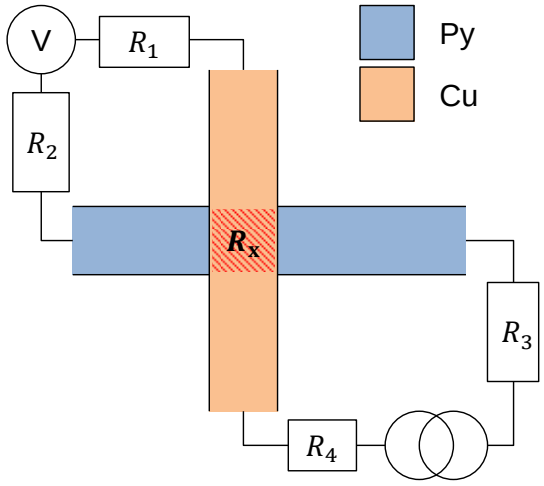

Figure 3.7: Schematic diagram of the four probe measurement technique.

It is safe to say that the resistance measured is R_{x} alone, highlighted in red in figure 3.7. In the general case this eliminates the main source of offset error.

3.4.3 DC non-local electrical measurement

For the detection of a pure spin current a non-local measurement was required, *i.e.* a voltage measurement separate from any charge currents. The mechanism for the generation of a voltage in the detector circuit is described in section 2.2.5. The quotient of the detected voltage by the injection current is known as the non-local resistance, R_{NL}. The characteristic change in this signal with a sweeping external magnetic field ranges from 0.1 to 5 mΩ in similar systems [16, 47, 49]. In microelectronics a commonly quoted current density limit for Copper is 1 MA/cm^2 which, working to this limit, would provide a signal change below 0.35 µV.

The method used for non-local spin current measurement was a DC reversal technique. A Keithley 2400 current source and a 2182a nanovoltmeter pair were used for the injection current and detection voltage. The source current was pulsed a number of times as alternating polarity pairs. The signal voltage, V_{signal}, measured at the peak current would consist of a non-local component, V_{NL}, and a background potential, $V_{\mathrm{background}}$, that would be due to any of the sources of error outlined in section 3.4.1.

$$V^{\pm}_{\mathrm{signal}} = {V_{\mathrm{NL}}}^{\pm} + V_{\mathrm{background}} \tag{3.4}$$

$$\text{where} \quad {V_{\mathrm{NL}}}^{+} = -{V_{\mathrm{NL}}}^{-} \tag{3.5}$$

The voltage pairs were combined as outlined in equation (3.6) to remove the background

component as the polarity of V_{signal} follows that of the input current.

$$\frac{V^{+}_{\mathrm{signal}} - V^{-}_{\mathrm{signal}}}{2} = \frac{(V^{+}_{\mathrm{NL}} + V_{\mathrm{background}}) - (V^{-}_{\mathrm{NL}} + V_{\mathrm{background}})}{2} = V_{\mathrm{NL}} \tag{3.6}$$

The voltmeter was operated with a built in digital filter that took a moving average of the signal as it was acquired. The moving average was taken over a window that was 100 measurements wide. If the signal moved outside 0.01% of the moving average of the voltage the reading was ignored and taken again. The 2182a was also equipped with a power line cycle integration filter. To improve accuracy the signal was integrated over 1 to 5 cycles of the power line frequency (50 Hz) depending upon the acquisition speed required. The input current was pulsed at a low frequency of 4 Hz which, whilst remaining close to DC with respect to transport properties, allowed for some reduction in $1/f$ noise. It was possible to use an analogue first order, low pass filter with a cut off frequency of 18 Hz at the expense of measurement frequency. This was avoided to reduce the measurement acquisition time, which was typically 25 s per voltage measurement.

In summary, the culmination of the development of a nanovolt electrical measurement system has been described in this section. The devices that were measured in this work were extremely delicate. Lengths were taken to reduce the risk of damaging the devices by static discharge. It was found that the best way to reduce this risk and to lower the noise level of the measurements taken was to take the measurements overnight. At this time the ground was free from transient noise from other equipment and the drift attributed to microvolt variations in the ground electrical potential were also avoided. The equipment was isolated and grounded to the best extent possible. However, there is still room for improvement to the electrical shielding of the sample itself during measurement. This is the next step that should be taken to improve the measurement system.

Chapter 4

Device geometry and operation

Unlike an electron charge, an electron spin cannot be observed easily on the macroscopic scale. The physical measurement of spin transport phenomena is largely confined to scales below the characteristic length: the spin diffusion length, λ_{S}. For non-magnetic transition metals λ_{S} is typically less than 1 μm at room temperature [94]. It was not until device fabrication reached a more advanced, nanometre level that spin transport phenomena could be investigated thoroughly [16]. Outlined in this chapter are the device geometries proposed for the investigation of electron spin processes.

This was the first project at York to extensively investigate spin-diffusion phenomena using the electron-beam (JEOL JBX-6300FS EBL) system. As such, significant work was undertaken by Dr. A. J. Vick to optimise the fabrication process. In order to do this in a systematic manner the characterisation of the fundamental spintronic and electronic properties of the devices was necessary. This chapter, therefore, describes the device development that was undertaken and the characterisation of the basic operability of the devices. In chapter 5 the actual device performance of those successfully fabricated is discussed.

4.1 Ladder devices

"Ladder" devices were fabricated to gain resistivity information about the materials on the scale that they were being used and to develop the direct current (DC) reversal measurement system. The schematic for the devices is shown in figure 4.1(a). They were designed to allow a number of four-point probe measurements to be made over a range of different channel lengths. This was undertaken to avoid affects from corners where the channels cross. This way, solely information about the straight wire section

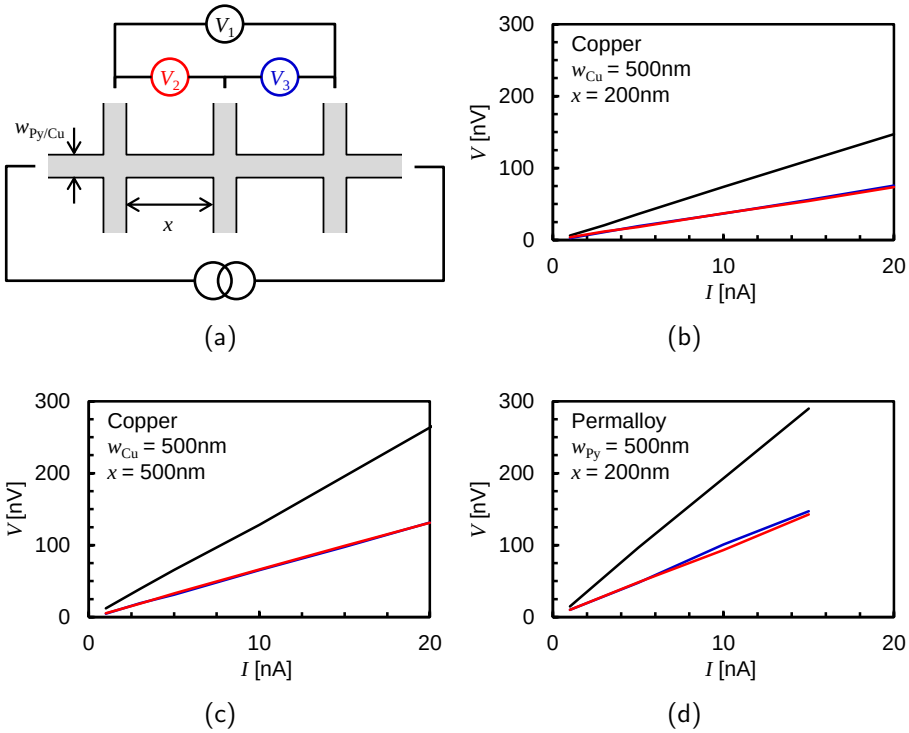

Figure 4.1: (a) Schematic of the Copper and Permalloy resistivity measurement and (b) to (d) results for Permalloy and Copper bars of varying width and separation.

was gained. They were fabricated to be of width, $w_{\mathrm{Py/Cu}}$, 500 nm, 200 nm and 100 nm. The distance between the probing wires, x, was 200 nm and 500 nm. The thicknesses of the Permalloy and Copper layers were 30 nm and 10 nm. Unfortunately during the fabrication process some of the samples were damaged, either physically or by electrical discharge through sample handling, preparation and measurement. Therefore, only a selection of the anticipated range of dimensions could be probed.

Measurements were made using the DC reversal technique discussed in section 3.4. A schematic diagram of the measurement is shown in figure 4.1(a) and the data are shown in figures 4.1(b) to 4.1(d). The data shows that the resistivity of the Copper nanowires using the electron beam evaporation and processes outlined in chapter 3 were (3.31±0.01) μΩ·cm and (2.66±0.04) μΩ·cm for the 500 nm and 200 nm wide bars respectively. For the Permalloy bars of width 200 nm the resistivity was (8.3±0.1) μΩ·cm, almost half that of values found in the literature. On inspecting the devices under SEM there was no apparent reason for this lower resistivity. Two possible explanations exist: that the nominal thickness dimension was inaccurate due to interfacial mixing, leading to an incorrect calculation of the thickness or that there was an improvement in the surface roughness in our devices compared to those elsewhere leading to a lower resistivity. The separations between the bars were taken as that at the metallic channel cross. A summary table of the measured resistivities and those found in the literature are shown

Material	Structure	ρ (μΩ·cm)
Copper (99.9999 %)	200 nm × 10 nm wires	2.66±0.04 (this work)
	500 nm × 10 nm wires	3.31±0.01 (this work)
Copper	Bulk	1.678 [95]
	50 nm thick wire	2.86 [16]
	100 nm × 80 nm wires	2.08 [49]
	100 nm × 54 nm wires	5.76 [47]
Permalloy	200 nm × 30 nm wires	8.3±0.1 (this work)
	500 nm or 800 nm × 40 nm wires	15.15 [16]
	100 nm × 30 nm wires	26.8 [49]

Table 4.1: Summary of the resistivities of polycrystalline Copper and Permalloy in this study and relevant literature. The dimensions stated are cross-sectional areas.

in table 4.1, where it is shown that the resistivities of the Copper devices fabricated in this study fall in line with those found in similar experiments. The resistivity of the Permalloy devices is lower than for devices of similar dimensions, by a factor of at least two.

4.2 Lateral spin-valves (LSVs)

LSV structures are commonly used for the investigation of spintronic properties. The method for spin injection in devices in this study was electrical, the principles of which are described in section 2.2.2. An LSV, shown in figure 4.2, is based on the principles of a conventional spin-valve multilayer but separates the stacked components laterally across a substrate. All devices were fabricated in the manner outlined in section 3.1.

4.2.1 Design

The ferromagnetic injector and detector pair in the LSV were Permalloy, shown in figure 4.2. To reduce the error in the low voltage states in the non-local measurement a well separated switching field was required. To ensure that there was a difference in the switching field for the two bars, one was fabricated with pointed rather than square ends as can be seen in figure 4.2. Domains will be nucleated at any asperities on the surface of the bar, for example: corners. However, counterintuitively the addition of extra corners hinders the nucleation of reverse domains by reducing the demagnetising field that is transverse to the magnetisation direction. The addition of extra corners to hinder domain nucleation has been shown to change the switching field in similar Permalloy bars by as much as 360 Oe from 545 Oe (0 flat ends) to 185 Oe (2 flat ends) [96]. Bar

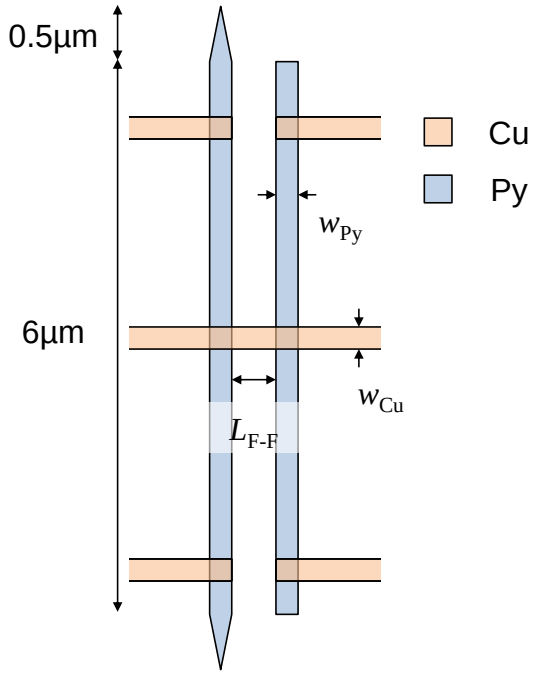

Figure 4.2: Lateral spin-valve design.

widths of $w_{\mathrm{Py}} = w_{\mathrm{Cu}} = 100$ nm, 200 nm and 500 nm were fabricated, scanning electron microscope (SEM) images of which are shown in figure 4.3. The length of the Permalloy bars (6 µm) was not changed. Although the aspect ratio for the bars will change the reversal dynamics, it has not been shown to affect the switching rate significantly [96].

4.2.2 Structure

The first layer, Permalloy, was fabricated to be 30 nm thick. Permalloy is 78 % Nickel and 22 % Iron. Permalloy has a 100 % spin polarised 3-*d* shell and a similar electronic structure to that of Cobalt and Nickel. The Nickel and Iron sites are distributed randomly across an fcc lattice and their potentials match, resulting in a low resistance for the majority spin channel, calculated to be 0.9 nΩ·m [97]. Furthermore, Permalloy was the preferred material for this study due to its corrosion resistance.

The second layer, Copper, was fabricated to be 70 nm thick so as to ensure full coverage of the Permalloy bar. Copper was the preferred material for this structure as high purity Copper (99.9999%) is readily available. It also adheres to Silica surfaces better than other materials such as Gold and has a spin diffusion length ranging from 0.29 µm at room temperature to 1 µm at 4.2 K [16, 47]. The samples were grown on thermally oxidised Silicon/Silica substrates. An oxidised substrate was chosen as it creates an electrically insulating barrier between the Silicon and the device. Thermally oxidised Silicon substrates also have an amorphous structure preventing the substrate

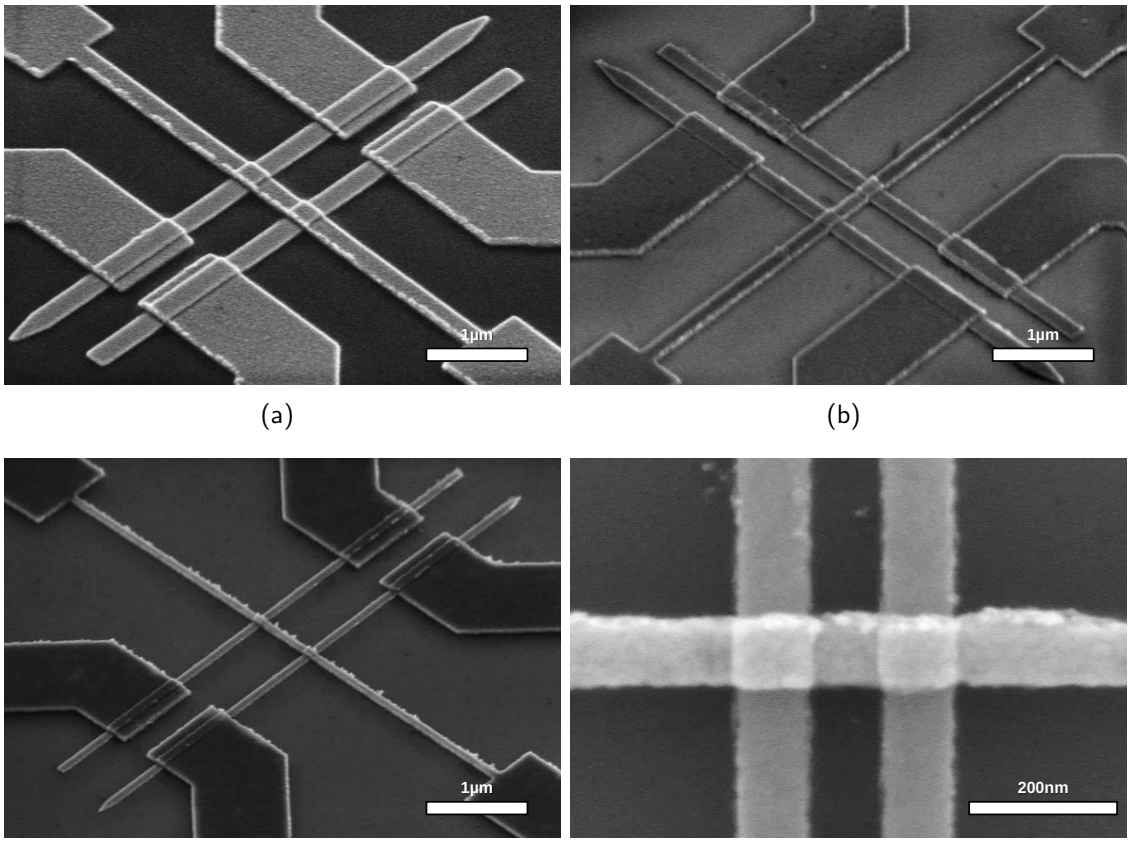

Figure 4.3: SEM images of lateral spin-valves with Copper and Permalloy width (a) 500 nm, (b) 200 nm and (c) 100 nm. (d) SEM image of the interfaces between Copper and Permalloy for $w_{\mathrm{Py/Cu}} = 100$ nm.

crystal habit affecting the structure of the Permalloy bars. This was required as the resistivity of the majority spin channel is extremely sensitive to the lattice constant [97].

4.2.3 Fabrication

A great number of devices were fabricated for this study (>3000), hence it was important to optimise the fabrication process. The first characterisation technique that was used was SEM. The samples were imaged to confirm the successful formation of micro- and nano-features. For the majority of the samples this was the case. If nano-feature (*e.g.* wires) production was not successful it was generally due to poor lift-off conditions. This was quickly resolved in the lift-off optimisation process. The formation of electrical contacts between lithography steps was of great importance. The most significant barrier to this was the poor adhesion of Copper to the substrate and to the Permalloy wires. This was thought to be due to residual anisole and other resist components from the development stage. Introducing an Argon plasma cleaning step before Copper deposition

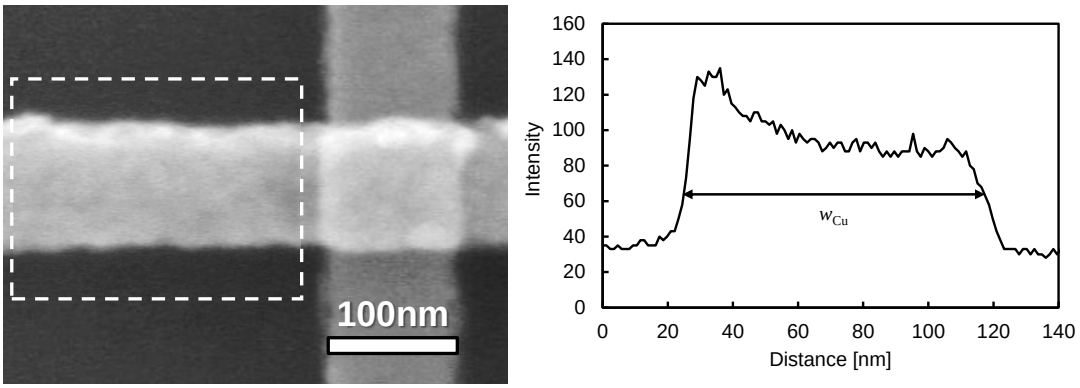

(a) (b)

Figure 4.4: (a) SEM image of a section of a Copper/Permalloy LSV interface and (b) an example of a pixel intensity plot across the Copper wire.

cleaned the substrate surface and removed any residue from the Copper trench to allow for better adhesion to the substrate and exposed Permalloy interface.

Beyond this, edge roughness and sample inhomogeneity were processing errors that were difficult to overcome. Edge roughness was a result of imperfect liftoff conditions and side-wall deposition. Side-wall deposition occurs when a metal is deposited and coats the sides of the resist feature trench. Upon lift-off, some of the deposited material remains giving the edges a slight "crown" feature. This can be seen in figure 4.4(b) where there is a clear edge feature on one side of the wire. Low power sonication was used for the effective metallic lift-off to reduce the occurrence of these features. However, some crowning was unavoidable. Inhomogeneity across the samples was also unavoidable. The interfacial resistances across the Permalloy/Copper interfaces ranged typically between 5×10^{10} Ω/cm^2 and 25×10^{10} Ω/cm^2. This was potentially due to a number of factors: The slight variation in interfacial area, the possibility of residue remaining between the layers and variations in the resistivity of the deposited material were all factors that became significant.

The roughness of the wires was calculated over a 100 nm length, a section of which is shown in figure 4.4(a). The SEM image was converted into a text file with each pixel represented by a greyscale value between 0 and 255, a plot of the greyscale values is shown in figure 4.4(b). For each pixel column in the x direction the average high and low values were computed. The midpoint of these values was taken to be the wire edge and the distance in nanometres between the edges calculated. From this the mean and r.m.s. values were calculated to be 87 nm and 2.6 nm respectively, for a Copper wire intended to be 100 nm wide.

The confirmation of the presence of Ohmic contact between the Permalloy and

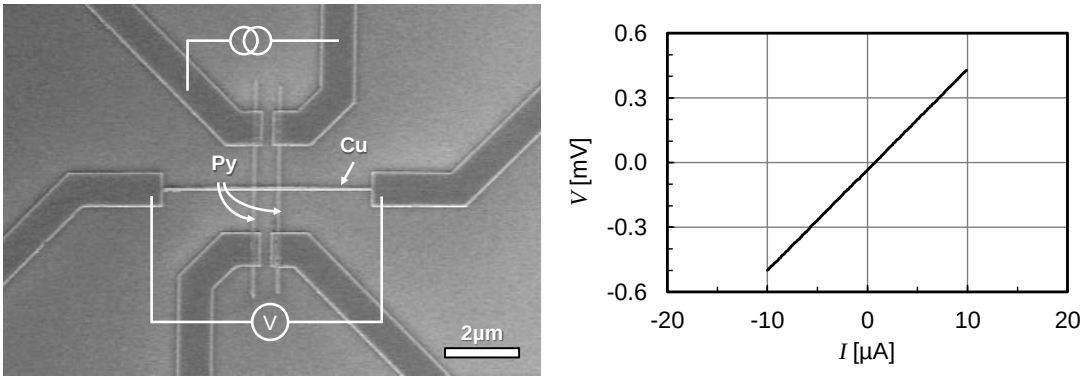

(a) (b)

Figure 4.5: (a) Diagram of the four point interfacial/channel measurement and (b) a typical I-V measurement for a $w_{\mathrm{Py/Cu}}$ =100 nm lateral spin-valve with a 200 nm bar separation.

Copper channel was achieved by a four point measurement technique, outlined in section 3.4.2. The measurement was set up so that the two interfaces and Copper channel were probed, as shown in figure 4.5(a). The measurements undertaken on $w_{\mathrm{Py/Cu}}$ =100 nm lateral spin-valves, LSVs, are presented. The intention was to measure the resistance of two Permalloy/Copper contacts and the intermediate Copper channel. By varying the distance between the Permalloy bars it was hoped that the average resistance of the interfaces could be extracted by fitting a straight line and extrapolating to a distance of 0 nm between the ferromagnetic bars. A table of the results for various channel distances are shown in table 4.2.

From this it can be clearly seen that there is little or no correlation between the channel width, $L_{\mathrm{F-F}}$ and the resistance. This demonstrates that the magnitude of the

	R (Ω)	
$L_{\mathrm{F-F}}$ (nm)	$w_{\mathrm{Py/Cu}}$ = 200 nm	$w_{\mathrm{Py/Cu}}$ = 500 nm
200	46.52±0.06	-
	152.72±0.09	-
300	225.5±0.3	77.35±0.05
	314.5±0.2	-
	81.02±0.03	-
400	49.39±0.01	34.21±0.03
	239.1±0.3	40.1±0.4
500	95.49±0.03	29.69±0.02
	105.14±0.04	-
	233.55±0.16	-
600	100.67±0.05	-

Table 4.2: Resistance values measured of the two interfaces and Copper channel for $w_{\mathrm{Py/Cu}}$ =100 nm lateral spin-valves.

channel resistance is much less than that of the interfaces and so the measured values can be taken to be the sum of the interfacial resistances. Indeed, for a 500 nm long, 100 nm wide, 70 nm thick Copper channel with a resistivity of (2.66±0.04) μΩ·cm, as measured in section 4.1, the resistance is (1.90±0.03) Ω. The measured values vary significantly, by almost five times for devices of nominally the same dimensions. Given this variation and the lack of correlation between resistances, measurements of this nature can only be considered an estimate of the interfacial resistance. By taking the values and halving them (as the measurement is of *two* interfaces and the intermediate channel of negligible resistance), the estimated interfacial resistances of the devices varied from (23.26±0.06) Ω to (157.3±0.2) Ω, the average being (74.7±0.1) Ω. The resistance-area (RA) product in this case is (2.988±0.004) Ω·μm^2 for the nominal dimensions if it is assumed that all of the injection takes place at the top surface of the interfacial region. The resistance-area product varies from 3.4×10^{-4} Ω·μm^2 (at 4.2 K) [98] in metal-metal junctions to 120 Ω·μm^2 [55] in metal/oxide/metal interfaces. The devices studied here sit in between these two extreme cases, which confirms the presence of interfacial contaminations as discussed above.

4.2.4 Operation

The intention was to use the LSV structure to selectively inject a spin imbalance into a Copper channel and open and close the channels in the detector circuit to investigate the electron-spin diffusion process. Conventionally spin-valve structures were fabricated perpendicularly layer upon layer [99]. The lateral lithographically defined structure allows for the isolation of a different body of physics, namely the geometrical phenomena of spin diffusion. The results described in the following section show the general characteristics of the non-local measurement that will be compared for different devices.

The detector circuit spin channel is opened and closed to the spin imbalance by sweeping an applied magnetic field in the plane of the sample in alignment with the Permalloy bars. To introduce a spin imbalance in the Copper channel, a low frequency (4 Hz) pulsed current was introduced across a Permalloy/Copper interface as shown in figure 4.6(c). A non-local voltage was detected across a similar Permalloy/Copper interface. The exact proposed device geometry was described in section 4.2.1. The dimensions that were varied, results of which are discussed in depth in section 5.1, are shown in figure 4.6(a). Being equal, the width of the Permalloy and Copper were varied, $w_{\mathrm{Py/Cu}}$ =500 nm, 200 nm and 100 nm. The larger device geometries of 500 nm and 200 nm width were fabricated to provide test samples for the development of the measurement process. The increased device size improved the resilience of the devices

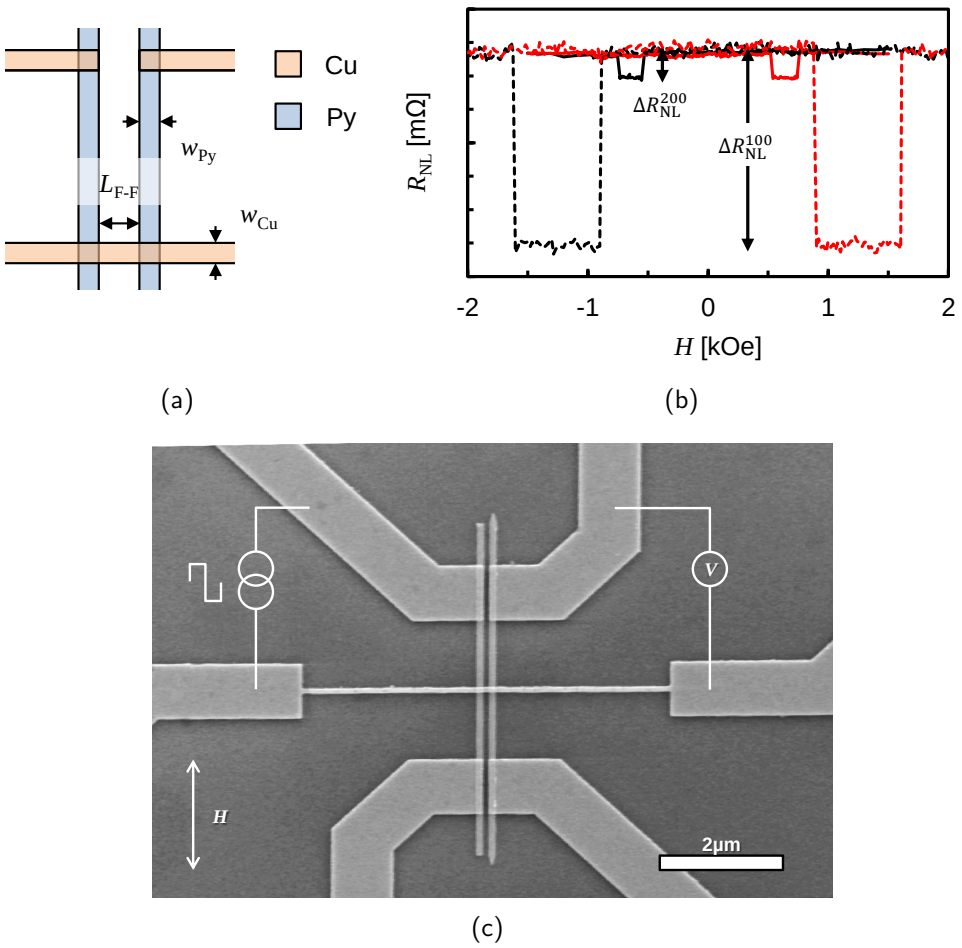

Figure 4.6: (a) Schematic of the lateral spin-valve structure, (b) typical non-local signal as a function of an applied field for $w_{\mathrm{Py/Cu}} = 100$ nm (dashed lines) 200 nm (solid lines) and (c) SEM image of the device and the measurement setup.

against destruction from handling and electrical testing.

The non-local signal as a function of field is shown for two samples in figure 4.6(b). The black lines represent the non-local signal as the applied field sweeps from positive to negative, and the red lines are the data from negative to positive. The solid lines show a measurement from a $w_{\mathrm{Py/Cu}} = 200$ nm and the dashed from $w_{\mathrm{Py/Cu}} = 100$ nm. The distance between the ferromagnetic injector and detector wires, $L_{\mathrm{F-F}}$ was varied between 600 nm and 100 nm. In the case of the signals shown in figure 4.6(b), both have a distance between the edge of the ferromagnetic wires of 200 nm. The two signals were obtained using different injection currents and are shown on an unmarked axis where the gradations represent a 0.25 mΩ interval.

Although one would expect that the change in the non-local resistance should remain the same, *i.e.* $\Delta V/I =$ constant from the model for injection discussed in section 2.2.5, the injection current has been shown to affect the detected change in

the non-local voltage [98]. Electrons passing into a bath of hot electrons do so with a reduced polarisation [100] and suffer a temperature dependent interfacial scattering [47]. Therefore the samples were probed with a different injection current of 50 μA and 25 μA for the 200 nm and 100 nm wide bars so that the current density through the injecting Permalloy and Copper wires remained constant at approximately 0.8 MA/cm^2 to reduce thermal effects at the injector. There are also thermal effects in the detector circuitry. There will be an increase in the temperature under the detector interface as a result of the injecting current. Therefore in the probing detector circuit there is a thermally induced voltage between the detector and the extremities of the Permalloy wires.

The change in the non-local resistance, R_{NL}, is comparable between the two devices. The initial values of R_{NL} were (21.681$\pm$0.001) mΩ and (30.687$\pm$0.002) mΩ. The change in R_{NL} was (0.18$\pm$0.01) mΩ and (1.45$\pm$0.01) mΩ for the devices of channel width 200 nm and 100 nm respectively. The dominant factor behind the difference in ΔR_{NL} is the difference in injection efficiency between the two samples. It is well known that the detected non-local signal is dependent upon the inverse of the cross-sectional area of the non-magnetic channel [48, 49, 101]. To reduce thermal effects on the spin injection the current density through the Permalloy wire was kept the same across the two sample sets as discussed above. However, there is a clear reduction in the change in the spin signal of a factor of eight, partly due to the reduction by four of the interfacial area.

The final characteristic of the two non-local signals is the difference in switching fields between the two devices. The reversal mechanism for a ferromagnetic nanowire is domain wall motion through the wire. A domain wall is nucleated at an area of increased transverse magnetic field [96], *e.g.* at a corner, discussed in more detail in section 5.1.1. A ferromagnetic injector and detector pair form a stable coupled magnetic configuration with a larger coercivity. In this case, the bar with the lower switching field (flat ends) had a coercivity that was increased by a factor of 3. The higher switching field (pointed ends) was increased by a factor of approximately 1.5 due to the stable anti-parallel magnetic alignment. Concerning the nanowires with a width of 100 nm the lower switching field was increased by a more modest factor of 1.1, compared to experimental results obtained by Chung and Hsu [102] in a similar system. In the samples fabricated in this work, the wire width changed but the wire length remained the same. Therefore, the anti-parallel magnetisation state would be more stable for the 100 nm wide wires than the 200 nm wide wires. Applying the Stoner-Wohlfarth model for a prolate spheroid, the coercivity increases as the inverse of the wire width, $H_{\mathrm{C}} \propto 1/w_{\mathrm{Py}}$ [102], which fell in line with the data obtained by Chung and Hsu, and is in agreement with the data presented here.

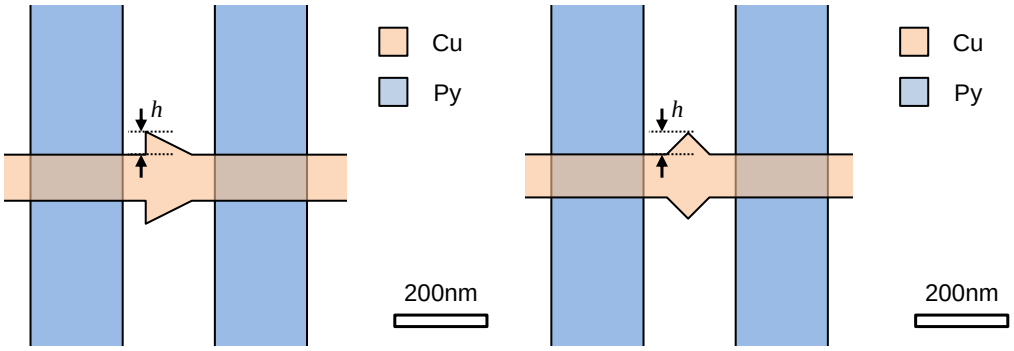

(a) (b)

Figure 4.7: Schematics of the (a) arrow and (b) diamond devices.

4.3 Spin signal amplification

A significant obstacle to the use of non-local spin-valves in spintronic applications is their poor efficiency at introducing a spin current into a non-magnetic material. Typically, non-local spin-valves have an spin injection efficiency that is three orders of magnitude lower than the local configuration counterpart [16]. One way in which this may be compensated is by the amplification of the spin signal in transit through the spin channel. Measurements undertaken by Abdullah *et al.* [60] found that the introduction of a geometrical asymmetry as shown in figure 4.7(a) into the spin channel resulted in an amplification of the spin signal by almost an order of magnitude.

To investigate the origin of the amplification observed by Abdullah *et al.* [60], LSV structures were fabricated with a diamond shaped structure in the Copper spin channel as shown in figure 4.7(b). The amplification that was observed was in devices with an asymmetric arrow shaped feature in the middle of the spin channel between the ferromagnetic injector and detector, shown in figure 4.7(a). The result was explained as a spin filtering process. The compensating charge diffusion currents experienced a different directionally dependent resistance. As the diffusion current is density dependent, a change in the channel dimensions will affect the diffusion. Because this change is directionally dependent, in a channel with an asymmetric geometry, one of the spin channels has an effectively increase current path and so an amplification was observed at the detector end of the spin channel. To confirm that this is a valid explanation for the effect a symmetric geometry, such as a diamond, was introduced into the spin channel.

SEM micrographs of the fabricated devices after electrical measurements were made are shown in figure 4.8. The narrowing of the vertical wires to the interfaces are due to Joule heating during the measurement. They are typical of the kind of damage

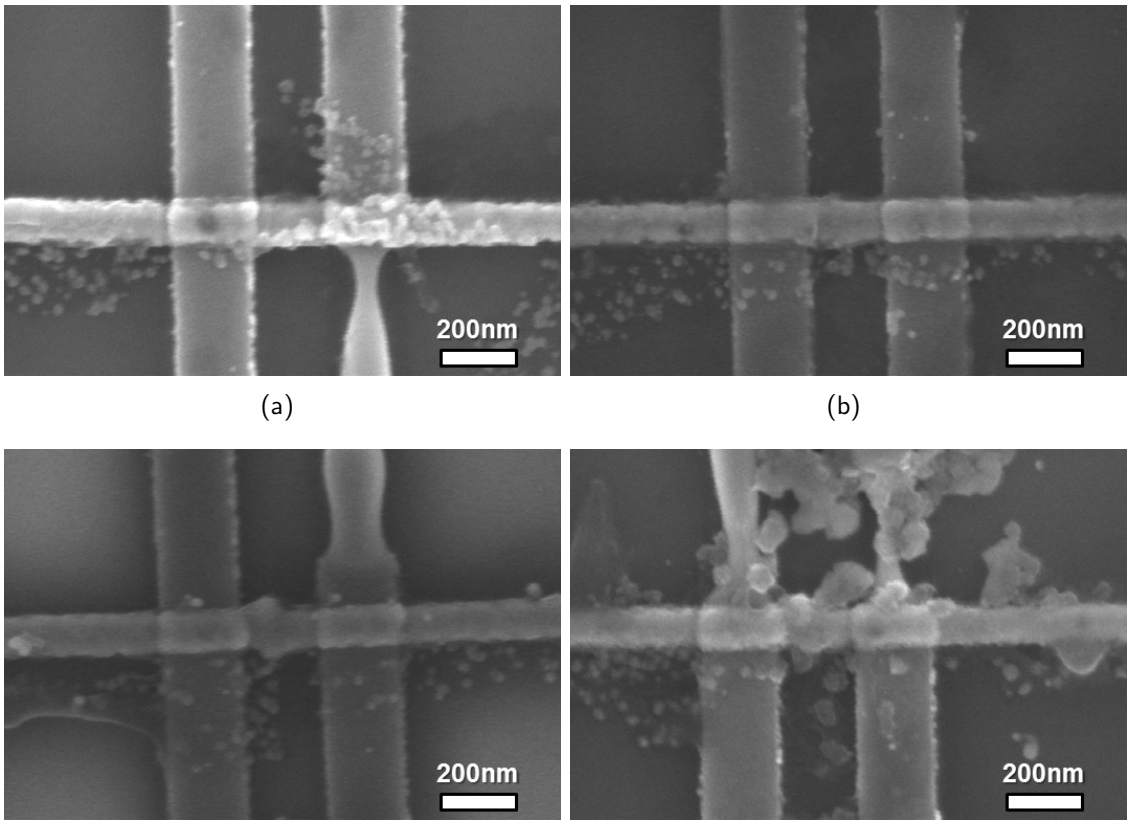

(a) (b)

(c) (d)

Figure 4.8: SEM micrographs of diamond devices with nominal height (a) 0 nm, (b) 20 nm, (c) 60 nm and (d) 60 nm. Some of the devices were damaged during and/or after electrical measurements were made.

caused to devices by the nature of the measurements. It was clear when this damage occurred during a measurement. With regard to the fabrication, complete lift-off was not always successful. Figures 4.8(a) to 4.8(d) shows debris at the lower edge of the Copper wire that occurred in some of the devices. To estimate the diameter of the debris particles, a bandpass and threshold filter was applied to an SEM image of the debris and particle analysis undertaken using ImageJ. Due to the filtering applied, the median diameter will be an underestimate of the particle size. The modal particle size was in the range 16 to 20 nm. More than 500 particles would need to be analysed for an accurate measurement of the distribution but insufficient particles were available from the SEM images. Approximately 100 particles were analysed. This debris is largely separate from the Copper channel and so it is not expected to have had a significant effect on the electrical measurements. In figure 4.8(d) there are much larger particles present. The origin of the debris is from the peeling-off and disintegration of the Copper channel during measurement as discussed in ref. [103].

As for the fabrication of well-defined diamond shapes, figure 4.8 shows that the diamonds were not entirely symmetrical. There was some offset between the upper and

lower wings on the edge of the channel. The true dimensions of the diamonds were not in line with the nominal sizes. The heights of the diamond shapes were 26 nm, 36 nm and 28 nm for the diamonds intended to be 20 nm, 60 nm and 60 nm respectively. The fabrication of well defined diamond features was not successful, as can be seen in figure 4.8. However, the geometry of Copper channel was successfully altered to widen and narrow in a symmetric diamond shape. The fact that these devices were not in line with the nominal dimensions is disappointing but will not affect the significance of the result. In order to improve the definition of the corner features within these devices a lower beam current would be required. The beam current used was 100 pA. This results in an overexposure of the resist in that region, broadening the exposed area. By reducing the EBL beam current to a value 40 pA as with other devices in this study, the edge and corner definition of these EBL features would be improved.

4.4 Spin interference

To provide additional functionality to LSVs a ring feature patterned in the spin-diffusion channel was investigated. This could allow for three terminal operation of an all-metal spin-valve in a similar manner to metal-oxide-semiconductor field-effect transistors (MOSFETs).

A ring geometry was introduced to split the spin channel into two paths and a current carrying bar patterned above the ring to introduce a magnetic gate operation, as shown in figure 4.9(a) and discussed in section 2.5.2. The ring devices were fabricated in the same manner as the LSVs. The current carrying bar introduced some restrictions to the device geometry. It was no longer possible to have one of the ferromagnetic wires with pointed ends at *both* extremities. Over the course of device measurement two geometries for the ferromagnetic wires were used. Firstly a square injector pad was attached to a shorter 1.5 μm ferromagnetic wire and later two bars of 6 μm length, one with points at one end, were used. The difference in geometry for one of the ferromagnetic pair would not have affected the injection or detection capabilities of the circuit as the injection and detection interfacial areas remained nominally equal. In anticipation of a current of tens of mA in magnitude being required through the current-carrying bar, sharp corner features were avoided in device design. Furthermore, the current-carrying bar was curved to increase the distance between it and the injection and detection wires, thereby decreasing the electric field strength and the probability of an electric discharge damaging the device. The measurement of the device is outlined in figure 4.9(a), with the operation of the gate being from application of a DC to the current carrying bar.

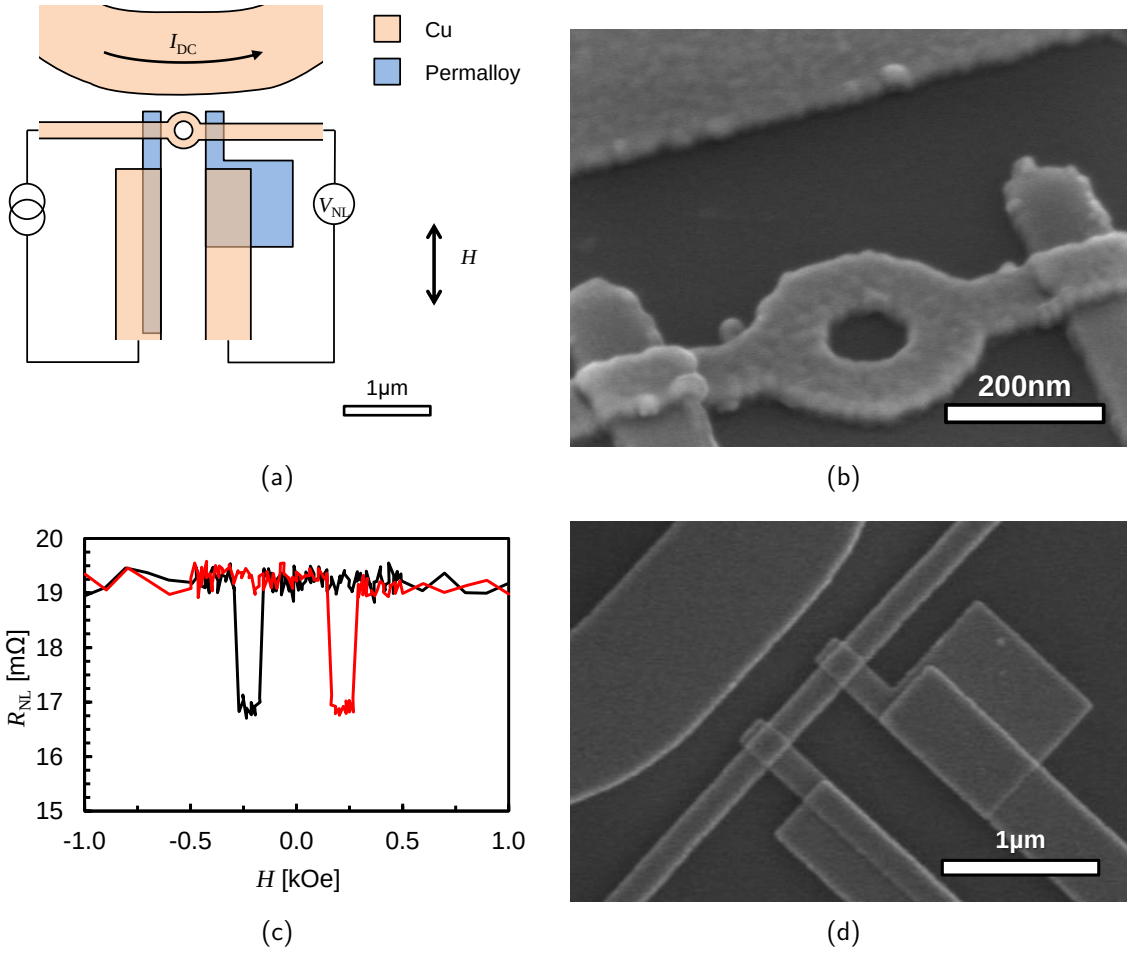

Figure 4.9: (a) Operation of the ring devices, (b) an SEM image of a typical ring device, (c) the non-local lateral spin-valve signal and (d) SEM image of a typical device intended to accommodate a split ring channel.

Lateral spin valve structures that accommodated a medial spin channel ring were fabricated. The width of the wires $w_{\mathrm{Py/Cu}}$ were 200 nm. The separation between the wires was 500 nm, to accommodate the ring geometry. The ring was patterned in the middle of the spin channel with an outer diameter of 450 nm and an inner diameter of 200 nm. The testing of the device structure for non-local LSV behaviour was undertaken. Devices were also patterned without a ring as shown in figure 4.9(d) and the same measurement made as for the LSV structures described in section 4.2.4. The non-local spin-valve signal is shown in figure 5.13. The switching field for both bars is significantly reduced from the values for LSVs of the same wire width. The upper switching field of the pair goes from (1.60±0.01) kOe to (0.27±0.01) kOe. This is due to the reduction in length of one of the ferromagnetic wires from 6 μm to 1.5 μm. This reduces the stability of the anti-parallel, flux-closure magnetisation, and therefore the switching field. This is likely due to the increased distance between the ferromagnetic bars, but also the significant reduction in the magnetic shape anisotropy of the detector bar in the ring geometry to that in the spin-valve geometry, *c.f.* figures 4.6(c) and 4.9(d).

To provide some kind of feeling for the type of field gradient required across the ring to cause destructive interference in the ring devices an order of magnitude calculation can be carried out. From equation (2.46), reproduced below for continuity

$$\mathrm{Re}(\lambda_{\mathrm{w}}) = \frac{\lambda_{\mathrm{S}}}{\sqrt{1+(\omega_{\mathrm{C}}\tau_{\mathrm{sf}})^2}}\,, \tag{2.46}$$

the condition for being able to observe an interference effect between the upper and lower channels can be calculated. Assuming that an interference effect will be visible with a difference in the spin diffusion lengths for the upper and lower channels of the order of $1/2$, interference will be observed when:

$$\frac{\lambda_{\mathrm{S}}}{\sqrt{1+({\omega_{\mathrm{C}}}^{\mathrm{upper}}\tau_{\mathrm{sf}})^2}} = \frac{\lambda_{\mathrm{S}}}{2\sqrt{1+({\omega_{\mathrm{C}}}^{\mathrm{lower}}\tau_{\mathrm{sf}})^2}}\,. \tag{4.1}$$

Here ${\omega_{\mathrm{C}}}^{\mathrm{upper(lower)}} = q_{\mathrm{e}}B^{\mathrm{upper(lower)}}/m_{\mathrm{e}}$, where $B^{\mathrm{upper(lower)}}$ is the perpendicular field in the upper (lower) channel of the ring. The approximation then reduces to

$$\frac{1+({\omega_{\mathrm{C}}}^{\mathrm{upper}}\tau_{\mathrm{sf}})^2}{1+({\omega_{\mathrm{C}}}^{\mathrm{lower}}\tau_{\mathrm{sf}})^2} \approx \frac{({\omega_{\mathrm{C}}}^{\mathrm{upper}}\tau_{\mathrm{sf}})^2}{({\omega_{\mathrm{C}}}^{\mathrm{lower}}\tau_{\mathrm{sf}})^2} \approx 4\,, \tag{4.2}$$

and so

$$\frac{B^{\mathrm{upper}}}{B^{\mathrm{lower}}} \approx 2\,. \tag{4.3}$$

So the condition at which one would expect to see a noticeable interference between the spin channels is when the field in the upper channel is approximately twice that of the lower channel.

But what of the magnitude of the perpendicular field? This is a relatively simple quantity to evaluate. The Fermi velocity of an electron in Copper is approximately 1.6×10^6 ms^{-1} and will takes approximately 0.3 ps to travel along the shortest path around the split spin channel. From equation (2.47) the phase of the electron is governed by a $\cos(\omega_{\mathrm{L}}t)$ relationship. Therefore, as an estimate with the wire is taken to be straight and of the shortest path length around a ring of 450 nm outer diameter and 200 nm inner diameter, to annihilate the spin signal in an electron traveling the shortest path around the ring structure the following approximate condition needs to be satisfied:

$$\frac{q_{\mathrm{e}}Bt}{m_{\mathrm{e}}} = \frac{\pi}{2}\,. \tag{4.4}$$

Substituting in the known values and t =0.3 ps, the field required for complete annihilation of the Hanle signal would be approximately 200 kOe. This is, however, the condition to completely suppress the spin signal through the Hanle interaction and the device is intended to operate as an interferometer. Therefore, so long as the condition that the

ratio between the fields in the upper and lower channels is approximately 2, the device may operate at fields well below this estimate.

4.5 Nano-motor devices

Spin torque oscillators were fabricated for the purpose of providing a "spin motor" [104] that could be used to couple to a magnetised body such as a magnetic nano-particle or as an electro-magnetic radiation detector. Furthermore the non-local lateral spin transfer nano-oscillator has the advantage, as mentioned in section 2.6.2, of a very large operating bandwidth, from 0 Hz up to, in principle, MHz or GHz frequencies. The design worked on the same principle as discussed in section 2.6.2. Two device structures fabricated are shown in figure 4.10.

The devices were fabricated in the same manner as discussed in section 3.1. The basis of the devices are the formation of a Permalloy injector pair with the discontinuous horse-shoe shaped features as shown in figure 4.10. The magnetisation of the Permalloy bars will couple across the gap which was measured to be 46 nm with a standard deviation of 2 nm across a batch of samples. Therefore, relative to each other, at the intersections with the Copper channel it was guaranteed that the relative magnetisations of the Permalloy wires at the interfaces were antiparallel. The switchable magnetic entity was an ellipsoid of Permalloy. The exact dimensions of the ellipsoid will have an effect upon its magnetic structure. The ellipsoid was formed from the outline of two semi-circles separated by a distance with the resulting gaps closed by a straight line.

The effectiveness of this fabrication process was examined using an SEM. Examples of these images are shown in figure 4.11. The nano-oscillator devices are a good

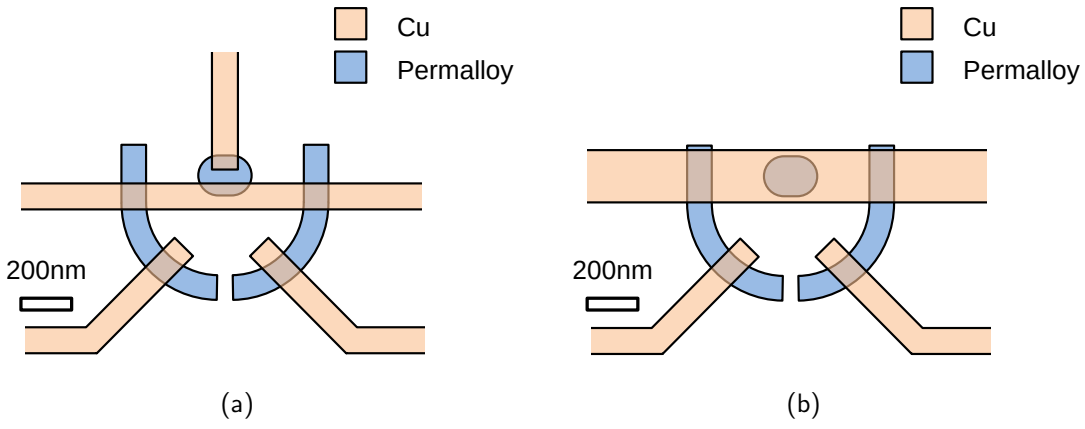

Figure 4.10: Device schematic for the spin-transfer nano-oscillator in an (a) detection and (b) operation geometry.

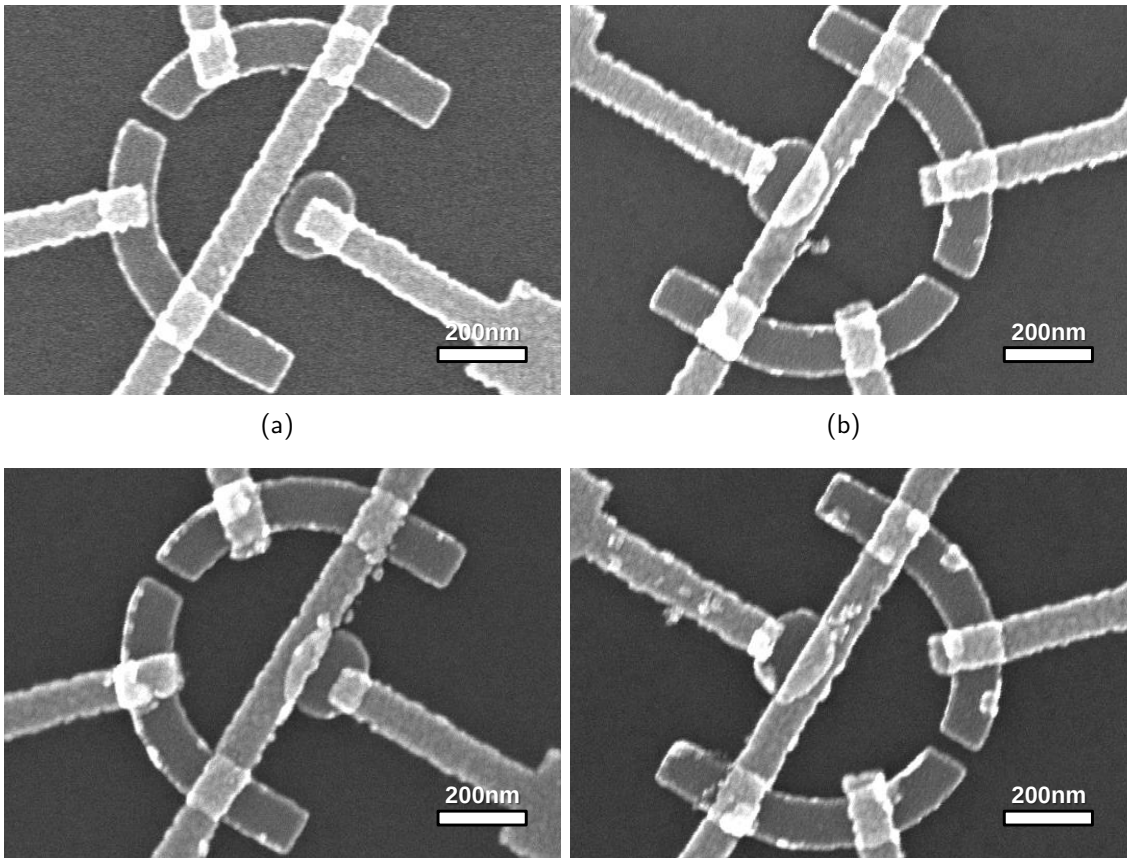

(a) (b)

(c) (d)

Figure 4.11: SEM images of (a) a device with a 50 nm overlay mismatch and (b) to (d) typical successfully overlaid nano-oscillator devices.

example of the overlay precision achievable with the JEOL JBX-6300FS electron beam, lithography system discussed in section 3.1.1. Another measure of the effectiveness of the fabrication process was the confirmation of Ohmic contacts between the Copper and Permalloy features. Contact resistances of the same order of magnitude and consistency, varying from approximately 50 Ω to 100 Ω, were measured similar to those measured for the LSV devices described in section 4.2.3.

4.5.1 Detection systems

SEM images of the nano-oscillators with detection systems are shown in figure 4.11. The addition of a Copper contact to the Permalloy disc allowed for the detection of the magnetisation of the disc by electrical measurement. The intention was to observe any change in electrical resistance due to anisotropic magneto-resistive measurements or by non-local LSV behaviour. This required extreme precision in the overlay accuracy of better than 50 nm. Although the overlay accuracy of the electron beam lithography system is quoted to be better than 9 nm, there is a greater inaccuracy in overlaying

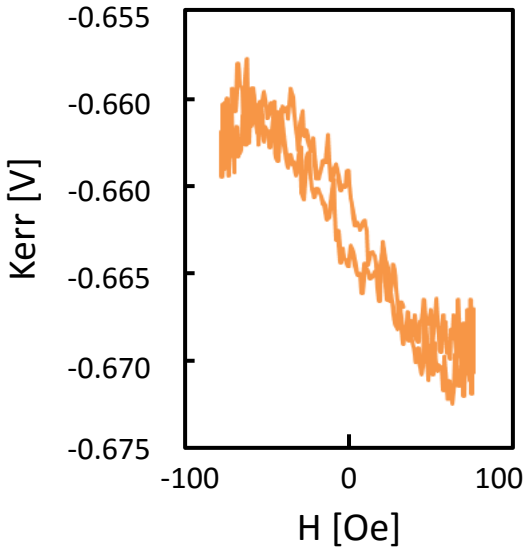

Figure 4.12: Polar MOKE signal from a Permalloy ellipsoid partially obscured by a Copper wire.

arrays of features. As can be seen in figure 4.11(a) the overlay of the Copper channels and the Permalloy disc was not successful in some cases.

For those devices that were successful, the resistances across the Permalloy disc/Copper channel interface, the Copper channel/Permalloy injector interface and the intermediate Copper channel were of the order 300 Ω. The increase in these interface resistances compared to typical values for LSV devices is due to the decreased contact area: In the lateral spin-valve devices the contact areas were 100 nm, 200 nm or 500 nm square, whereas in the nano-oscillator devices the contact area between the Copper channel and the partly overlaid disc were approximately 1×10^{-5} m^2, a factor four smaller than the interfacial area for the 200 nm wide bars measured with the data shown in table 4.1

The SEM images shown in figure 4.11 show that there is debris at the edges and on the surface of the devices, especially in figure 4.11(d). This is consistent with the debris that has been generated from the Copper layer on other devices and is difficult to avoid. It is specific to the lift-off process for the Copper layer and has not been seen on the Permalloy nano-features that have been fabricated.

The orientation of the magnetisation of the disc is an important aspect of device operation. For the optimum stray field from the disc an in plane magnetisation was necessary. To probe the magnetisation of the disc directly a focussed polar magneto-optical Kerr effect (MOKE) magnetometer was used, courtesy of Prof. D. Allwood at the University of Sheffield. The Kerr signal from the partially obscured Permalloy disc is shown in figure 4.12. The sloped transition of the hysteresis loop and the lack of

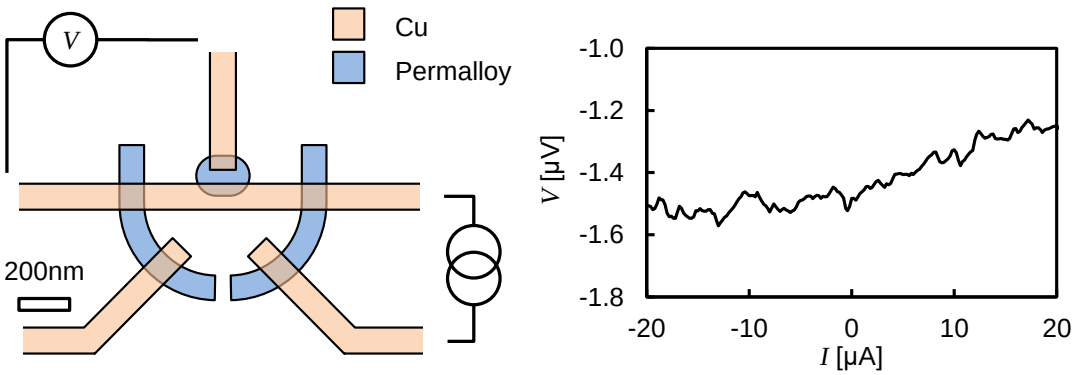

(a) (b)

Figure 4.13: (a) Schematic of the non-local measurement setup for the nano-oscillator and (b) preliminary result from a nano-oscillator device.

appreciable coercivity is typical of a vortex magnetic structure rather than an in plane structure [105, 106].

In an attempt to observe switching of the magnetisation of the Permalloy disc a measurement similar to that undertaken by Kimura *et al.* [79] was made. A pulsed current was applied to one of the injecting half horse-shoe shaped electrodes. The voltage across the Permalloy disc was measured non-locally as shown in figure 4.13(a) as the magnitude of the injected current was varied. The resultant non-local I-V curve did not show any changes in the non-local resistance due to magnetisation switching before the device was damaged by the large current densities supplied. The maximum current density supplied was an order of magnitude lower than the critical current density for switching observed by Kimura *et al.* [79]. The non-local resistance was (6.8$\pm$0.1) mΩ, which is of the expected order of magnitude when compared to similar devices, albeit with a different geometry. No magnetisation switching was observed, but a non-local spin-current in the Copper channel was observed over the Permalloy disc.

4.6 Device limitations

As a rule of thumb the DC density limit in Copper can be taken to be 5 MA/cm^2 [107]. The current limit therefore scales as the square of the typical device dimensions and hence the devices were susceptible to damage. The origin of this is through Joule heating,

$$\text{Heating} \propto \rho j^2 \,, \tag{4.5}$$

where ρ is the resistivity and j is the current density through the material [108]. Therefore in measuring a sample a sensible current limit should be set to avoid exceeding the

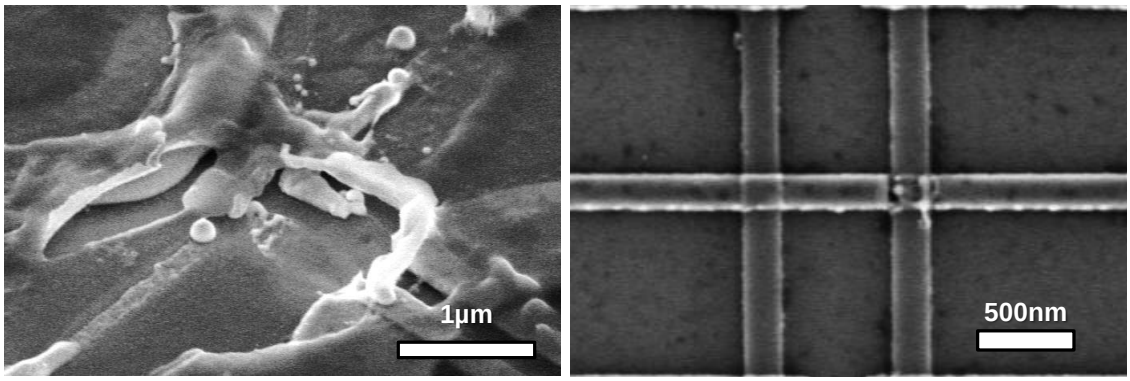

(a) (b)

Figure 4.14: SEM images of damaged ring-type devices with (a) 100 nm wide wires and (b) 200 nm wide wires and no ring.

5 MA/cm^2 limit. In this study a limit of 0.5 MA/cm^2 was imposed as it has been shown that the resistivity of the materials, in particular the interfaces, varied by up to two orders of magnitude in extreme cases. As this current limit was observed and the resistivity of the Copper and Permalloy nanowires did not vary significantly it was the interfacial resistance that caused damage to the samples. An example of the damage can be seen in figure 4.14(a). Here, the sample was observed in an SEM with the protective LOR3A resist layer still over the sample. As an insulator LOR3A renders the sample (almost) invisible under the SEM. As can be seen there was significant heating to the devices, causing what appears to be melting of the sample features and deformation/removal of the LOR3A layer. Furthermore, residual resist at the interface could increase the chances of damage due to Joule heating. Any residue would reduce the conductive area of the interface and so increase the magnitude of heating due to the applied current. The interface was therefore cleaned using an Ar ion milling process before depositing the Copper onto the Permalloy and the measurement technique employed millisecond pulses of current to reduce the effects of Joule heating at the interface.

Throughout this study the noise level in non-local resistance measurements varied, with the error varying by two orders of magnitude from 0.001 to 0.1 mΩ. The noise level bore no relationship with the initial non-local resistance, the change in the non-local resistance or the interfacial resistance. If there were a correlation between the interfacial resistance and the noise level this could indicate that the interface was responsible. However, it is also possible that magnetic impurities at the interface would act as spin-flip scattering sites but not manifest as a higher non-polarised electrical resistance. The higher noise levels, of the order 0.1 mΩ, could also be due to variations in the Copper channel resistivity. Variations in the measurement of the Copper channel between samples described in section 4.1 would indicate that this could be a contributing factor to the noise through the Nyquist effect, where the noise level is proportional to the

resistance [90].

Assuming a sample was fabricated with reasonable interfacial and Copper channel electrical characteristics, the questions "how reproducible are the measurements?" and "how resilient are the devices to electrical measurement?" needed to be answered. To test this, a repeat measurement was taken of a lateral spin-valve device with a straight Copper channel. Nine typical, complete non-local field sweep measurements were made before the sample was damaged. The change in the non-local resistance did not vary within error, remaining at an average of (0.57 ± 0.02) mΩ. The error over nine measurements was (0.024 ± 0.002) mΩ, where the error quoted was the standard error. Inspection of the device by SEM, shown in figure 4.14(b), shows that the damage caused was due to the Copper and Permalloy wires heating and fusing. This would cause mixing of the magnetic and non-magnetic material, nulling spin-injection into the Copper channel. Assuming this was a gradual process, this indicates that the dominant cause of the variation in noise was due to variation in Copper channel resistivity. The alloying or fusing of the material does not occur uniformly across the interface of the device. Therefore the current path through the interface itself is not uniform. The current passes through the corners and edges of the interface. This supports the explanation of the disparity between the observed non-local signal and its dependence on the injection area, discussed in the context of other variables in section 4.2.4. Further evidence of non-uniform electron transport was the peeling-off of the Copper wire from the Permalloy, discussed in ref. [103]. Here, in a separate investigation, a set of LSV devices the Copper channel peeled away from the interface with the Permalloy as a result of spin-transport measurements supporting the explanation for the debris observed on the samples discussed in section 4.3. As the injection current does not pass uniformly through the injection area, the non-local signal is not strictly proportional to the area, although does show some dependence. To investigate this further, modelling of the current through an interface of this nature in three dimensions would be required.

In summary, various sets of devices were fabricated around the principle of an LSV structure. In some cases the fabrication process did not produce as clearly defined features as would have been desirable, most notably with the "diamond" devices. Yet it was clear that a spin current was present at the point of operation, be it in the centre of an operational geometry or in proximity to a magnetised body within the spin channel. The measurement system that was designed has been optimised to a sufficient level for the observation of sub-micron scale spin transport phenomena.

Chapter 5

Diffusive spin transport phenomena

In this chapter results from the nanoscale investigation of spin transport phenomena are presented. The results focus on the applicability of microscopic spin transport phenomena in LSV-like spintronic devices. Firstly, LSV devices with a straight wire were investigated to provide a foundation for the exploration of diffusive spin currents. Secondly, the origin of the amplification in asymmetric spin channels observed by Abdullah *et al.* was investigated by altering the geometry to a symmetric case. Thirdly, the effect of a split channel – a ring structure – on the magnetic field operation of an all-metal magnetic gate operated LSV was investigated. The results presented here demonstrate methods to increase the operation efficiency of all-metal LSV devices.

5.1 Lateral spin-valves

Lateral spin-valves (LSVs) were fabricated, consisting of two Permalloy wires with an intermediate Copper spin channel, as discussed in section 4.2. The Permalloy bars were used as selective injector and detector layers as in a conventional perpendicular spin valve structure. The specifics of the fabrication of LSVs are outlined in section 3.1. This work focusses on the manipulation of spin within a nanowire channel. The process of spin injection and the efficiency of doing so is not the focus of this work. However, it was important to investigate the diffusion of electron spin within a channel to ascertain the typical dimensions that would be appropriate for specific geometries. The simplest structure, and one that has been investigated extensively [16, 47–49, 55, 58, 98, 109], is the conventional LSV structure. Being of a versatile, simple geometry it lends itself to the investigation of spintronic phenomena.

5.1.1 Switching characteristics

The fabrication process was largely successful, with a more detailed discussion held in in section 4.2.3. It was shown that it was possible to produce 100 nm scale features with a roughness of 3%. The electrical characterisation of the devices was undertaken by a pulsed electrical non-local measurement, discussed in section 3.4. With the sweeping of an applied field the ferromagnetic injector and detector wires in the LSV switch, creating the characteristic non-local signals shown in figure 5.1. Some of the raw data contained a thermal drift. This was removed by fitting a straight line to the data and subtracting the background drift. The separation, $L_{\mathrm{F-F}}$, between the Permalloy wires shown in figure 4.2 was varied. Unless otherwise stated the dimensions are the nominal widths/separations of the wires. A clear signal is obtained for the LSV with 100 nm separation as shown in figure 5.1 (black line), and a decrease in the change in resistance with Copper channel length is clear. The signal for the sample with a channel length of 500 nm (pink line) only shows part of the field sweep. The sample was destroyed part-way through testing, potentially through a transient voltage through a common earth with another piece of equipment or simply as a result of the current density supplied through the device. However, a drop in the non-local resistance at the switching field was still observed and so the change in R_{NL} was still extracted.

The coercivity and switching behaviour of the Permalloy wires is determined by their shape. The introduction of pointed ends to one of the Permalloy bars was intended to create a difference in the switching filed for the two wires. Introducing pointed ends has been shown to increase the switching field in magnetic nanowires [96] as compared to the flat ends there is a decreased transverse demagnetising field component in the

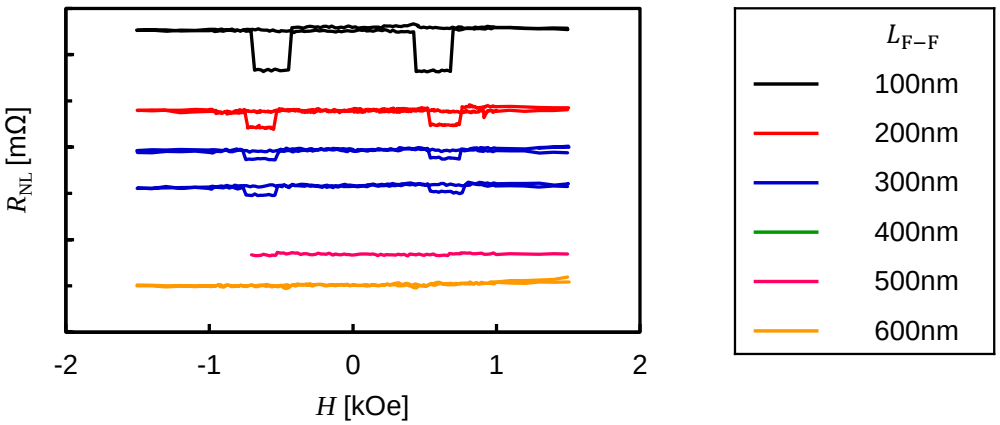

Figure 5.1: Non-local signals as a function of channel length, $L_{\mathrm{F-F}}$, for devices of nominal width 200 nm The signals have been shifted in the ordinate for ease of comparison and the minor gradation interval is 0.5 mΩ.

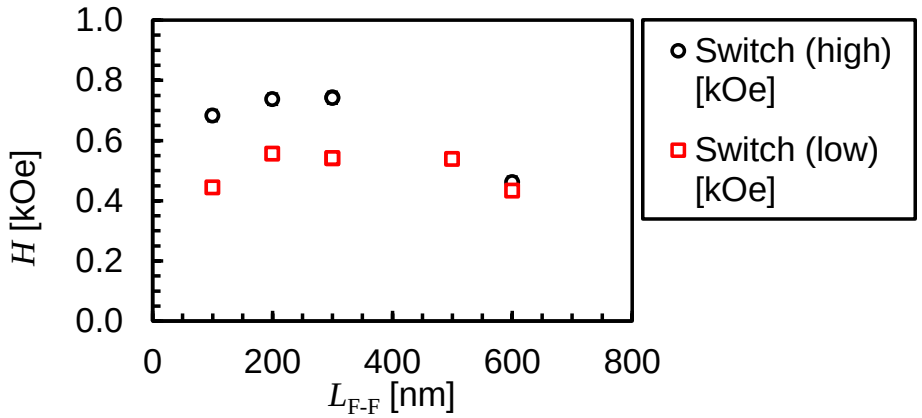

Figure 5.2: High and low switching fields for the Permalloy wires in the lateral spin-valves.

pointed nanowires. The transverse component of the demagnetising field causes magnetic canting at the edges, increasing the probability of a reverse field nucleating. After a reverse domain has been nucleated a rippled domain structure is formed along the length of a ferromagnetic bar before becoming entirely reversed. The presence of corners has been shown to suppress the formation of these rippled domain patterns, and so the reversal occurs over a narrower field range for the bars with pointed ends than those with flat ends as modelled by Schrefl and Fidler and observed experimentally by Kirk and Chapman [96].

The high and low switching fields were extracted from the non-local measurements, attributed to the pointed and non-pointed wires respectively. In the LSV of smallest separation, $L_{\mathrm{F-F}} = 100$ nm, there is a clear reduction in the average switching field of the ferromagnetic pair by 13% as shown in figure 5.2 due to the interaction between the two wires. Above 200 nm there is no obvious separation dependence upon the average switching field. It is then above 500 nm that a drop in the average switching field may be observed. At 600 nm the separation of the switching fields collapsed. Although difficult to make out due to the minute change in signal, the difference between the switching fields for the sample with a channel width of 600 nm were significantly reduced to a switching field width of approximately 200 Oe. One bar switched at a field of (440$\pm$10) Oe and the second at (460$\pm$10) Oe. It is clear that beyond this separation the preference for anti-parallel alignment is overcome by the magnitude of the applied field. Further investigation of this separation switching dependence would require fabrication of arrays of interacting pairs of Permalloy wires, or lateral-spin valves with separations ranging from 200 nm down to 50 nm or less.

Any differences between switching fields for samples of the same geometry is a result of two factors. It is possible that there is an error in aligning the sample with the magnetic field direction. This error is estimated to be up to 10 degrees. Intuitively, one

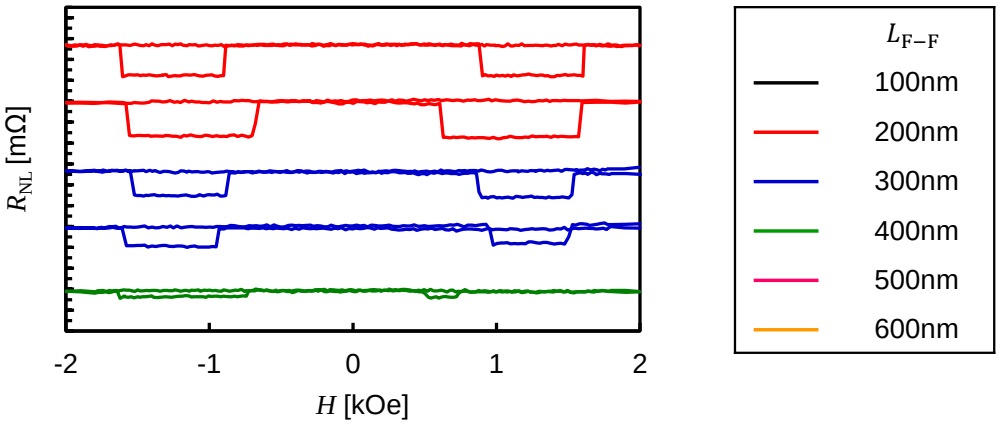

Figure 5.3: Non-local signals as a function of channel length, L_{F-F}, for devices with nominal wire width of 100 nm The signals have been shifted in the ordinate for ease of comparison and the minor gradation interval is 0.5 mΩ.

would expect such an error to reduce the coercivity, as it does in the Stoner-Wohlfarth model for fine particles, by 30%. However, variation in the switching field with wire alignment has been shown not to affect the switching field significantly and has been shown to be linear in the region between -15° and +15° applied field angle. The second, more likely explanation is that the effect is due to inconsistencies in the sample shape from differences in the lift-off conditions, a difference in switching fields is induced. The introduction of asperities at the edges and corners of the samples will affect the local demagnetising field, increasing or decreasing the nucleation field that initiates the reversal.

As for the smaller bars, a measurement of such a range of channel lengths was not possible due to sample damage during the fabrication/handling of the devices. However, the data for bars of 100 nm wire width are shown in figure 5.3. Again, the minor gradations on the non-local resistance axis are of 0.5 mΩ. The switching fields as a function of injector and detector separation are the same within the error in field and any differences are due to sample fabrication issues. This is in agreement with the data for the 200 nm wide bars, where no significant change in the mean switching field is observed between the channel lengths of 200 nm and 500 nm. The change in non-local resistance is clearly significantly larger than that for the 200 nm wide samples. The injection current density through the interfaces has been kept the same at 0.25 MA/cm^2. However, the current density through the Permalloy wire doubles, increasing from 0.83 to 1.67 MA/cm^2. The cross sectional area in the Copper channel is also halved, doubling the induced current density for a given spin chemical potential.

The majority of the contribution to the difference in non-local signals is due to heating effects. These will come from the Permalloy and Copper injector circuitry. The

$L_{\mathrm{F-F}}$ (nm)	ΔR_{NL} (mΩ)		$\Delta R_{\mathrm{NL100}}/\Delta R_{\mathrm{NL200}}$
	$w_{\mathrm{Py/Cu}}$ =100 nm	$w_{\mathrm{Py/Cu}}$ =200 nm	
100	-	0.453 ±0.003	-
200	1.45±0.01	0.18±0.01	8.1±0.3
	1.67±0.01	-	-
300	1.17±0.01	0.129±0.002	9.0±0.2
	0.84±0.01	0.090±0.002	9.3±0.2
400	0.27±0.01	-	-
500	-	0.010±0.003	-
600	-	0.033±0.004	-

Table 5.1: The value of ΔR_{NL} for samples of differing channel length and width.

increase in temperature due to Joule heating follows the relationship

$$\Delta T \propto I^2 R \tag{5.1}$$

where I is the charge current and R is the resistance. Therefore, at the injection side of the lateral spin valve the difference in the change in the temperature between the 200 nm and 100 nm in the vicinity of the Copper and Permalloy wires doubles due to the change in the cross-sectional area of the Copper and Permalloy. In the region of the interface between the Copper and the Permalloy, the cross-sectional area, and therefore change in temperature, quadruples due to the change in wire width from 200 nm to 100 nm. It is these thermal effects that dominate the spin injection efficiency, as an electron spin injected into a hot electron bath does so with a reduced efficiency [100]. This is the origin of the reduction in magnitude in change in R_{NL} by a factor of nine with wire width, summarised in table 5.1.

5.1.2 Spin diffusion length

The prime figure of interest is the spin diffusion length, λ_{S}, of the Copper channel. For the successful manipulation of a spin current there needs to be one present at the location of manipulation. To measure this, the channel length, $L_{\mathrm{F-F}}$, was varied from 100 to 600 nm and the corresponding change in non-local resistance, R_{NL}, measured. By using the equation discussed in section 2.3.2, reproduced below,

$$\Delta R_{\mathrm{NL}} = \frac{4P_{\mathrm{i}}^2 R_{\mathrm{F}}^2}{(1-P_{\mathrm{i}}^2)R_{\mathrm{N}}} \frac{\exp(-L_{\mathrm{F-F}}/\lambda_{\mathrm{S}})}{[1+\frac{2R_{\mathrm{F}}}{(1-P_{\mathrm{i}}^2)R_{\mathrm{N}}}]^2 - \exp(-2L_{\mathrm{F-F}}/\lambda_{\mathrm{S}})}\,, \tag{2.33}$$

the spin diffusion length within the Copper can be measured. Here, P_{i} is the spin polarisation efficiency in the Copper channel above the interface with the Permalloy, $R_{\mathrm{F(N)}}$ is the spin resistance of the ferromagnetic (non-magnetic) wire, $L_{\mathrm{F-F}}$ is the

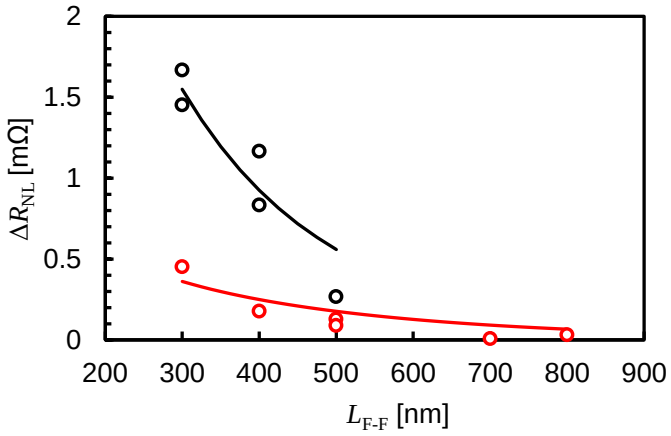

Figure 5.4: Dependence of the change in non-local resistance as a function of injector and detector separation for LSVs with Copper/Permalloy width 100 nm (black) and 200 nm (red).

spacing between the ferromagnetic injector and detector wires and λ_{S} is the spin diffusion length in the Copper channel. The spin resistance, reproduced below for continuity, takes the form

$$R_{(\mathrm{F/N})} = \frac{\rho_{(\mathrm{F/N})}\lambda_{\mathrm{S(F/N)}}}{a_{(\mathrm{F/N})}} \tag{2.34}$$

where ρ is the resistivity, λ_{S} is the spin diffusion length and a is the cross-sectional area of the ferromagnetic/non-magnetic wires. As stated in section 2.3.2 the spin resistance is the effective resistance between spin channels of the same material. Typical values of the spin resistance for devices in this study are $R_{\mathrm{N(Cu)}} \approx 4\ \Omega$ and $R_{\mathrm{F(Py)}} = 48.8\ \mathrm{m}\Omega$ for the wires with width 100 nm and thickness of 70 nm and 30 nm for Copper and Permalloy respectively.

In fitting this equation to the data, the spin diffusion length in Permalloy was taken to be 5.5 nm [110, 111] so that P_{i} and $\lambda_{\mathrm{S(Cu)}}$ could be used and extracted as free fitting parameters.

Most of the samples were tested to destruction, so only the nominal dimensions are available for discussion. From analysis of other sets of samples, the Copper width is typically 10% less and the Permalloy 10% more than the nominal width. In extracting the spin-diffusion length and the injection efficiency from the line of best fit, the distance between the ferromagnetic wires was taken from the centre of the injection and detection interface, *i.e. not* the separation between the edges of the wires. These figures were used in fitting a decay curve to the data. Figure 5.4 shows the data for the change in ΔR with nominal channel length and the curve fitted to the data.

The spin diffusion-lengths extracted from the lines of best fit were (200±25) nm and (310±30) nm for the two channel widths. A table of the extracted values and others

Material	T (K)	λ_{S} (nm)
Copper	4.2	1000±200 [48]
	4.2	395±30 [98]
	4.5	460±21 [109]
Copper (99.99%)	10	545±12 [58]
Copper (99.9999%)	10	771±13 [58]
Copper (99.99%)	270	365±60 [58]
Copper (99.9999%)	270	355±9 [58]
Copper	288	546 [47]
	290	290 [109]
	RT	500 [49]
	RT	350 [16]
	RT	400 [112]
	RT	350±50 [55]
Copper (99.9999%)	RT	200±25 (this work, $w_{\mathrm{Cu}} = 100$ nm)
	RT	310±30 (this work, $w_{\mathrm{Cu}} = 200$ nm)

Table 5.2: Summary of the spin diffusion lengths of polycrystalline Copper in this study and relevant literature.

found in the relevant literature are shown in table 5.2. These values correspond to spin resistance values of 2.37 and 3.72 Ω. It was expected that the spin diffusion lengths would be in agreement with each other. Such a reduction in the spin diffusion length from the 200 nm to the 100 nm wide wires was unexpected. The drop in spin diffusion length may be explained by the increase in surface dependent scattering as the spin diffusion length is greater than the dimensions of the medium within which it travels. This effect would be amplified by edge roughness. However, in the other works in table 5.2 the spin diffusion lengths do not display any significant wire dimension dependence. Therefore, it is more likely that the drop in spin diffusion length by a factor of two was due to an insufficient number of data points for a fit of significance. The r.m.s. error in the fit was 1.3×10^{-5} mΩ and 7.8×10^{-5} mΩ for values of $w_{\mathrm{Py/Cu}} = 200$ and 100 nm bars. The fit is six times better for the 200 nm than the 100 nm wide bars. The extracted values for the polarisation of the Permalloy were 0.20 and 0.33, compared to the well known value of 0.7 [56]. The model assumes that there is no spin flipping at the interface. The model also assumes that the electrons are not injected into a hot electron sink with a reduced polarisation. This is unlikely to be the case. This indicates that there is a significant spin-flipping at the interface between the Copper and the Permalloy. This will be due to magnetic impurities and Joule heating. The magnetic impurities could be due to roughness at the Copper/Permalloy interface or residue from the development stage of lithography. This is in agreement with the conclusion drawn from the presence of high and non-consistent interfacial resistances discussed in section 4.2. The spin diffusion length of (310±30) nm allows for the placement of a channel geometry to augment or alter the spin signal well within the limits of fabrication by electron beam lithography.

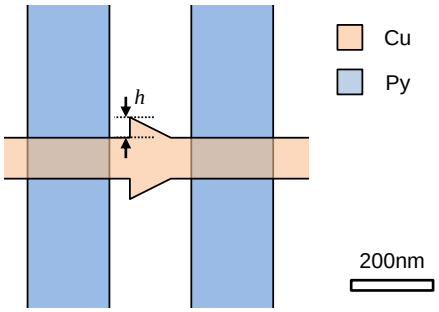

Figure 5.5: Schematic diagram of the arrow-type filtering device.

5.2 Spin amplification by filtering in lateral spin-valves

Amplification of a spin current signal by spin filtering was observed by Abdullah *et al.* [60] in LSVs with an asymmetric arrow feature within the spin channel. A schematic of the devices is shown in figure 5.5. The amplification observed was explained to be a result of geometrical spin filtering. Two diffusion currents are present in such a system. If the injection leads are attached to the left of the structure in figure 5.5, in an arrangement such that the spin majority is spin up, the following occurs: a spin-up current diffuses from the left to the right and a spin-down current diffuses from right to left. In this manner the charge current is compensated, *i.e.* there is no net flow of charge, yet there is a flow of spin. In the work by Abdullah *et al.* the compensating diffusion current saw a different resistance in transit along the channel due to the medial arrow geometry.

Considering the spin diffusion as a two current model, this leads to a preferential lower resistance for one spin channel compared to the other, leading to an effective amplification of the signal. To confirm this theory, LSVs with a symmetric geometry within the spin channel were fabricated. In line with the phenomenological theory for the amplification observed by Abdullah *et al.*, the difference in resistance for the spin up and spin down channels would be nil in a symmetrical spin channel. A diamond-like geometry was introduced into the spin channel as this geometry was similar to the arrow shapes used in the study, but symmetrical.

Non-local resistance measurements were made as a function of applied magnetic field. A typical non-local signal is shown in figure 5.6. The Permalloy injector and detector wires were fabricated in the same manner as for the LSV devices. They were designed to be 30 nm thick with a nominal width of 200 nm, one having pointed ends to separate the switching fields of the wires and so, ignoring the feature within Copper channel, the devices were the same as the LSV structures. The switching fields of the wires were (0.71$\pm$0.01) and (0.53$\pm$0.01) kOe. The separation between the edge of the wires was 200 nm (400 nm from the centre to centre), which for the LSV had a

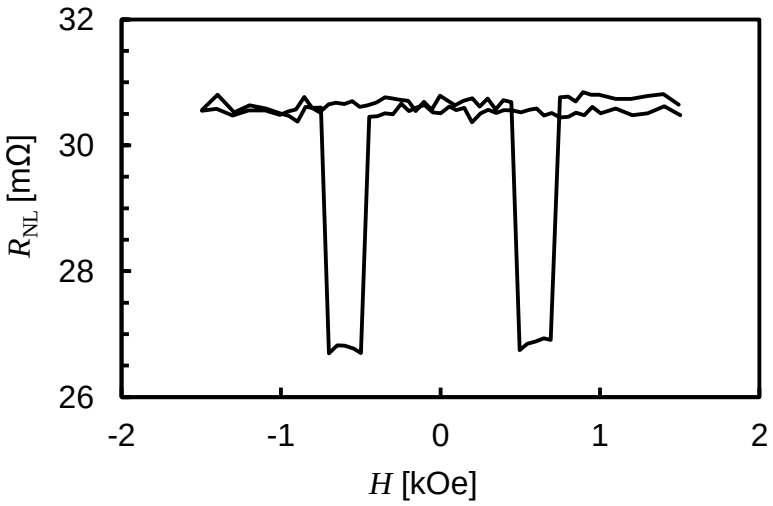

Figure 5.6: Non-local resistance as a function of the applied field for a diamond device of 28 nm height.

switching field of (0.74±0.01) and (0.56±0.01) kOe. The slight variation between the LSV and diamond LSV switching fields is likely to be due to differences arising from the lithography stages.

The non-local resistance as a function of applied field is shown for a variety of devices in figure 5.7. There was no correlation between the non-local resistance at the maximum field, *i.e.* in the parallel injector/detector alignment, and the channel geometry within this sample set. A greater variation is observed in this set of samples than in any other discussed so far. For the parallel injector/detector state the non-local resistance varies from 17 to 40 mΩ with an average non-local resistance of 28 mΩ. The ranges, averages and standard deviations of the non-local resistances for LSV devices is shown in table 5.3. This could be due to non-uniformity in the resistance across

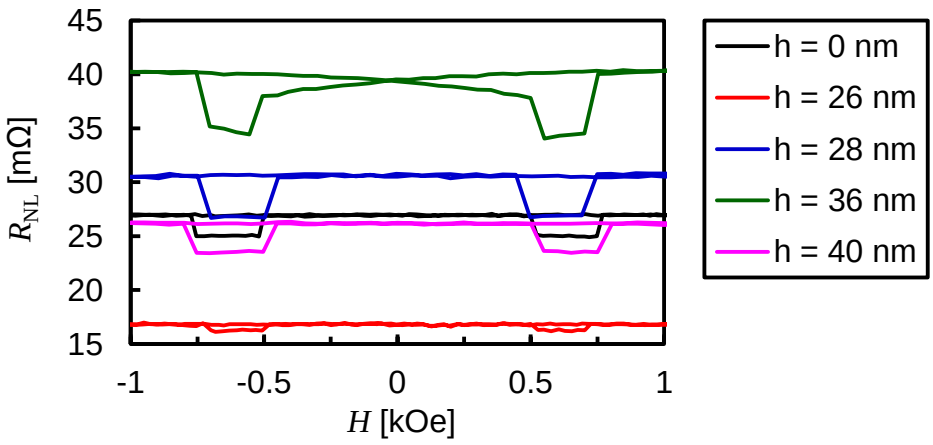

Figure 5.7: Raw data for the non-local resistance as a function of applied field for diamond lateral spin-valves of differing height.

Device	Mean R_{NL} (mΩ)	R_{NL} range (mΩ)	R_{NL} std. dev. (mΩ)
LSV, $w_{\mathrm{Py/Cu}} =$ 100 nm	29	10	4.1
LSV, $w_{\mathrm{Py/Cu}} =$ 200 nm	20	16	5.5
Diamond LSV	29	24	9.3

Table 5.3: Mean, range and standard deviations of the non-local resistance values for the devices investigated.

the interfaces, within the intermediate spin-channel or both. However, these variances in initial non-local resistance have not shown any correlation with the channel length or the change in non-local resistance in the straight Copper wire devices, discussed in section 5.1.2. It is possible, therefore, that the variation is due to interfacial impurities and imperfections. These could be due to: incomplete removal of the resist layer before Copper deposition; magnetic impurities (canting, misaligned grains or stoichiometric variance) at the interface between the Permalloy and Copper; or the presence of voids at the interface due to poor adhesion between the metals as discussed in ref. [103]. Across all of the devices measured there were variations in the initial non-local resistances, summarised in table 5.3, so it would seem that variations in the quality of the interface do contribute to this. Indeed, the figures in table 5.3 show that there is an increase from 4.1 to 5.5 mΩ in standard deviation of the non-local resistances with channel width. This is attributed to the increased variation in the injection efficiency due to an increased interfacial area.

However, there is a second possible explanation for variance in the non-local resistance at the maximum field. The standard deviation takes a significant leap from 5.5 mΩ to 9.3 mΩ between the bar devices with $w_{\mathrm{Py/Cu}} = 200$ nm and the diamond devices. The diamond devices had a Permalloy wire width of 200 nm, and a Copper wire width of 100 nm. So the increase in variation cannot be attributed to an increase in interfacial area. A great variation in the maximum non-local resistance was also observed by Abdullah *et al.* in the arrow devices that were investigated [60]. Here the initial non-local resistance varied from approximately 30 to 70 mΩ. As a variation of this magnitude has only been observed in devices with a intermediate geometry of some kind, and no significant other dependence has been observed across all of the devices measured in this study, it seems that the change in initial non-local resistance is dominated by variations in Copper channel resistance, which was of course intended in the spin filtering amplification devices.

In the non-local measurements, shown in figure 5.7, one of the Permalloy bars for the 36 nm diamond device clearly reverses in a different manner to the others. The transition

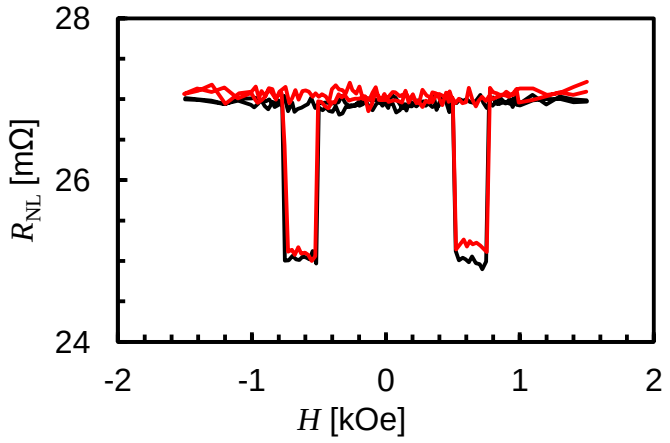

Figure 5.8: Field dependence of the non-local resistance for injection from the left (black) and right (red) Permalloy wire.

is sloped, occurring over approximately 1 kOe, rather than being immediate. This type of reversal was observed in one other sample of the same Permalloy width (200 nm). The sloped transition is likely due to a metastable domain structure within the nanowire. According to Schrefl *et al.* [96], an intermediate ladder-like domain structure was present in their 200 nm wide Permalloy wires. The presence of pointed ends suppressed this metastable state. The pointed wires investigated by Schrefl *et al.* had higher switching field of 225 Oe, which falls in line with our finding that the sloped reversal only occurs in the wire with the lower switching field. The presence of a complex domain structure along the length of the Permalloy wire and at the interface of the Copper would reduce the magnitude of the detected non-local resistance by reducing the injection polarisation by scattering through regions of varying magnetisation within the Permalloy injector or detector wire.

To investigate the effect of channel geometry the height of the diamond geometry was varied and the non-local resistance characteristics were measured. For a complete investigation of the phenomenological explanation for the effect put forward by Abdullah *et al.* it was necessary to take a measurement and then reverse the injector and detectors. First, a measurement was taken with the left (right) Permalloy bar being used as the injector (detector). Then the leads from the measurement equipment were removed and switched so that the right (left) Permalloy bar was used as the injector (detector). The field dependence of the non-local signal from a measurement of this nature is shown in figure 5.8. As can be seen, there is a negligible change in ΔR_{NL} of ${\Delta R_{\mathrm{NL}}}^{\mathrm{LtoR}}/{\Delta R_{\mathrm{NL}}}^{\mathrm{RtoL}} = (1.06\pm0.04)$. Over the sample set, three measurements with the reversed injector/detector direction were taken. They were (1.06±0.04), (1.0±0.2) and (1.29±0.03) for the diamond devices of height $h = 0$, 26 and 36 nm. There was no correlation between the ratio of injector/detector interfacial area and any observed

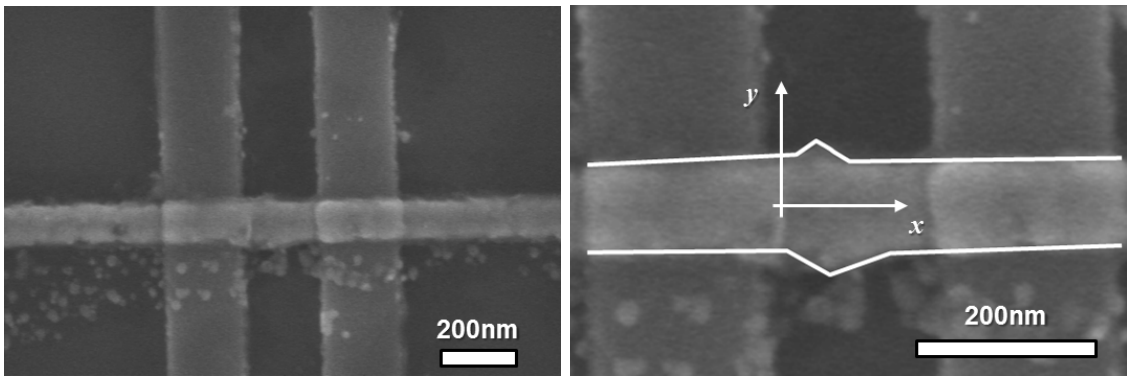

(a) (b)

Figure 5.9: (a) SEM micrograph of a diamond device with nominal height 20 nm and (b) a close-up with an outline of the diamond geometry.

amplification.

There was, however, asymmetry in the devices that were fabricated. An example device is shown in figure 5.9. Here, there is a clear offset between the peaks of the diamond shape within the channel. This is not paramount to the symmetry of the diffusion channel. It is change in channel cross-section that is of importance, *i.e.* the difference in the differential of the cross section, $\frac{\partial y}{\partial x}$, between travelling from left to right and right to left. For the three devices where the reverse electrical measurement could be taken, a measure of this asymmetry was made. The increase in width versus height to the centre of the diamond and the subsequent decrease in height to the edge was taken for electrons travelling from left to right in figure 5.9(b) and then from right to left. This was done separately for the top and bottom sections of the diamond. These differentials in the widths were summed as a measure of the asymmetry. This can be taken as an estimate of the channel asymmetry. There is a monotonic increase in the amplification and indeed the magnitude of ΔR_{NL} with the channel asymmetry, proving the origin of the spin filtering amplification is geometrical.

It can be stated as a certainty that the geometry of the channel has an effect upon the change in non-local resistance. The clear amplification of the signal observed by Abdullah *et al.* [60] by a factor of seven is shown alongside the results for the symmetrical diamond devices. An amplification of the order measured in the arrow devices was not observed, as shown in figure 5.10. There is an increase in ΔR_{NL} as the diamond height, h, increases. This can, however, be explained by the asymmetry in the diamond devices, mentioned above. In accordance with the theory, any lateral asymmetry in the channel geometry will result in an increase in the non-local spin signal.

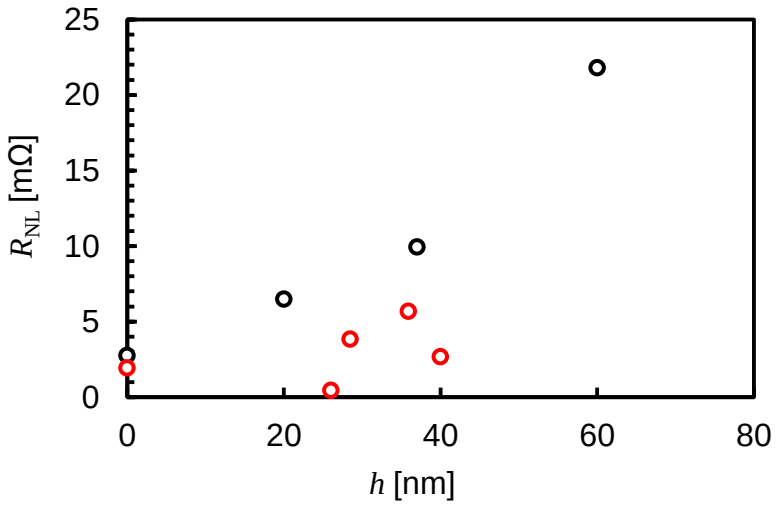

Figure 5.10: Height dependence of the change in non-local signal for arrow (black circles) and diamond (red circles) devices.

5.3 Spin Interference

Spin interference devices were fabricated in the same manner as described in section 4.2.3 and for all other devices investigated. The devices were fabricated around a LSV design with 200 nm wire width, $w_{\mathrm{Py/Cu}}$. This was above the smallest feature sizes that were achievable, indeed a SEM image based around a LSV device with 100 nm wire width is shown in figure 4.9(b). Operation of the devices required the application of a significant current, of the order of tens of milliampere, to the current-carrying wire. This would require the application of a large potential difference, hundreds of millivolts, to the device. Larger feature sizes were preferred for fear of damaging the devices due to static discharge. An SEM micrograph of a typical device is shown in figure 5.11.

The interfacial resistances of the devices were of the order of hundreds of Ohms, which is at the upper end of the ranges of interfacial resistances observed for similar devices in this study (typically between 20 and 100 Ω), indicating that the quality of the interface between the Permalloy and the Coppper was not as uniform or clean as in other devices. The current-carrying bar, above the non-local spin channel, was intended to generate an Oersted field, in the manner outlined in section 2.5.2. This wire was 1 µm wide and 70 nm thick and had a resistance of the order of 100 Ω.

To estimate crudely the field applied from the current-carrying bar it was initially assumed to be an infinitely long wire and to obey Ampère's law. However, for a more accurate estimation of the field from the wire, finite element modelling was used to estimate the field at the centre of the ring and the variation across the ring on the nanometric scale. The current carrying bar was modelled as an axisymmetric Copper

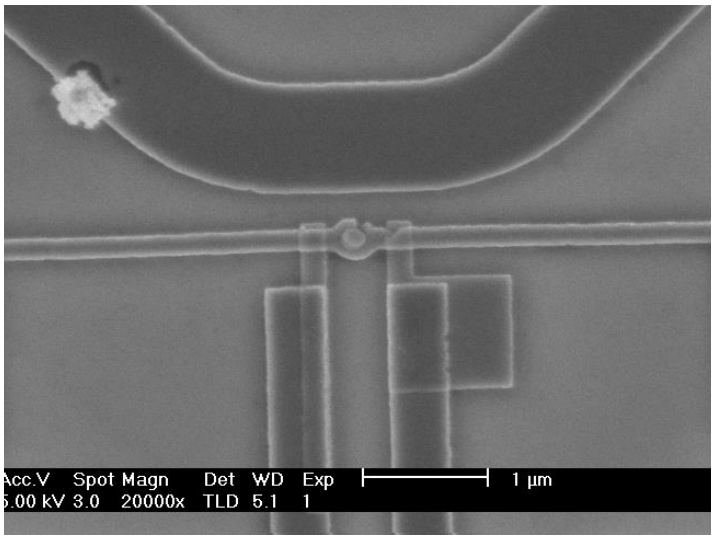

Figure 5.11: SEM image of a typical ring device.

ring with a mesh size of 0.05 µm outside the ring and 0.1 µm inside the ring. The outer diameter of the ring was taken to be 7.33 µm to fit closely the curvature of the bar patterned in the interference device. As expected, the field at the centre of the spin interference ring (the ring patterened into the Copper channel of the LSV) is linear with the current passing through the current-carrying bar.

The key to the operation of the spin-interference device is the variation of the field across the two channels of the ring. A plot of the magnitude as a function of distance across the ring is shown in figure 5.12. The vertical lines in the plot show the position of the outer edge of the ring structure. As can be seen, there is a clear variation in the magnetic field strength across the ring. The magnitude of the Ampère field at any given point is proportional to the current passing through the current-carrying bar, and so the difference in the field across the ring varies linearly with the current applied. Due to

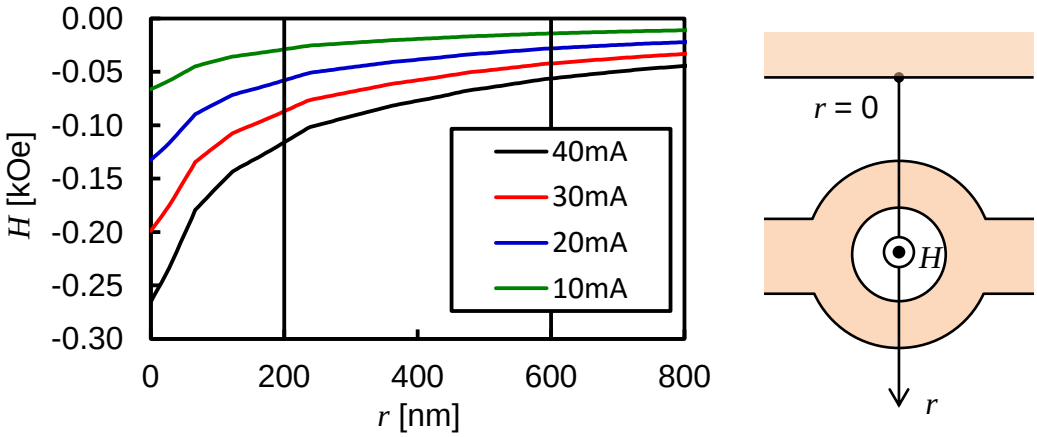

Figure 5.12: Variance of the Ampère field across the ring.

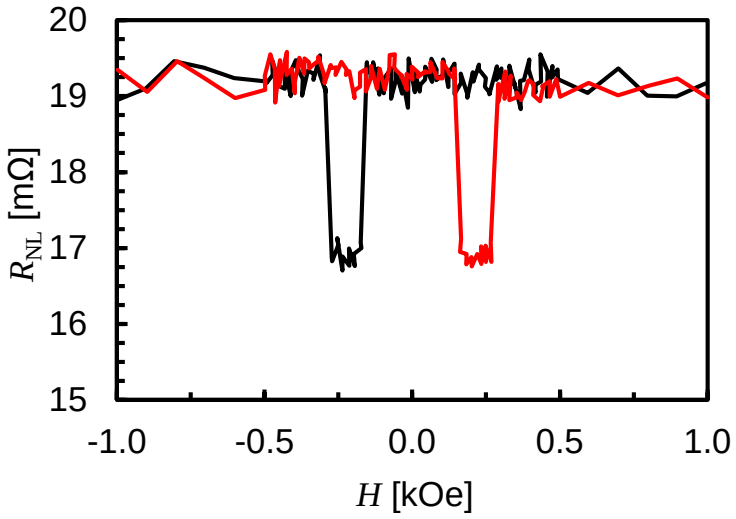

Figure 5.13: Typical non-local signal from a ring device as a function of applied in-plane field with field sweep from positive to negative (black line) and negative to positive (red line).

the curvature of the current-carrying wire there is also a change in the field along the direction parallel to the electron-spin diffusion. However, this is an order of magnitude smaller than the variance perpendicular, along the section shown in figure 5.12.

A typical non-local measurement is shown for a ring device in figure 5.13. The device measured had no medial ring and showed a change in non-local resistance between the parallel and anti-parallel magnetic configuration of (2.33±0.03) mΩ. This is an order of magnitude higher than the corresponding value for a straight bar device, as discussed in section 4.2.4. It should be noted, however, that these are not comparable quantities. The two sets of samples were fabricated at different times and the interfacial qualities are different, as indicated by the difference in the interfacial resistances which were twice to an order of magnitude higher, *c.f.* between 20 and 100 Ω to 100s Ω. The increase in resistance could be due to several things, for example the formation of an oxide layer at the Permalloy/Copper interface or residue from the previous resist layer. Given the increase in the spin-signal and the corresponding increase in the change in non-local resistance in the literature due to the introduction of tunnel barriers at the interface the former is taken to be the case.

There was, again, variation in the non-local signal in the parallel injector/detector magnetic configuration, from (10.9±0.2) mΩ to (19.25±0.02) mΩ. The variation in the injection and detection efficiency is thought to be related to the interfacial resistance. However, throughout the study no correlation was observed. The coercivity of the injector and detector wires was observed to be at (0.17±0.01) kOe and (0.27±0.01) kOe for the low and high switching field respectively, lower than that for the straight bars in

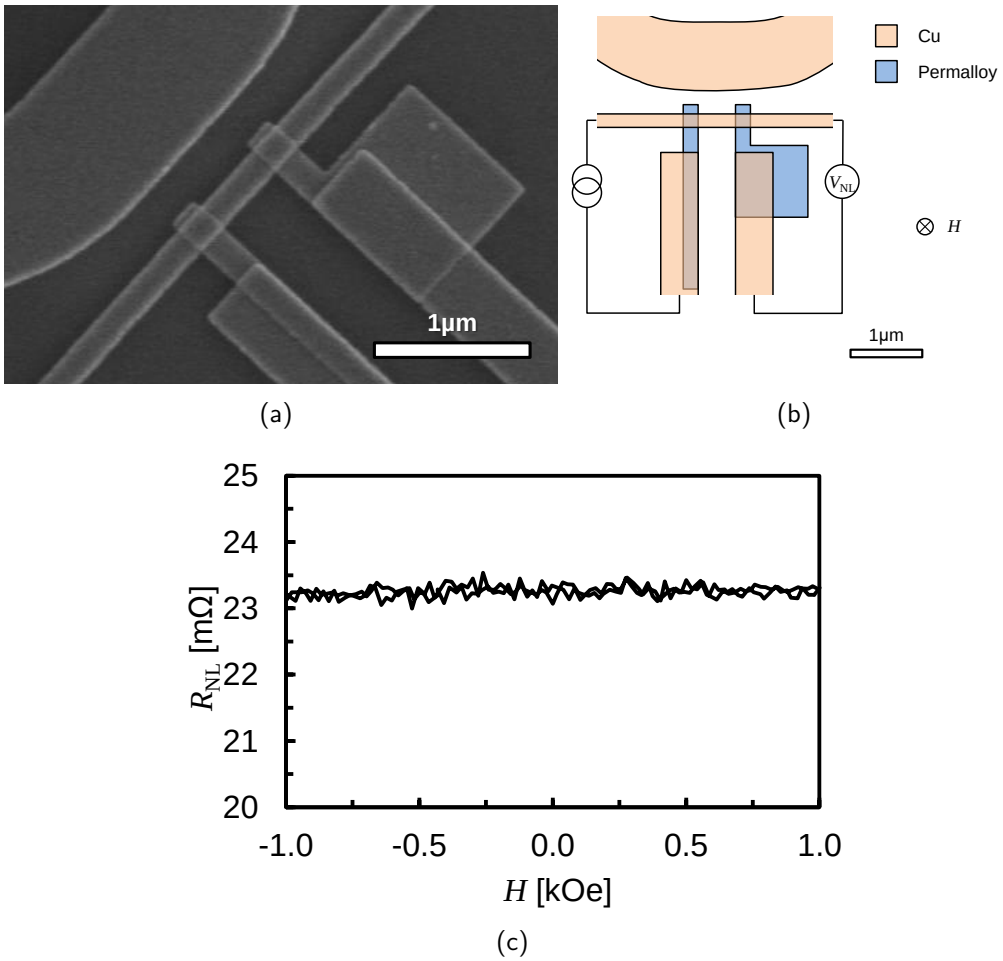

Figure 5.14: (a) SEM micrograph of a "ringless" ring device, (b) schematic of the measurement setup and (c) the non-local resistance as a function of applied field.

figure 5.2 by more than a factor of two. This was due to change in design of the injector bars. One was patterned to have a large square pad attached, an example of which is shown in figure 5.14(a), and considerably shorter length. The introduction of a square pad to the end of one of the wires, *i.e.* more corners, lowered the switching field due to the increase in potential reverse domain nucleation points. The reduction in this length from 6 µm to 1.5 µm reduced the induced stability in the anti-parallel configuration due to flux closure.

To verify that any observed effects were due to the introduction of a ring into the spin-channel, devices were fabricated with a straight spin diffusion channel; a "ringless" device. All other features were kept the same. An SEM micrograph of such a device is shown in figure 5.14(a). A conventional Hanle measurement [47] was undertaken. The injector/detector bars were set in a parallel magnetic configuration by applying a saturating in-plane magnetic field of 2 kOe. The sample was then repositioned so that it was still centrally located within the pole pieces as to apply an out-of-plane magnetic field. The in-plane component of the magnetic field was assumed to be negligible. The

non-local resistance measurement was set up as shown in figure 5.14(b). The out-of-plane field was swept to add an additional field to those generating the electron-spin precession in the spin-channel, which should cause the electron spin imbalance to collapse and reduce the magnitude of the spin imbalance at the detector wire. No Hanle effect was observed up to a field of 2 kOe. A plot with a smaller field step between 1 kOe and -1 kOe is shown in figure 5.14(c). This is not surprising, given that the Hanle effect is usually only observable in metal lateral spin-valves at fields well above 2 kOe [47].

After proving that there was no Hanle effect upon the spin imbalance in the Copper channel, a measurement was then made to observe the change in ΔR_{NL}. A conventional non-local measurement was made to confirm the presence of non-local behaviour. The medial ring had an outer diameter of (365±5) nm with an inner diameter of (193±5) nm. There was a slight difference between the width of the upper and lower portions of the ring, being (93±5) nm and (83±5) nm respectively. The parallel injector/detector non-local resistance was (12.04±0.03) mΩ and the change in non-local resistance was (1.2±0.2) mΩ. Satisfied that the ring device showed the requisite non-local spin transport, the effect of the introduction of a field gradient across the medial ring was measured. The magnetisation of the injector and detector pair was set to be anti-parallel by saturating the bars in a 2 kOe field and reducing the field to (0.56±0.01) kOe. This supporting field remained applied to the device to ensure that the magnetisation remained in the anti-parallel state. Then, a DC current was applied to the current-carrying bar. The non-local resistance was measured with a pulsed injection current of 25 μA as a function of the DC current applied to the ring. The DC current was converted into an estimate for the applied field at the centre of the ring by finite element modelling, as described above. To confirm that any change in the non-local voltage was not subject to thermal effects, the same measurement was taken in the absence of any applied current. There was no change in the non-local resistance as a function of applied current. There is a clear reduction from the initial ΔR_{NL} of (1.2±0.2) mΩ to (0.0±0.2) mΩ at 0.078 kOe. This significant reduction, coupled with the absence of any dephasing at fields of up to 2 kOe in devices without a ring structure shows that spin-transport properties are significantly affected by the presence of a ring and application of a field gradient.

The non-local resistance in the presence of a field in the z-direction, as given in section 2.5.1 and reproduced below for continuity, is given by the following:

$$R_{\mathrm{NL}}(B_{\perp}) = \pm\frac{\alpha_1\alpha_2 D\rho_{\mathrm{N}}}{a_{\mathrm{N}}}\int_0^{\infty}\Phi(t)\cos(\omega_{\mathrm{L}}t)\exp\left(-\frac{Dt}{{\lambda_{\mathrm{S}}}^2}\right)\mathrm{d}t \tag{2.47}$$

where

$$\Phi(t) = \frac{1}{\sqrt{4\pi Dt}}\exp\left(-\frac{L_{\mathrm{F-F}}^2}{4Dt}\right). \tag{2.48}$$

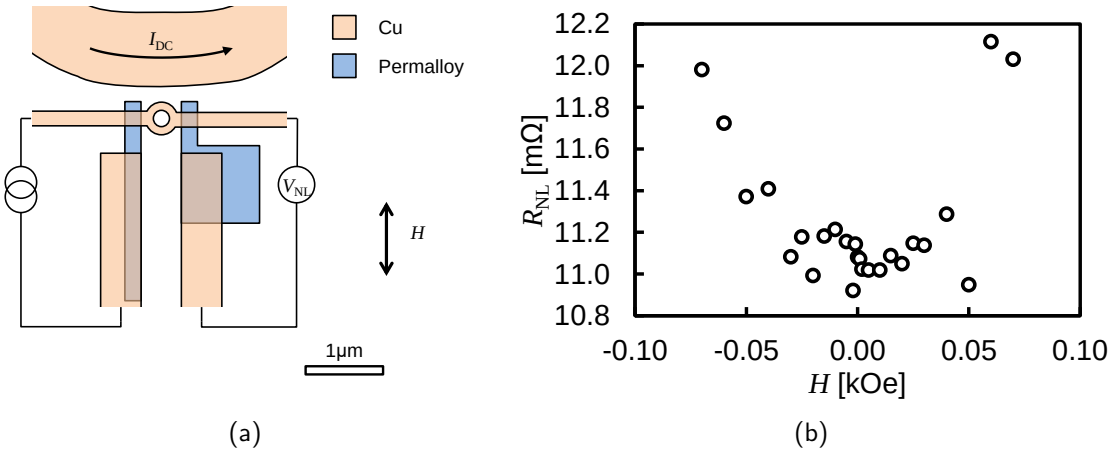

(a) (b)

Figure 5.15: (a) Schematic diagram of a ring device and (b) the change in the non-local signal with fields induced by the current-carrying wire.

The solution to which was solved analytically by Sasaki *et al.* [69] and is given by

$$\begin{aligned} R_{\mathrm{NL}}(B_{\perp}) = & \frac{\alpha^2 \rho_{\mathrm{N}} \sqrt{D\tau}}{2a_{\mathrm{N}}} \exp\left(-\frac{L_{\mathrm{F-F}}}{\sqrt{D\tau}}\right) (1+{\omega_{\mathrm{L}}}^2\tau^2)^{-1/4} \\ & \times \exp\left\{-\frac{L_{\mathrm{F-F}}}{\sqrt{D\tau}}\left[\sqrt{\frac{1}{2}(\sqrt{1+{\omega_{\mathrm{L}}}^2\tau^2}+1)}-1\right]\right\} \\ & \times \cos\left[\frac{\arctan(\omega_{\mathrm{L}}\tau)}{2}+\frac{L_{\mathrm{F-F}}}{\sqrt{D\tau}}\sqrt{\frac{1}{2}(\sqrt{1+{\omega_{\mathrm{L}}}^2\tau^2}-1)}\right] \end{aligned} \quad . \qquad (2.49)$$

where α is the spin polarisation of the injector/detector, D is the diffusion constant, ρ_{N} is the resistivity, a_{N} is the cross-sectional area of the Copper wire, ω_{L} is the Larmor frequency, t is time, λ_{S} is the spin diffusion length in the Copper wire, $L_{\mathrm{F-F}}$ is the distance between the ferromagnetic injector and detector, and τ is the spin averaged relaxation time.

Although equation (2.49) does not contain any consideration of the field gradient across the ring, it can be used to calculate any change in the operational efficiency of the ring device due to the presence of the ring and the field gradient. By carrying out a Hanle measurement with the perpendicular field being generated by the current carrying bar, the "effective" spin diffusion length can be measured and compared to the spin diffusion length observed in conventional lateral spin-valves.

Equation (2.49) was fitted to the data shown in figure 5.15(b). The diffusion constant for Copper, D, was taken to be 2.7×10^{-3} $\mathrm{m^2s^{-1}}$ [55] and the resistivity was taken to be 2.66 μΩ·cm. The injector/detector polarisations and the spin diffusion length in the ring devices were left as free fitting parameters. Equation (2.49) was fitted to the data by a least-squares fit. The red line in figure 5.16 is the least-squares fit using

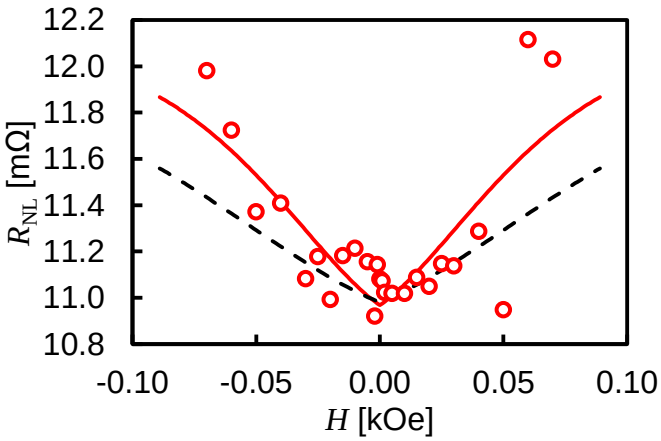

D	2.1×10^{-3} m^2s^{-1} [55]
$L_{F\text{-}F}$	650 nm
σ_{Cu}	3.76×10^{7} Ωm^{-1}
α	3.6%

Figure 5.16: Change in non-local resistance as a function of applied fields in the z-direction. The red line shows the least-squares fit of equation (2.49) to the data and the black line shows the same fit using the parameters from nominally identical devices without a medial ring structure. The parameters that were used in fitting the lines are shown in the table to the right of the graph.

equation (2.49), where the injector/detector polarisations were found to be 3.6% and the spin diffusion length was found to be (410±60) nm. The black dashed line in figure 5.16 was calculated using a spin diffusion length of (310±30) nm, as found in the straight wire devices of the same nominal dimensions. The difference between the lines was due to the change in spin-diffusion length alone, as the same fitting parameters were used to highlight the improvement in operational efficiency.

The change in spin diffusion length by 30% in a high purity Copper (99.9999%) channel by the introduction of a medial ring displays the potential for an additional functionality in an LSV. With the application of gate magnetic-field to the LSV device an additional degree of freedom is available. Furthermore, splitting the diffusion channel into two paths by the introduction of a ring produces an increase in the spin diffusion length. This change in the spin diffusion length enhances the efficiency of the gate operation. Compared to a conventional LSV the ring LSV is 30% more efficient.

In summary, LSV devices were fabricated and the spin diffusion characteristics were analysed. The spin diffusion lengths and injection efficiencies fell in line with values recorded elsewhere [16,47–49,55,58,109,112]. To confirm the origin of the spin filtering amplification discovered by Abdullah *et al.* in LSVs with an asymmetric spin diffusion channel, devices were fabricated with a symmetric feature within the channel. No spin filtering was observed. This proves that the amplification due to filtering observed was due to a direction dependent diffusion resistance. Ring devices were fabricated, where the Copper diffusion channel split and recombined. By the application of different magnetic fields to each diffusion path, an increase in the gate operation efficiency of 30% was observed. This demonstrates a possible new mechanism for the gate operation of all-

metal LSVs in a more efficient manner.

Part II

Macroscopic spin current phenomena

Chapter 6

Effects of mechanical rotation

The effects of coupling between angular momentum and spin are well known and are explained in the review of gyromagnetic effects upon electron-inertia by Barnett [113]. There are two well-known gyromagnetic effects: The Einstein-de Haas and the Barnett effects are essentially reciprocal in nature and describe the coupling between the rotational and magnetic angular momentum of electrons, nuclei and magnetised bodies. Further to this, through general relativistic principles of equivalence, rotation of a suitable sample at high speeds may present as an electric field to the electrons within the sample. This would result as spin Hall effect: the anomalous spin dependent scattering of electrons described in section 2.2.2.

6.1 The Barnett effect

The Barnett effect was first presented in Barnett's work of 1915 [17]. The effect is the enhancement of the magnetisation of a ferromagnetic material by the application of angular momentum by mechanical rotation. A brief qualitative explanation would be that the spin angular momentum of the magnetic domains within a magnetised body behave in the same way as the angular momentum/momenta of any other body or ensemble [113]. That is to say the magnetisations of the domains in a material tend to align with the vector for rotation, for the sake of argument along the z-axis. Barnett predicted that this would occur in electrically neutral bodies.

The original work by Barnett observed that the magnetisation of a material is augmented by the addition of the "Barnett field". This pseudo-field augments the magnetisation of a particles. For the case of an electron, this pseudo-field has a magnitude

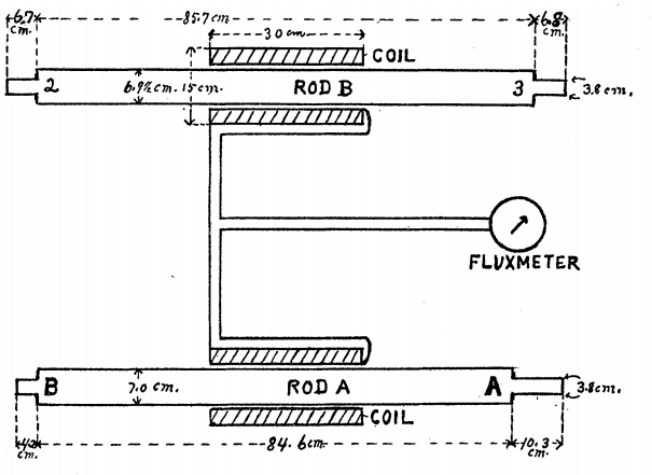

Figure 6.1: Schematic of the original experiment performed by Barnett [17].

given by

$$\mathbf{B}_\Omega = 2\frac{m_\mathrm{e}}{q_\mathrm{e}}\Omega \tag{6.1}$$

where m_e is the electron rest mass, Ω is the angular frequency and q_e is the electronic charge. In the experiment performed by Barnett [17], an iron rod of length 0.99 m and diameter 0.07 m was set with its axis horizontal as shown in figure 6.1. A coil was wound around the rod acting as a fluxmeter. A compensating rod was used with a second coil wound in opposition and connected in series with the first. In this manner any fluctuations in the global magnetic field would be compensated and the galvanometer attached to the fluxmeter circuit measured the induced voltage in the coil due to any variation in the flux threading the first rod due to rotation alone as shown in figure 6.1. The rod was driven by an electric motor and the deflection in the galvanometer was measured. This deflection was then calibrated to a field applied to the stationary rod. It was found that the intensity of the magnetisation produced by the rotation of the iron rod was -1.5×10^{-6} G/Hz, an intensity that was half of the predicted value. In fact his experimental result was out by a factor of $1/g$, as the work done by Barnett predates the prediction and experimental observation of the gyromagnetic ratio.

A more modern derivation that includes the full expression for the electron gyromagnetic ratio, $\gamma_\mathrm{e} = gq_\mathrm{e}/2m_\mathrm{e}$, involves the transformation of the Hamiltonian for an electron spin from an inertial frame to a rotating frame and is given by

$$\mathcal{H} = \frac{\mathbf{p}^2}{2m_\mathrm{e}} - (\mathbf{r} \times \mathbf{p}) \cdot \boldsymbol{\Omega} + \mathbf{S}_\mathrm{tot} \cdot \frac{gq_\mathrm{e}}{2m_\mathrm{e}}(\mathbf{B} + \mathbf{B}_\Omega) \tag{6.2}$$

where $\mathbf{p}$ is the momentum, m_e is the electron rest mass, $\boldsymbol{\Omega}$ is the angular frequency, $\mathbf{S}_\mathrm{tot}$ the total spin angular-momentum, g the Landé g-factor, q_e the electronic charge, m_e the electronic rest mass and $\mathbf{B}$ is the applied magnetic field. $\mathbf{B}_\Omega$ is the Barnett field

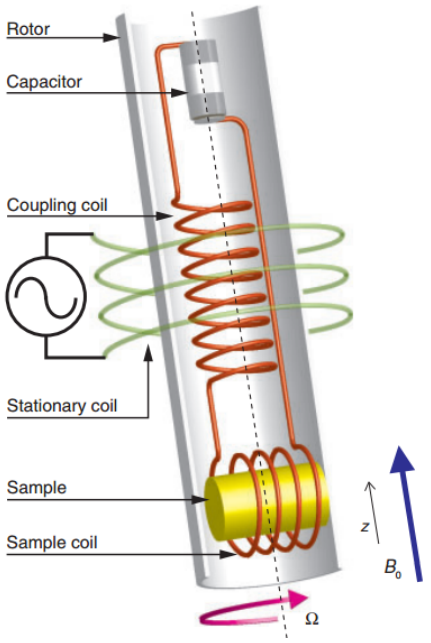

Figure 6.2: Schematic of the original experiment performed by Chudo *et al.*, reproduced from ref. [23].

and is given by:

$$\mathbf{B}_\Omega = \frac{2m_\mathrm{e}}{gq_\mathrm{e}}\mathbf{\Omega} \tag{6.3}$$

The concept of the Barnett field can be extended to different magnetised bodies. The description is not restricted to that for an electron spin as the Barnett field affects nuclear moments as well as the moments of atoms and magnetic domains.

Almost 100 years later Chudo *et al.* [23] published the use of a nuclear magnetic resonance (NMR) measurement technique to observe the Barnett effect on the nuclear moment of samples. The atomic nucleus has a significantly larger mass than an electron. Thus, the effect was increased significantly compared to that observed by Barnett [17] on the electronic moments as given by equation (6.3). The absorption of electromagnetic radiation by a nucleus is proportional to the local magnetic field. By sweeping the frequency of the radiation an absorption peak is observed. This peak shifts with a change in the moment of the nucleus. The experimental set-up developed by Chudo *et al.* is shown in figure 6.2.

Confirmation that the observed shift in the NMR resonance was due to the Barnett effect was made by using various materials and therefore nuclear g-factor. The samples used were Indium phosphate and Silicon powder samples where the isotopes measured were ^{115}In and ^{29}Si, having g-factors of opposing sign, *i.e.* the nuclear magnetic moment is anti-parallel to its angular momentum [23].

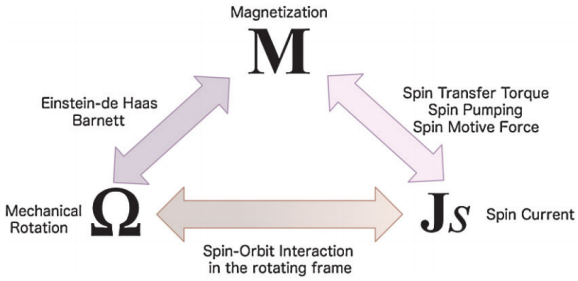

Figure 6.3: The relationship between magnetisation, mechanical rotation and spin current, reproduced from ref. [19].

6.2 Mechanical spin effects

The relationship between rotational motion and magnetisation is well established and discussed in section 6.1. Similarly, the coupling between magnetisation and spin current is well established as illustrated in figure 6.3. The final piece of the puzzle is the link between an electron spin and mechanical rotation. Mechanical spin effects are often termed spin mechatronics. This is an emerging field within spintronics with, as yet, no direct experimental confirmation. The first publications of the theory of spin mechatronics [18, 19] form the basis of the discussion in this section.

The phenomenon arises from Einstein's principle of equivalence for inertial and gravitational effects. The mathematical derivation of the general relativistic effect that causes this phenomenon is beyond the scope of this work but is summarised below to highlight the significant physical statements. For the full mathematical derivation see Matsuo *et al.* and the appendices therein [18]. Firstly, the covariant form of the Dirac equation was taken by Matsuo *et al.* and the appropriate coordinate transforms from an inertial frame to a rotating frame were made. The coordinate transformation is defined as,

$$d\mathbf{r}' = d\mathbf{r} + (\boldsymbol{\Omega} \times \mathbf{r})dt \tag{6.4}$$

where $\mathbf{r}$ is position and $\boldsymbol{\Omega}$ is the angular frequency, defined in figure 6.4. The Dirac equation was then substituted into the Schroedinger equation,

$$\mathrm{i}\hbar\frac{\partial\Psi}{\partial t} = \mathcal{H}\Psi \tag{6.5}$$

where

$$\mathcal{H} = \beta_1 m_\mathrm{e}c^2 + c\alpha_1 \cdot \boldsymbol{\pi} + q_\mathrm{e}A_0 - \boldsymbol{\Omega} \cdot (\mathbf{r} \times \boldsymbol{\pi} + \boldsymbol{\Sigma})\,. \tag{6.6}$$

Here the symbols have their conventional meanings and a full discussion of the equation is in ref. [18]. The term of significance is the $\boldsymbol{\Omega}\cdot(\mathbf{r}\times\boldsymbol{\pi}+\boldsymbol{\Sigma})$ term, where $\boldsymbol{\Omega}$ is the angular frequency, $\mathbf{r}$ is the position vector, $\boldsymbol{\pi}$ is the frame transformed mechanical momentum,

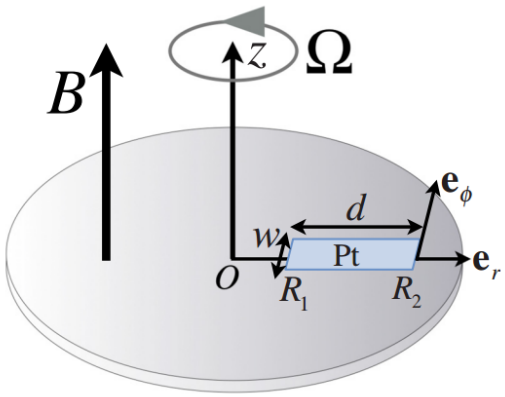

Figure 6.4: A foil in a rotating frame, from ref. [114].

and $\boldsymbol{\Sigma}$ is the spin operator. This is the quantum mechanical generalisation for the inertial effects. It is from this term that the effect arises. In a non-quantum mechanical system this term would describe the Coriolis, centrifugal and other rotationally induced forces. The Pauli-Schroedinger equation may then be solved yielding an extra electric field that acts upon an electron wave-packet in the presence of a magnetic field as shown in figure 6.4. The electric field takes the form:

$$\mathbf{E}' = \mathbf{E} + (\boldsymbol{\Omega} \times \mathbf{r}) \times \mathbf{B} \tag{6.7}$$

where $\mathbf{E}'$ is the field felt by the electron wave-packet in the rotating frame, $\mathbf{E}$ is any electric field in the inertial frame, $\boldsymbol{\Omega}$ is the angular frequency and $\mathbf{B}$ is the static magnetic field applied to the electron wave-packet in the rotating frame.

In a material with strong spin-orbit coupling, such as Tungsten, a set of semi-classical equations may be used to describe the spin dependent transport. The velocity of an electron is split into a base "normal" velocity, $\mathbf{v}$, and an additional anomalous Hall velocity, $\mathbf{v}_\sigma$. *I.e.* $\dot{\mathbf{r}} = \mathbf{v} + \mathbf{v}_\sigma$ where the Lorentz force acting upon an electron, given by

$$\mathbf{F} = q_\mathrm{e}[\mathbf{E} + (\mathbf{v} \times \mathbf{B})]\,, \tag{6.8}$$

which results from the local electric field, $\mathbf{E}$, velocity of the electron, $\mathbf{v}$, and the local magnetic field $\mathbf{B}$ to govern the motion of the particle. The Lorentz force defines the "normal" electron velocity in the material.

In a rotating frame the anomalous electric field is defined as

$$\mathbf{E}_\sigma = \mathbf{v}_\sigma \times \mathbf{B} = \frac{q_\mathrm{e}\lambda}{\hbar}\{\sigma \times [(\boldsymbol{\Omega} \times \mathbf{r}) \times \mathbf{B}]\} \times \mathbf{B} \tag{6.9}$$

where λ is the spin-orbit coupling and σ is the Paul spin matrix. The spin-orbit coupling,

λ is related to the spin-orbit coupling strength, η_{SO}, by

$$\lambda k_{\mathrm{F}}^2 = \eta_{\mathrm{SO}} \tag{6.10}$$

where k_{F} is the Fermi wave-vector. In the simple case where the angular frequency and a magnetic field are parallel and in the z-direction, *i.e.* $\mathbf{\Omega} = (0, 0, \Omega)$ and $\mathbf{B} = (0, 0, B)$, the spin induced spin-current in a rotating disc such as that shown in like figure 6.4 is the sum of the radial and azimuthal components [18].

$$\mathbf{j}_{\mathrm{S}}(r) = j_{\mathrm{S}}^{r}(r)\mathbf{e}_{\mathrm{r}} + j_{\mathrm{S}}^{\phi}(r)\mathbf{e}_{\phi} \tag{6.11}$$

where $\mathbf{j}_{\mathrm{S}}$ is the spin-current density, and $\mathbf{e}_{\mathrm{r}(\phi)}$ is the unit vector in the radial (azimuthal) direction. The radial and azimuthal spin-current components differ and are given by

$$j_{\mathrm{S}}^{r} = \frac{\tau_{\mathrm{S}}\omega_{\mathrm{C}}}{1 + (\tau_{\mathrm{S}}\omega_{\mathrm{C}})^2} j_{\mathrm{S}}^{0} \tag{6.12}$$

and

$$j_{\mathrm{S}}^{\phi} = \frac{(\tau_{\mathrm{S}}\omega_{\mathrm{C}})^2}{1 + (\tau_{\mathrm{S}}\omega_{\mathrm{C}})^2} j_{\mathrm{S}}^{0} \tag{6.13}$$

where $j_{\mathrm{S}}^{r(\phi)}$ is the spin current in the radial (azimuthal) direction, τ_{S} is the spin-relaxation time and ω_{C} is the cyclotron frequency. j_{S}^{0} is given by

$$j_{\mathrm{S}}^{0}(r) = 2nq_{\mathrm{e}}\eta_{\mathrm{SO}}\frac{\hbar\Omega\omega_{\mathrm{C}}r}{E_{\mathrm{F}}}\,. \tag{6.14}$$

Here n is the electron number density, q_{e} the electronic charge, η_{SO} the spin-orbit coupling strength, $\hbar$ the reduced Planck constant, Ω the angular frequency, ω_{C} the cyclotron frequency, r the radius from the centre of rotation and E_{F} is the Fermi energy for the electron wave-packet. For electrons, up-spins migrate in the positive $\mathbf{e}_{\mathrm{r}}$ and $\mathbf{e}_{\phi}$ directions, *i.e.* to the outer and leading edges of a rotating foil. By In the ballistic limit, where $\tau_{\mathrm{S}}\omega_{\mathrm{C}}$ is large, equation (6.12) goes to zero and equation (6.13) reduces to $j_{\mathrm{S}}^{\phi} = j_{\mathrm{S}}^{0}$. If the ballistic limit is not approached, $j_{\mathrm{S}}^{\mathrm{r}} \propto B^2$ and $j_{\mathrm{S}}^{\phi} \propto B^3$ [114].

The dimensionless spin-orbit coupling may be obtained by non-local measurement of the spin Hall effect [18] and η_{SO} is proportional to the spin Hall angle, θ_{SH} [27]. The values of η_{SO} and θ_{SH} for various transition metals are shown in table 6.1. With the exception of η_{SO} for Tungsten, all of the values were obtained experimentally. The value of η_{SO} for Tungsten was estimated based on the values of η_{SO} and θ_{SH} obtained for other materials and that $\eta_{\mathrm{SO}} \propto \theta_{\mathrm{SH}}$ [27]. The material suggested by Matsuo *et al.* was Platinum, with $\eta_{\mathrm{SO}} = 0.58$. However, θ_{SH} for Tungsten is significantly larger than for Platinum and so should yield a spin current in excess of an order of magnitude larger

Material	T (K)	η_{SO}	θ_{SH} (%)
Aluminium	4.2	0.006 [115]	0.02±0.01 [115]
Palladium	293	0.28 [116]	1.2±0.2 [117]
Platinum	293	0.58 [118]	2.7±0.3 [117]
Tantalum	10	0.17 [119]	-0.37±0.11 [119]
Tungsten	293	≈9	-33±6 [120]

Table 6.1: Table of spin-orbit coupling constants and spin Hall angles for various transition metals.

than Platinum. For this reason, Tungsten was the material of choice for this study.

In summary, of the great variety of ways to introduce a spin polarisation into a system the induction of a spin current by mechanical rotation is one of the more recent. Although the field of spintronics is developing, with new methods of generating a spin current still being discovered to date, the fundamentals of the physics should not be unfamiliar to those who are familiar with magnetism and electronics. And so, methods of generating a spin current generally have an analogue with an already well established electron charge or magnetic phenomena.

Chapter 7

Experimental methods

In this section the measurement technique for the observation of a spin current induced by mechanical rotation is outlined, in the manner predicted and in similar experimental conditions to those proposed by Matsuo *et al.* [18, 19]. The experimental setup consists of the generation of a spin current in a millimetric foil. An appropriate technique must be chosen carefully for the measurement of a nanoscale phenomenon on a macroscopic length scale whilst maintaining sensitivity to nanoscale phenomenon. Of those available, an optical technique was most suitable.

7.1 Optical set-up

A paramagnetic sample was rotated mechanically to generate a spin current. In a mechanically rotating system the electrical detection of such a phenomenon would be complicated. The presence of rotating parts in the circuit would require brushed contacts and the subsequent noise level would render the measurement imperceptible. An optical detection system has the advantage of being remote and, in principle at least, simple. For the measurement in mind a paramagnetic foil was mounted on a Neodynium-Iron-Boron (NdFeB) magnet and fixed at a radius to a rotating plate. Rotating the plate caused the foil to periodically pass under a probing laser. The reflected beam was analysed to observe any changes in the moment at the surface of the sample.

7.1.1 Principles of polar MOKE magnetometry

The measurement system that was used was a converted DC magneto-optical Kerr effect (MOKE) magnetometer. A MOKE magnetometer relies on the magneto-optical Kerr effect, discovered by Kerr in 1877. Kerr described the rotation of the plane polarisation of light as it reflected from the surface of a magnetised object [121]. The effect is fundamentally the same as all other magneto-optical effects where the plane of polarisation is affected by the application of an external field, such as the Voigt and Faraday effects. The geometry used was a conventional polar MOKE geometry, where the incident light is introduced perpendicularly at the surface that is magnetised parallel to the incoming light. The presence of a magnetic B-field alters the off-diagonal terms in the dielectric tensor, E_{D}, leading to an optical anisotropy in the material [122].

$$E_{\mathrm{D}} = N^2 \begin{pmatrix} 1 & \mathrm{i}Q & 0 \\ -\mathrm{i}Q & 1 & 0 \\ 0 & 0 & 1 \end{pmatrix} \tag{7.1}$$

where N is the refractive index of the material and Q is the magneto-optical constant of the material. Upon entering a magnetised material a linearly polarised beam will split into left and right circularly polarised components. The two components travel with different velocities and attenuation within the material, as defined by the refractive index for each polarisation.

$$N_{\mathrm{l/r}} = N(1 \pm \hat{g}Q) \tag{7.2}$$

where $\hat{g}$ is the direction cosine between the propagation vector of the light and the magnetisation. It should be noted that the dielectric tensor is altered by the magnetic flux density, B. However, in most materials the contribution from the magnetic field strength, H, is minuscule compared to the contribution from the local magnetisation, M. Therefore the interaction is dominated by M [123]. This is of particular importance when probing materials such as ferrimagnets, where there are sub-lattices that compensate to give a total flux density of zero or close to zero, yet still have a local magnetisation that affects the polarised light. Upon exiting the material the two circularly polarised components recombine to form an elliptically polarised beam with the major axis rotated away from the initial state by θ_{K}, the Kerr rotation [123].

The beam that is reflected from a magnetised surface therefore has two components. Firstly, the beam will consist of a non-magneto-optically dependent background component, A_{B}. Secondly, there is also a magneto-optically dependent component. This

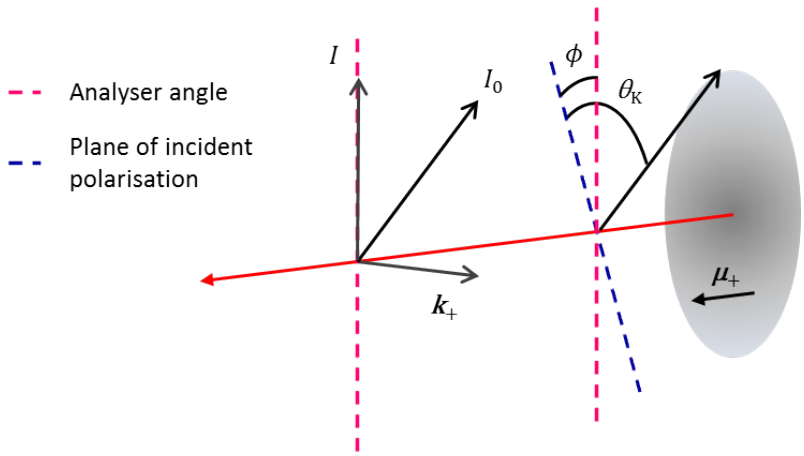

Figure 7.1: Reflected components of a normally incident, plane polarised beam from a magnetised surface.

is a magneto-optically dependent vector, $\mathbf{k}_{\pm}$, that has a sign and magnitude depending on the relative direction and intensity of the magnetic moment, $\mathbf{m}_{\pm}$. The resulting amplitude is given by A and is dependent upon $\mathbf{m}$. By placing an analysing polariser in the path of the reflected beam any changes in intensity/amplitude in the transmitted beam corresponds to a change in θ_{K} [124].

$$A = A_{\mathrm{B}} + A_0 \sin^2(\phi - \theta_{\mathrm{K}}) \tag{7.3}$$

The amplitude of the transmitted, magneto-optically dependent component is governed by the above equation where A_0 is the light intensity prior to the analyser and where ϕ and θ_{K} are defined in figure 7.1. The change in a moment, $\Delta\mathbf{m}$, is proportional to the change in signal and for small angles is defined by equation (7.4)

$$\Delta\mathbf{m} = A_{\mathrm{B}} + A_0 \sin^2(\phi - \Delta\theta_{\mathrm{K}}) \approx \Delta A \tag{7.4}$$

where $\mathbf{m}$ is the moment of the interaction volume, A_{B} is the non-magneto-optical background amplitude, A_0 is the amplitude at maximum analyser transmission, ϕ is the analyser angle and θ_{K} is the Kerr rotation.

7.1.2 Sources of error in MOKE

There are a series of intrinsic sources of noise and error in the MOKE measurement system as a whole. These fall loosely into electrical and optical categories. A short review by Allwood *et al.* contains some of the general errors that should be considered

in designing a MOKE system [124]. Electrical errors have already been discussed in section 3.4.1.

The first major optical artefact in the systems was due to the pulse width of the signal as the frequency of rotation increased. The photo-detectors used (Thorlabs DET36A) have a rise time of 1 ns. However, the current generated in the photodetector was the integral of the signal intensity over a time defined by the radial speed of the sample and its diameter. It therefore followed a $1/f$ relationship. At a radial distance of 0.1 m, a rotational frequency of 200 Hz and with a sample diameter of 1.5 mm the integration time was approximately 12 µs.

To be sure that the measurement was only due to the change in moment two analysers were used. These were set in opposition to each other at an angle $\phi^{\pm}$ so that a positive change in θ_{K} resulted in an increase in signal in one photo-detector and a decrease in the other, described respectively by equation (7.5). Therefore a frequency dependent amplitude, $A(f)$, term is added to equation (7.4) to give the voltage detected for the two channels,

$$\Delta V^{\pm} \approx \Delta \mathbf{m}^{\pm} + A(f) \propto \frac{\Delta A^{\pm}}{A_0^{\pm}} + A(f) \tag{7.5}$$

where $\Delta A^{+} = -\Delta A^{-}$. It should be noted that the $A_0^{\pm}$ term used was the intensity due to the signal amplitude at 50 Hz for the $\phi^{\pm}$ analyser channels. This varied by a small amount for the two photo-detector channels. By subtracting the signals from one another the frequency dependent response was removed. *i.e.*

$$\frac{\Delta V^{+} - \Delta V^{-}}{2} = \frac{\Delta A^{+} A_0^{-} - \Delta A^{-} A_0^{+}}{2 A_0^{-} A_0^{+}} \tag{7.6}$$

where $A_0^{-} \simeq A_0^{+}$,

$$\frac{\Delta V^{+} - \Delta V^{-}}{2} \propto \Delta \mathbf{m} \tag{7.7}$$

The remaining sources of error resulted from errors in alignment. The beam had a divergence of 1.8 mrad and the use of a lens focussing the beam onto the surface of the sample caused a variety of incident angles. This actively reduced the sensitivity and accuracy of the measurement by effectively smearing the Kerr interaction with the laser beam. This could have been avoided to some extent by using a lens with a longer focal length. For the ultimate sensitivity the path lengths were also reduced as much as possible and were the same for the two paths to the photo-detectors. The final major source of error in the optical measurement was in the reflection from the sample surface and the difference in reflectivity of the samples. The roughness of the sample surface

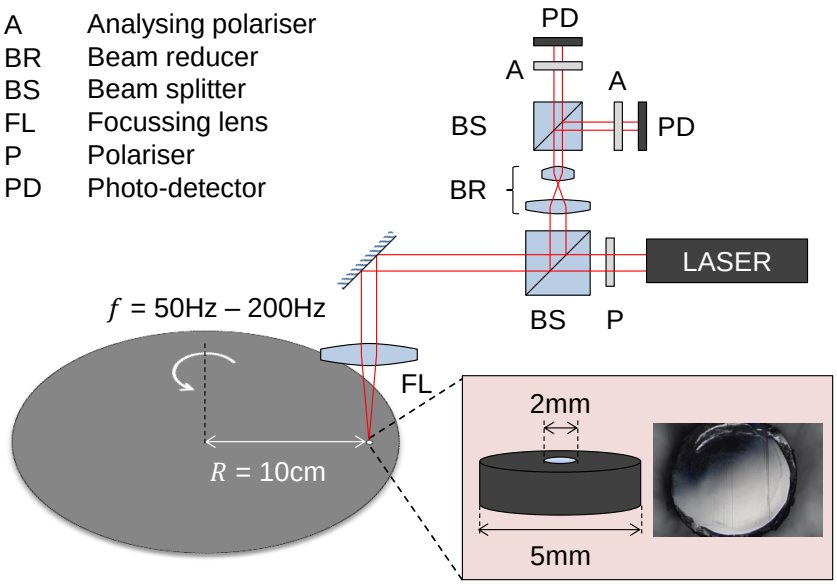

Figure 7.2: Schematic diagram of the optical system.

drastically affected the signal by scattering light upon reflection.

7.1.3 Optical components

A diagram of the optical system is shown in figure 7.2. A Melles-Griot 05-STP-903 Helium-Neon laser with a wavelength of 632.8 nm was used. The beam was Gaussian with a 1.8 mrad divergence. The laser was selected as the source for a direct current (DC), single frequency MOKE [125] for which the laser stability (0.1 %) was paramount.

In the experimental set-up the beam passed through a beam splitter and was focussed onto the surface of a foil as shown in figure 7.2. Due to space restrictions a lens with a focal length of 50 mm was used. The divergence of the beam due to focussing was estimated to cause a 0.01 % weakening of the signal due to the range of angles of incidence.

The $1/e^2$ full beam diameter, $2w$, was measured by a conventional 90/10 measurement. A razor blade was drawn across the path of the beam with a micrometer controlled stage. The intensity of the beam and the position of the blade were measured and plotted, as can be seen in figure 7.3. Given that the beam is Guassian the distance for the 90 % - 10 % drop in intensity, x_{90-10}, is related to the $1/e^2$ half width by equation

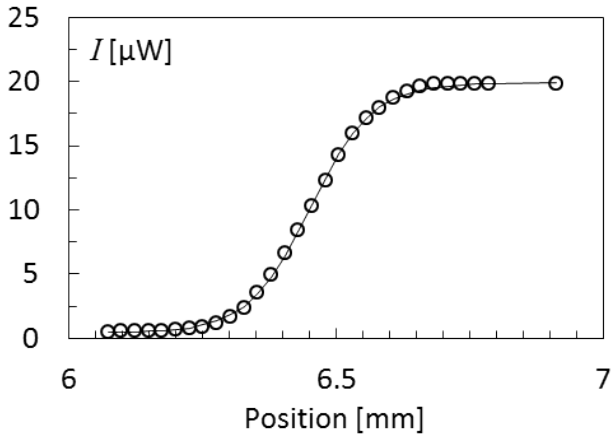

Figure 7.3: Measurement of the beam profile by the x_{90-10} method.

(7.8) and the beam full width was found to be (0.42±0.01) mm.

$$x_{90-10} = 1.28w \tag{7.8}$$

The beam was normally incident on the foil surface. The Tungsten foil was initially 125 μm thick. It was polished to a <1 μm r.m.s. smooth finish with a series of diamond lapping papers and an Alumina suspension with grains of 0.05 μm diameter. The foils were 1.5 mm in diameter and mounted on Nickel/Copper/Nickel flashed NdFeB magnets of varying field strength that were 5 mm in diameter. The magnets were sprayed black to avoid other reflections. In the experimental set-up shown in figure 7.2 the beam is shown reflecting from the surface of the foil. This was adjusted to be as normal as possible. It then passed back through the initial focussing lens to the beam splitter. The beam was then reflected and passed through a second splitter and the two analysers that were set in opposition as described in section 7.1.2. The beam intensity was then detected by two Thorlabs DET36a detectors.

7.2 Mechanical set-up

The mechanical set-up was designed as part of this work and several iterations of design were made before the final system was realised. The set-up was custom built and manufactured in-house. Efforts that were made to reduce the noise in the optical and electrical circuitry would have been pointless if the rotating system were mechanically unstable. The design of the system was defined by the by the experimental requirements. The impetus for the generation of a spin current by mechanical rotation is covered in section 6.2. It has been predicted that to generate a spin current density of 10^8 A/m^2

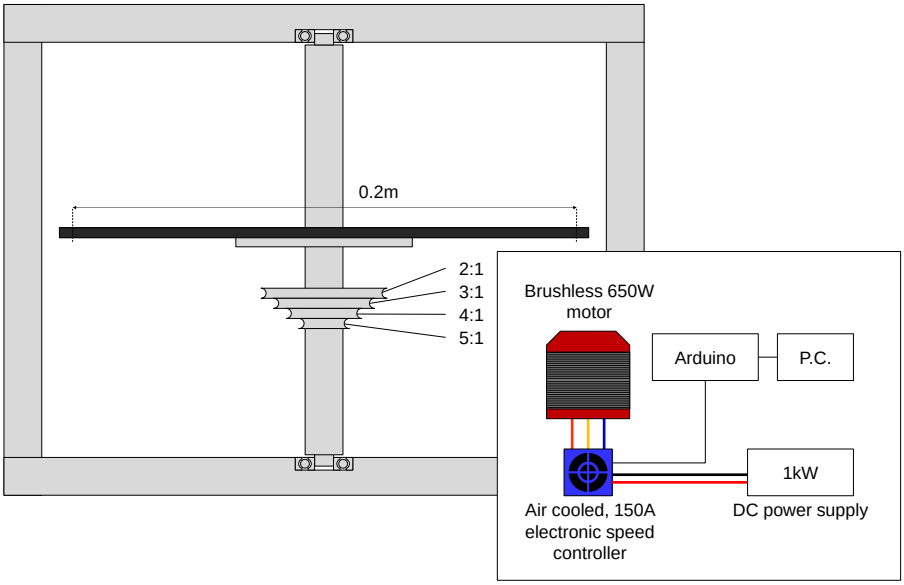

Figure 7.4: Simplified drawing of the rotating plate frame with, inset, a block diagram of the brushless motor control.

a Platinum sample must be rotating at a frequency of 1 kHz, at a radial distance of 0.1 m in a field of 10 kG [18]. A spin current of 15 times this value is expected due to the significantly larger spin Hall angle of (33±6)% compared to (2.7±0.3)% for Tungsten and Platinum respectively. In a rotating system such as this there is a trade-off between frequency, f, and radius, R. In this system there was an upper limit to the angular frequency that could be achieved due to imbalance in the plate and shaft. It was therefore not possible to reach the full extent of the experimental conditions outlined by Matsuo *et al.*

Various NdFeB magnets were used with fields up to $B = (5.2\pm0.1)$ kG. The magnet was 5 mm in diameter compared to the 1.5 mm diameter of the foil. The sample and magnet were glued together and fixed to the extremity (r=100 mm) of a 210 mm diameter, 4 mm thick stainless steel plate. To ensure that the plate was as finely balanced as possible a "blank" magnet was placed at the opposite position. Also, during the final stages of assembly the plate was attached to the shaft, as shown in figure 7.4 and finish machined so that the plate was flat. The disc mount was bolted to the anti-vibration optical bench. Any vibration that is not counteracted by the anti-vibration bench will result in an error in the optical circuit. Although it was possible to separate the disc mechanically from the optical circuit, shortening the optical path length, *i.e.* the distance along the optical path from the laser to the sample, by 125 mm was considered to reduce the error further. The shaft was designed to be run by a pulley with gearing ratios of 5:1, 3:1, 2:1 and 1:1 from a 650 W brushless motor, The motor speed was digitally controlled with a pulse width modulated signal from an Arduino Mega microcontroller board, as shown in figure 7.4, so that f increased smoothly. The electronic control of the rotation

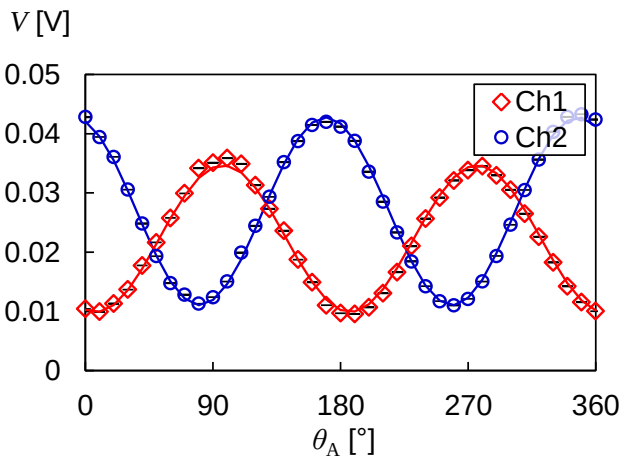

Figure 7.5: Variation of the signal intensities as a function of the analyser angles.

speed was developed as part of this project with contribution from Mr. B. Ng. The pulse width modulated signal was a $V_{\mathrm{pp}} = 5$ V square wave with a 20 ms period. The pulse duration was varied from 3 to 5 ms using the microcontroller board which was controlled through a LabView interface.

7.2.1 Sample preparation

High purity, 99.95 %, 0.1 mm thick foils were prepared for the measurements. Initially the samples were cut using a punch to cut a 1.5 mm diameter sample. This caused bowing at the edge of the sample which made observation of the moment at the edge of the sample difficult. Initially Platinum was measured, but the results were of a poor quality due to the bowing issue. To increase the magnitude of the observable effect, Tungsten was chosen which has a spin-orbit coupling constant, η_{SO}, of ≈ 9, as shown in table 6.1. As Tungsten was far too brittle to be punched, the samples were laser cut, which significantly reduced bending and bowing to the sample. The samples were then polished to a < 1 µm finish using a series of diamond lapping papers (15 µm, 9 µm, 3 µm and 1 µm) and were then finished using an Alumina suspension of particles with 0.05 µm particle diameter. As explained, the samples were then glued to NdFeB magnets. The change in thickness of the samples during the measurement process was negligible, remaining at 0.1 µm nominal thickness.

7.2.2 Preliminary measurements

As explained in section 7.1.2, the polariser and analyser were set in opposition to remove any background signals. For the polar MOKE measurement an S polarised beam was

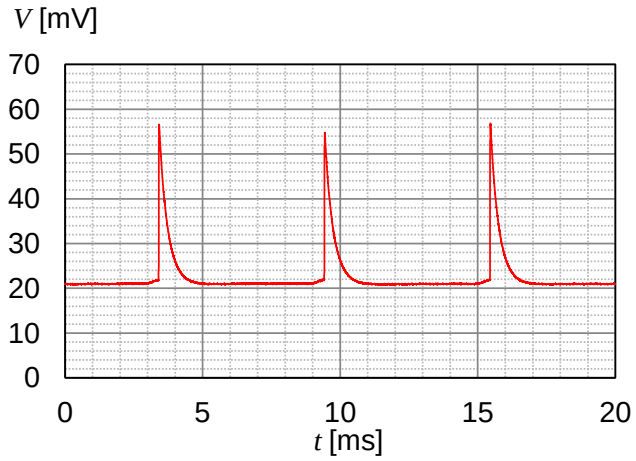

Figure 7.6: Example of the signal obtained from one of the photo-detectors.

incident on the sample. In the linearly polarised case this notation is arbitrary but means that the direction of polarisation, magnetisation and analyser angle are orthogonal. The intensity detected by the two photo-detectors now varied in opposite directions in response to a change in polarisation. The analyser angles were calibrated for each sample. The polariser angle was fixed and the two analyser angles were rotated through 360° as the sample was rotated at $f = 50$ Hz. A response curve of the peak height as the sample passed under the beam was plotted. The response curve was fitted with a sine squared function via a least squares fit, as shown in figure 7.5. For the calibration data shown in figure 7.5 the ideal analyser angles were extracted from the plot and found to be (51.2±0.3)° and (38.2±0.3)° for analyser (channel) 1 and 2 respectively. The angles were extracted by fitting a $\sin^2$ curve to the data using a least-squares fit and finding the values of the angle at the maximum gradient of the fit. The difference in the angle was due to slight variation in the polarising angle of the two detectors as purchased. As stated, the calibration was undertaken for each sample. To ensure that the calibration conditions and the measurement conditions were the same the plate was rotated until the bearings were warm, typically for 20-30 minutes. Therefore, each sample started at the same "zero" point; the magnetic moment at 50 Hz. As a result, any changes in Kerr rotation and the corresponding magnetic moment is directly comparable.

The voltages generated by the photodetectors were measured by a Tektronix DPO 7354C 3.5 GHz oscilloscope. As the sample passed underneath the beam the reflected light was detected as a signal pulse. The oscilloscope was operated in a high resolution mode where the effective bandwidth was 22 MHz. The average of V_{pp}, the height of the pulsed signal, was acquired over a 100 ms window for the two channels. An example of the pulsed data taken over a shorter acquisition, is shown in figure 7.6. The rise time of the photodetectors was specified to be 14 ns [126]. This is reflected in the sharp rise in the voltage at the beginning of the peak in figure 7.6. The rise time in a photodetector

is given by

$$t_{\mathrm{rise}} = 0.35 \times 2\pi R_{\mathrm{load}} C_{\mathrm{j}} \tag{7.9}$$

where R_{load} is the load resistance (50 Ω) and C_{j} is the diode junction capacitance (40 pF [126]). However, the signal would typically display a considerably longer fall time, or tail length, of approximately 1 ms, as shown in figure 7.6.

The increased fall time could be due to a combination of factors. Firstly, some time was taken up by the transit of the sample under the beam. By performing simple calculations it can be found that at a radius of 10 cm and a frequency of 200 Hz a sample of 1.5 mm diameter will take approximately 12 μs to pass under the beam. This value will, of course, be longer at lower measurement frequencies. These values were chosen for comparison with the data in figure 7.6 which was taken at approximately 200 Hz and show a good agreement with the pulse width displayed in figure 7.6 even though the time scale in the figure is larger than this. Secondly, the fall time in this measurement was dominated by charge carrier recombination outside the depletion region of the photodiode. Although the spot size of the laser was measured to be 450 μm at the surface of the sample, there was some scattering of the beam upon reflection causing a slight divergence from the otherwise collimated beam. This resulted in dispersal of the beam over the path length from the sample to the photodetectors. Not only this, but the beam itself was Gaussian in form (reflected in the measurement of its width, discussed in section 7.1.3). Therefore, including the tail, the beam is likely to be of up to 1 mm in in diameter. As a consequence, the beam that was incident on the photodetectors was larger than the depletion region, or active area, of the photodiodes (2.2×2.2 mm [126]). Charge carriers generated outside the depletion region and in the substrate have a recombination time of several microseconds [127].

However, the fall times observed in figure 7.6 are two orders of magnitude larger than can be accounted for using the arguments above. The origin of the tail length observed in figure 7.6 is unclear, however, fall times of up to ms in order of magnitude have been observed in other systems due to bias application and the capacitance of the junction [128]. The rise time was still short enough to probe the moment at the leading edge of the sample, where it was expected from the prediction that the spin current would accumulate [18]. As the beam spot size and interaction volume was large compared to typical spin diffusion lengths (450 μm compared to $\approx$ μm) probing the leading edge alone is preferable to taking a measurement across the sample as a lot of the signal would be averaged out. The peak to peak voltage, V_{pp}, changes upon increasing the frequency in the absence of an applied field. The quantity of interest was the change in $\frac{dV_{\mathrm{pp}}}{df}$ with different applied fields.

In summary a measurement system was developed that could take a reproducible measurement of the magnetic moment on the surface of a metallic foil at high frequency (200 Hz), where the laser was only incident on the surface of the magnet for approximately 10 µs. Calibration of the analysers was undertaken, which was repeated for each measurement. As stated, the design was relatively simple. However, the marriage of mechanical system to an optical system was not simple. Any vibration or oscillation of the sample would cause a change in the angles of the incident and reflected beams. This changed the amplitude of the signal detected by the MOKE, manifesting as noise and spurious signals in the measurement. The system presented here is the culmination of the development of a system that has taken several forms that was reached once the mechno-optical artefacts had been removed.

Chapter 8

Observation of a spin current induced by mechanical rotation

In this chapter the observation of a spin current in a Tungsten foil induced by mechanical rotation is presented. Further to the description of the experimental setup and components in chapter 7, this section describes the exact procedure for the accurate measurement of the change in magnetic moment in a foil as a function of the applied magnetic field strength. The change in moment arises from the rapid rotation up to 200 Hz of the Tungsten sample and the subsequent generation of a spin current within the sample. The presence of an accumulated spin current at the edges of the sample would manifest as a change in the moment and would be detectable by a method such as MOKE magnetometry, described here. The presence of a spin current in a paramagnetic foil was predicted by Matsuo *et al.* in 2011 [18], and the observation of the phenomenon as described in their proposed experiment follows.

8.1 MOKE calibration

As discussed in section 7.1, the intensity at the photodetectors follows the relationship

$$\Delta\mathbf{m} = A_{\mathrm{B}} + A_0 \sin^2(\phi - \Delta\theta_{\mathrm{K}}) \approx \Delta A\,, \tag{8.1}$$

where $\mathbf{m}$ is the moment of the interaction volume, A_{B} is the non-magneto-optical background amplitude, A_0 is the amplitude at maximum analyser transmission, ϕ is the analyser angle and θ_{K} is the Kerr rotation. Therefore the linearity of the response is sensitive to the initial magnetic moment of the sample and the relative orientation of the

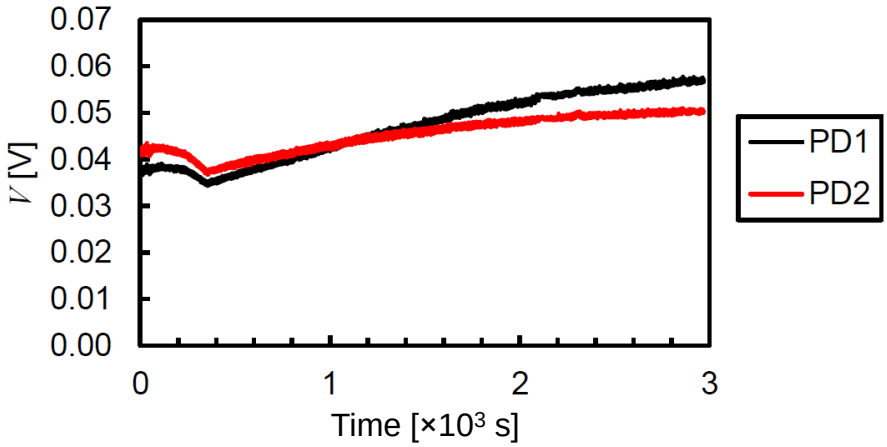

Figure 8.1: Measurement of the photodetector stability.

analysers. To identify the ideal analyser angles, the plate was rotated at approximately 50 Hz and a plot made of the peak height versus analyser angles. A sine squared curve was fitted to the data by a least squares fitting method. The analyser angle in the linear region of the sine squared curve was extracted for the analyser pair. The analyser angles were then set to these values. This process was repeated for each sample so that the measurements were comparable between samples.

The stability of the laser and photodetectors was investigated. The sample was rotated at a frequency of 50 Hz and the peak height response was plotted as a function of time. The laser is stable to 0.1% and the signal is clearly photodetector dependent so the variation in the signal intensity in figure 8.1 is due to the photo-detectors alone. There is a gradual drift of 20 mV across the course of the measurement in the first photodetector (black line) and a drift of approximately 10 mV in the second detector (red line). Given that the measurement protocol calls for the subtraction of one signal from the other, this will lead to a systematic drift in the measurement of the Kerr rotation.

The signal was measured as a function of magnet field strength. The magnetic field strength was varied by using magnets of different heights, h, and a brass stub of the same dimensions was used for the zero-field (reference) result. Measuring the field strength at the precise locality of the surface of the magnet was difficult to achieve. Without going to the length of patterning a Hall bar device on the magnet and taking an electrical measurement to determine the field, probing the field strength at the position of the foils at the surface was actually unachievable. It was expected that the stray/demagnetising field lines at the surface would be highly divergent due to the shape of the magnets. To achieve as accurate a measurement as possible a Hall probe with the sensing element set in 0.85 mm wide epoxy was used. The sensing element would therefore be no more than

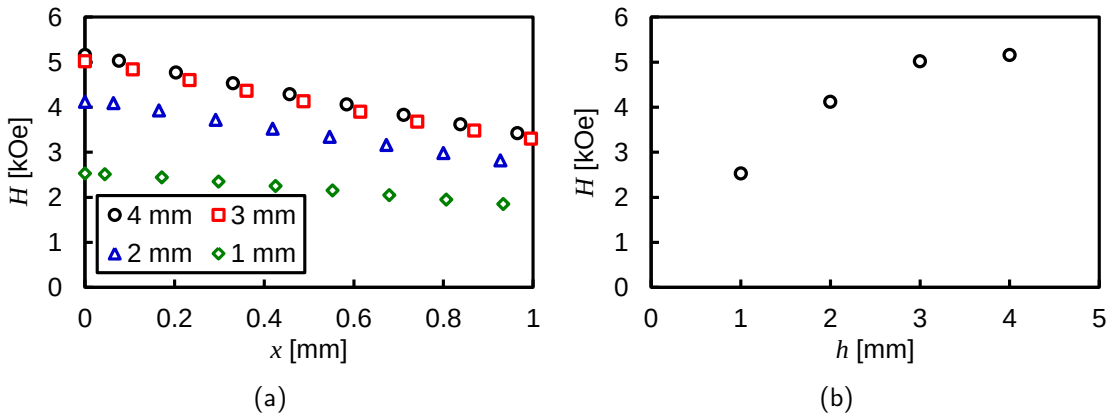

Figure 8.2: (a) Perpendicular stray field as a function of the distance from the surface of the magnet and (b) the stray field at the surface of the magnets for different magnet heights.

half this distance away from the surface. The thickness of the foils was approximately 0.1 mm. A plot of the field strengths as a function of the distance from the surface for N45 magnets of 5 mm diameter and varying height is shown in figure 8.2(a). Here it can be seen that the variation of the field with the distance from the surface is insignificant compared to the magnitude of the field for the magnets of height $h = 1$ mm, 2 mm and 3 mm. The 3 mm and 4 mm magnets have field strength values of (5.02±0.01) and (5.16±0.01) kOe respectively. These values are closer but are separate enough within the error of the measurement to be considered accurate values of the field at the surface of the magnet. A plot of the surface field strength for the different heights of magnet used is shown in figure 8.2(b).

8.2 Signal frequency response

At frequencies below 10 Hz the voltage pulse generated by the photodetectors in response to the incident light was that of the voltage detected for a stationary sample. As the frequency of rotation was increased, the pulse height decreased due to the reduction in acquisition time that the reflected beam is incident upon the active region of the photodiode. A typical data set for a Tungsten sample is shown in figure 8.3. Here the frequency is swept from 50 Hz, 3,000 rotations per minute r.p.m.) to the maximum frequency available: 200 Hz, 12,000 r.p.m.. The reduction in acquisition time reduces the magnitude of the current produced by the avalanche event in the biased detector and so follows a $1/f^2$ relationship, as shown in figure 8.3. To remove as much of this background frequency response as possible, the analysers were set in opposition, a process discussed in depth in section 7.1. However, there will still be some residual

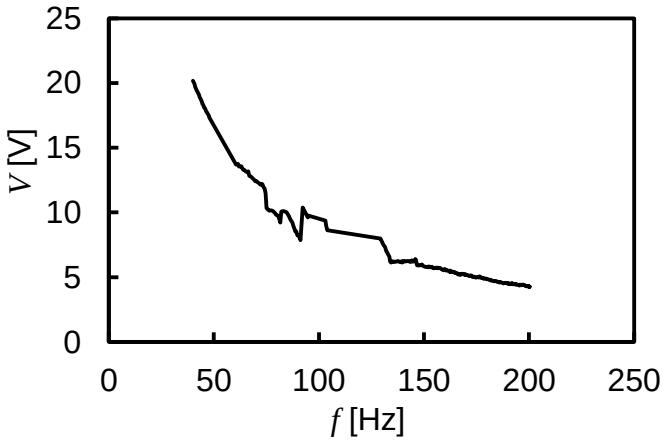

Figure 8.3: Frequency response of the MOKE signal.

frequency dependent component, but total elimination would not be possible.

The magnitude of the signal is largely dependent upon the quality of the sample preparation. Typically, the raw signal amplitude at a frequency of 50 Hz is tens of volts. Other than the clear reduction in magnitude with frequency there are regions along the curve where the signal deviates from the $1/f^2$ relationship. These regions are due to mechanical resonances in the system which occurred at 75 – 90 Hz and 135 – 145 Hz and were observed in all frequency sweeps. So that the frame and holding bolts were not put under unnecessary strain these frequencies were avoided by taking the measurement between 150 and 200 Hz. The signals from the two optical channels were subtracted (after the beam splitter) to remove the background frequency dependence and any vibrational or resonant noise effects that were contained in both channels.

A typical set of data is shown in figure 8.4. The data in figure 8.4 are from a sample

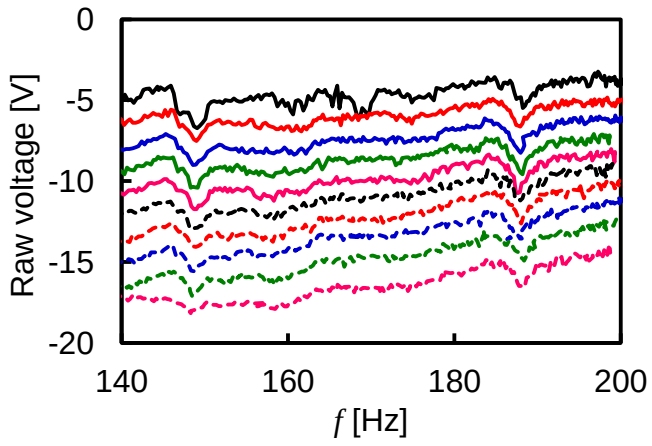

Figure 8.4: The frequency response of the MOKE signal due to the change in the moment as a result of spin accumulation at the edge of the sample.

of Tungsten foil. The Tungsten foil was 1.5 mm in diameter and glued to the surface of the magnet. The NdFeB magnet had an energy product of 42 MG·Oe and a field strength at the surface of the magnet of 1.91 kOe. The data sets are of the difference between the two channels to yield the Kerr rotation as outlined in section 7.1. The solid black line was the first measurement taken with the pink dashed line being the last. Given the method of data acquisition there is a reduced, but not completely eliminated, photodetector frequency response. However, the gradient of all the frequency sweeps agree within the error of 0.0002, confirming the validity of the measurements. The frequency sweeps were taken consecutively and shift down systematically by approximately 1.5 V. The data-set shows that there are still mechanically resonant features in the frequency response that have not been removed by the two channel method. However, given the reproducibility of the data these were ignored. It is also apparent that the noise on the measurement reduced over the length of the measurement. This was attributed to the bearings in the frame heating up and expanding. This led to a smoother running of the rotating plate. The bearings were warmed up by running the measurement at 150 Hz for 15 mins before measurement.

8.3 Data analysis

The raw data sets were taken and normalised to the peak amplitude at 140 Hz. The same data as shown in figure 8.4 is shown normalised in figure 8.5(a). Once the data have been normalised there is a clear agreement between the data sweeps. There are peaks in the data at approximately 150 Hz and 190 Hz. These are due to mechanical resonances, a conclusion that was very obvious when taking the measurement. The mechanical resonances are most apparent in the first measurement when normalised. Therefore, the first measurement was discounted from further analysis as it clearly contained a systematic error that was significantly reduced in subsequent measurements and would have provided an anomalous bias to the data.

The data was then averaged and the error calculated as the standard error of the mean. Figure 8.5(b) shows the averaged data. It is the change in the magnetic moment of the interaction volume with frequency that is of interest. The slope of the signal between 150 Hz and 200 Hz will give a measure of the change in moment due to the change of frequency. In section 6.2 the prediction of the magnitude of the induced spin current was discussed. The conclusion of the prediction is summarised and reproduced below. The spin current induced in the foil has a current density given by:

$$j_{\mathrm{S}}^{0}(r) = 2nq_{\mathrm{e}}\eta_{\mathrm{SO}}\frac{\hbar\Omega\omega_{\mathrm{C}}r}{E_{\mathrm{F}}}\,. \tag{6.14}$$

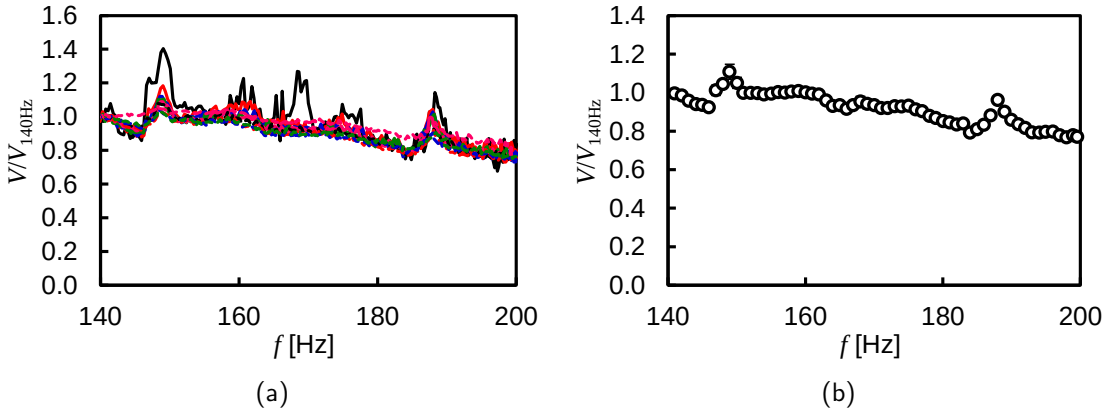

Figure 8.5: (a) Normalised and (b) averaged, normalised frequency response of the MOKE signal due to the induced spin currents.

Here, n is the electron number density, q_{e} the electronic charge, η_{SO} the spin-orbit coupling strength, $\hbar$ the reduced Planck constant, Ω the angular frequency, ω_{C} the cyclotron frequency, r the radius from the centre of rotation and E_{F} is the Fermi energy for the electron wave-packet. Here, it can be seen that the spin current is expected to increase linearly with frequency. The dominating factor in the signal is the reduction in signal due to the increase in frequency and the resultant decrease in the exposure time of the photodiodes. The increase in signal due to the change in moment will superimpose onto this background response. Therefore a straight line was fitted to the data between 150 Hz and 200 Hz to confirm this relationship. There is indeed a linear frequency dependence upon the observed signal. As stated in equation (6.14) there is also a linear field-dependence in the cyclotron frequency term. Accordingly the field was varied by changing the permanent magnet.

8.4 Change in moment as a function of magnetic field

The change in moment with frequency, $\frac{d\mathbf{m}}{df}$, between 150 Hz and 200 Hz as a function of the magnetic field strength is shown for Tungsten in figure 8.6. $\frac{d\mathbf{m}}{df}$ shows a clear magnetic field strength, H, dependence. In the region between -2.5 kOe and 2.5 kOe the behaviour is linear, as would be expected from the induced Barnett field, given by:

$$\mathbf{B}_{\Omega} = \frac{2m_{\mathrm{e}}}{gq_{\mathrm{e}}}\mathbf{\Omega} \tag{6.3}$$

where g the Landé g-factor, q_{e} the electronic charge, m_{e} the electronic rest mass and $\mathbf{H}$ is the applied magnetic field.

There is a change of 11% due to the rotational effect of the Barnett field from

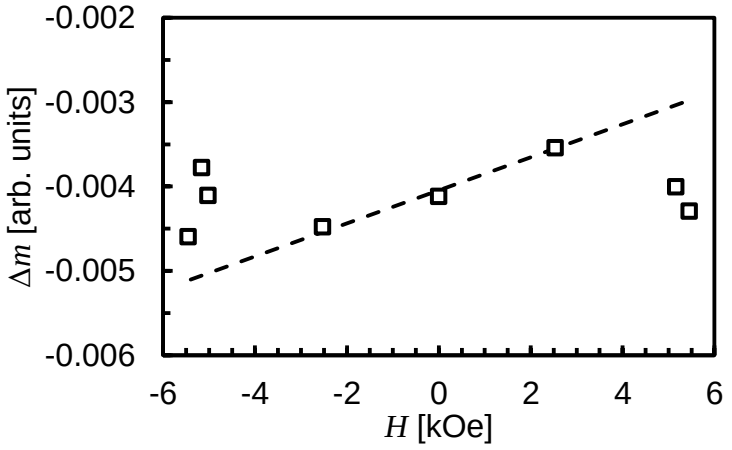

Figure 8.6: Change in moment as a function of applied magnetic field for a 1.5 mm Tungsten (99.95%) foil. The straight line is fitted to the linear region and extended to show the deviation of the detected moment at higher fields. Measurements were taken by Y. Baba.

the 0 kOe (null) sample. Beyond these field values the rotational effect then goes on to augment the change in moment, $\Delta\mathbf{m}$, in the opposite direction by 18% from the values at -2.5 kOe and 2.5 kOe. The incident laser will probe the surface to a depth of approximately 50 nm at the first edge of the sample. Beyond the first edge the cascade effect within the photodetector will mask any further change in moment on the remaining sample as the surface passes under the beam and the current in the photodiode decays. The non-monotonic increase/decrease in magnetic moment beyond the Barnett region indicates that the spin accumulation at the probed edge of the sample acts to oppose the magnetic moment induced in the foil due to the applied magnetic field. The spin current is also not observed until higher fields a threshold spin current is required before spins of opposite sign migrate to the edges of the sample and they become detectable. *However*, the measurements that were taken at higher field values show clear deviation from the linear Barnett dependency. The variation in this deviation does vary which was due to variation in the sample preparation, from asperities at the surface and edges of the samples.

It is important to note that the induced spin current is highly sensitive to the sample condition and frequency. The induced spin current is expected to follow a cubed, squared or linear relationship depending on the limits used. As stated in section 6.2 and reproduced below for continuity, the spin current induced by rotation consists radial and azimuthal components that have non-linear H dependency. However in the limits applied due to the experimental condition, *i.e.* $(\tau_{\mathrm{S}}\omega_{\mathrm{C}})^2 \ll 1$, the relationship is expected to be linear, following

$$j_{\mathrm{S}}^{0}(r) = 2nq_{\mathrm{e}}\eta_{\mathrm{SO}}\frac{\hbar\Omega\omega_{\mathrm{C}}r}{E_{\mathrm{F}}}\,. \tag{6.14}$$

where n is the electron number density, q_{e} the electronic charge, η_{SO} the spin-orbit coupling strength, $\hbar$ the reduced Planck constant, Ω the angular frequency, ω_{C} the cyclotron frequency, r the radius from the centre of rotation and E_{F} is the Fermi energy for the electron wave-packet. As stated there is a clear divergence from the linear Barnett effect in the region beyond $|H| = 2.5$ kOe. This is indicative of the presence of an additional moment within the sample, attributed to the spin current predicted by Maekawa *et al.* [18].

The presence of a spin current above a critical field at 150 - 200 Hz has been observed in Tungsten. Efforts were made to support the result by using a different material, Platinum, thereby changing the spin orbit coupling strength and the induced signal. This has so far proved difficult to be achieved as Platinum has a spin-orbit coupling constant some 20 times less than Tungsten. The most time effective and simple way to prepare the samples was by laser cutting. Being of high tensile strength (yet very brittle) Tungsten was relatively easy to handle and polish to a mirror (< 1 µm) finish. This made Tungsten an ideal material for preparation by this method. However, Platinum, being more malleable, polished easily but was easily bent at the edges, reducing the observed spin signal a reproducibility of the measurements. A linear dependency on the fields applied to the samples was observed with Platinum, but the reproducibility was not as good as for Tungsten. To unambiguously prove that the observed change in moments at higher fields is due to the presence of a spin current a range of materials such as Platinum, Palladium and Silver could be investigated. In doing so, careful attention should be paid to the sample preparation procedure.

Chapter 9

Conclusions and future work

The aims of this work were laid out in chapter 1. This project had two distinct objectives that contributed to the one theme: the understanding of electron spin transport. Electron spin transport covers a broad set of phenomena, but specifically in this project the focus has been on the diffusion of electron spins. Irrespective of any electron drift, *i.e.* a charge current, an increase in polarised electron spin density results in a diffusion of the electron spin polarisation. The first part is concerned with using the principles that govern electron spin-diffusion currents to inspire the design of spintronic devices with improved efficiency. The second part is concerned with the generation of an electron spin current by mechanical rotation. The conclusions drawn from these two parts are addressed below in the same order.

9.1 Observation and operation of spintronic devices

A measurement cell was developed, as described in chapter 3, so that a standard on-Silicon device could be mounted in an 8 mm leadless chip carrier (LCC), itself in an LCC socket mounted in a block for magneto-resistive measurements. This mirrors the standard process used in semiconductor device testing. A wide variety of test parameters were made available. The measurement cell was designed to fit between the pole pieces of an electro-magnet in a cryostat for low temperature measurements. As well as this cryostat compatible cell, an LCC socket was mounted on a brass finger that could be adjusted to achieve a variety of applied field angles.

There were a number of issues that defined the maximum allowable currents that could be passed through the devices. At the nanometric dimensions that were investigated a 100 μA corresponds to a current density of the order of 1 MA/cm^2. The

magnitude of the changes in resistance that were measured were of the order of mΩs, leading to the requirement of a voltage measurement system sensitive to changes in voltage of 100 nV or so. Chapter 3 describes the process and method used to take voltage measurements with a noise of down to 10 nV. Nanoscale lateral spin-valve, LSV, devices were successfully fabricated with spin transport characteristics that fall in line with known values for the materials that were investigated, summarised in table 5.2. Therefore, a fabrication, preparation and measurement process was developed that could reproducibly be used to test novel spintronic devices. After a number of months of development a yield for the total process, from fabrication to a testable, on-chip device of 10% was achieved.

A state of the art electron-beam lithography system was successfully utilised to fabricate novel spintronic devices. The sub-5 nm resolution of the JEOL JBX-6300FS was used to fabricated 100 nm sized metallic features with a typical r.m.s. roughness along the length of a wire of 2.6 nm. The origin of geometrical spin filtering [60] was confirmed. This part of the project was based on the work of a previous student [65]. The amplification by spin filtering that was observed by Abdullah *et al.* [60] in asymmetric spin diffusion channels was not observed in symmetric spin diffusion channels. This supports the phenomenological hypothesis put forward; that the diffusion currents will see a directionally dependent resistance due to changes in the diffusion channel geometry. The increase in the spin signal by almost an order of magnitude has already been observed [60] and the mechanism that provided this has been confirmed in this work. The filtering of a diffusive spin-current is a way of overcoming the poor operational efficiency of all-metal LSV devices.

The more efficient operation of an LSV device with the application of a perpendicular magnetic field of approximately 0.1 kOe was observed. The introduction of a medial ring to an LSV and the application of a gate magnetic field increased the spin diffusion length from that found in straight wire LSV devices from (310$\pm$30) nm to (410$\pm$60) nm . This 30% increase in the spin diffusion length provides an augmentation to the functionality to such LSV devices. As with the amplification of a spin current, the utilisation of a field gradient across the ring for efficient gate operation of spin diffusion currents is another way in which the operational inefficiencies of LSV devices may be overcome.

The results presented here show that there is a real possibility of overcoming the problem of operational efficiency that faces all-metal spintronic devices. The International Technology Roadmap for Semiconductors states that in 2014 the feature sizes achieved were down to 14 nm and the 10 nm features that it predicts for 2016 are still under development, with the announcement of the successful fabrication of a 7 nm node in 2015 [129]. There will, of course, be a physical limit to the feature sizes that can

be produced due to stray field effects, Joule heating and other consequences of passing currents through such small features. The solution to this problem is, in part, the improvement of fabrication techniques. However, a change in the way that devices are operated will be required to overcome size limitations. All-metal spintronic devices are a possible alternative, with their viability being strengthened by the results presented here.

9.2 Generation of a spin current by mechanical rotation

The second part of the project was focussed on the design, build and evaluation of a measurement system to allow the verification of a hypothesis by Matsuo *et al.* for the generation of a spin-current by mechanical rotation [18,19,114]. The experimental setup was, in principle at least, simple and it would not be difficult to set up such an experiment with reasonably standard lab equipment. A DC MOKE magnetometer was adapted to provide a measurement that would cancel out any global sources of noise, *e.g.* vibration and surface scattering. The optical system was then married to a mechanical rotating system for the observation of a mechanically induced spin current. The opto-mechanical system was difficult to optimise due to the opposition of experimental conditions and measurement sensitivity, *i.e.* as the roational frequency of the plate increased, the noise on the measurement tended to increase. Given that other methods used to probe this effect have yet to provide experimental confirmation of the phenomenon, it would seem that this simple and non-contact method is effective.

It was shown that the moment (and the corresponding spin current) within a foil can be probed by a non-invasive optical method, MOKE, whilst rotating the sample at frequencies up to 200 Hz with an applied field in the rotating frame of the sample. In the low field limit ($|H| < 2.5$ kOe) the change in magnetic moment with frequency, $\frac{d\mathbf{m}}{df}$, at the surface of the foil followed a linear relationship with H as expected from the Barnett effect [17]. Beyond the low field limit ($|H| > 2.5$ kOe) $\frac{d\mathbf{m}}{df}$ deviated from its linear H dependency, indicating the presence of another effect that was affecting the change in the induced magnetic moment. This is indicative of the presence of a spin current as predicted by Matsuo *et al.* [18, 19, 114]. The indication of the presence of a spin current due to mechanical rotation confirms the presence of an electric field through general relativistic effects and the presence of a spin current produced through the spin orbit interaction. This experiment also provides a more intuitive demonstration of the spin-orbit interaction as a coupling of an electron's angular momentum and motion.

9.3 Future work

For the observation and operation of spin diffusion in LSVs the measurement system requires some further development. The fabrication process was the limiting factor to the realisation of operating spintronic devices. The Permalloy injector and detector pair were found to have an injection polarisation of 0.2 in this study. Given the known polarisation of Permalloy in the bulk material of 0.7 [56], this implies that there is a loss of polarisation due to an electronic depolarisation at the interface between the Permalloy and the Copper. This could be due, in part, to a spin conductivity mismatch between the Permalloy and the Copper. However, the most significant factor was the preparation of the interface during fabrication. The interface was exposed to air in between deposition steps and although Ar ion milling was employed to prepare the interface before depositing Copper, it is expected that resist residue and oxidation was not completely removed.

Therefore, a range of conducting channel materials and interface preparation methods could be used to address the spin conductivity mismatch at the interface. Ideally an injector material with 100% spin polarisation, such as a Heusler alloy, should be used for optimal operation characteristics. The Heusler alloy Co_2MnSi (CMS) has been shown to have an effective spin polarisation of 63% [64]. Although oxides can be used to improve the injection efficiency, they tend to decompose structurally at small dimensions. Dusting of the interface with materials such as Manganese has been show to increase the exchange bias in coupled layers [130] and so a similar method could be used to improve the spin-conductivity matching at the interface. A materials/fabrication study of this nature would be a significant body of work but would yield much larger spin signals and therefore make the observation of spin transport phenomena such as interference and amplification more apparent. Further to this, a study of the spin-transport characteristics at a liquid Nitrogen, or perhaps even Helium, temperatures would yield signals that were larger by an order of magnitude or so, having been shown to do so in works such as ref. [58]. The cryostat and probe system designed, developed and built in this project – discussed in section 3.3 – could be used to such an end.

In order to confirm the origin of what is proposed to be the generation of a spin current by mechanical rotation, further measurements need to be taken on different materials, thus changing the spin-orbit coupling constant, η_{SO}. A suitable material would be Platinum or Palladium, as it is known that these materials have a lower spin-orbit coupling strength, a high density of electrons at the Fermi level and would have similar reflective qualities. This would prove, beyond doubt, that the effect observed in this work was a spin current induced by mechanical rotation.

In this part of the project, the most difficult aspect was the production of samples

with the same optical and electronic properties. These were defined by the thickness, edge definition and surface roughness. Initially the samples were cut using a circular punch, damaging and buckling the edges of the samples. This was overcome by laser cutting the samples, which provided a much cleaner cut at the edge and therefore a greater component of the signal was detected at the edge of the sample, where spin accumulation occurs. Even then, it was difficult to obtain highly consistent data between samples, due to their distributions in the surfaces smoothness and minor instability in their rotation. Further headway should be made in producing samples with improved uniformity, reflective surface and edge definition. An alternative method to achieve this would be through deposition of the material (Tungsten, Platinum or Palladium) through a mask by sputtering or evaporation. The roughness of the magnet surfaces was visible to the naked eye, so would have to be prepared by the deposition of a smoothing Nickel layer. Once smoothed to less than 1 μm roughness, the paramagnetic material, *e.g.* Platinum, could be deposited by sputtering or evaporation through a mask to a thickness of at least 50 nm to match the penetration depth of the laser. This would provide a reproducible way to deposit highly reflective samples of uniform thickness. Careful consideration would have to be paid to the edge definition of the sample, as mask deposition techniques are known to produce shadowing at the edges. Furthermore, heating of the permanent magnet during deposition may alter its magnetisation. This could be overcome by the application of a setting field to the magnet when the sample is cooling after deposition by sputtering or evaporation.

The mechanical rotational system itself is suitable for the measurement of materials that have a high spin-orbit coupling strength. To measure samples with a lower spin-orbit coupling strength, such as Silver and Palladium, the whole system would have to be properly engineered to incorporate a motor with a higher maximum speed. Brushless motors that can roate at speeds of up to 100,000 rpm are readily available and the use of such a motor with an air bearing may reduce the vibration at high frequency. Potentially one could consider using a blade design rather than a plate to reduce the rotational inertia. However, the rigid plate design ensures the rotation of the sample around a fixed path.

List of symbols

$2w$	Full beam diameter. 122
A	Amplitude. 119–121, 129
a	Area. 40, 41, 49, 95, 106, 107
α	Spin polarisation. 34, 38, 39, 46, 49, 106–108
α_0	Damping factor. 28, 49, 52
α_1	Dirac matrix. 114
B	Magnetic flux density. 30, 47–49, 83, 106, 107, 112, 115, 116, 119, 124
$\mathbf{B}_\Omega$	Barnett field. 112, 113, 134
β	Bandwidth. 64
β_1	Dirac matrix. 114
C	Capacitance. 127
c	Speed of light in a vacuum. 30, 114
C_S	Seebeck coefficient. 31
χ_O	Magneto-optical susceptibility. 32
D	Diffusion constant. 37, 38, 42, 45, 48, 49, 106–108
$D_\mathrm{s.d.p}$	Spin diffusion prefactor. 38–40
δ	Kronecker delta. 43
E	Electric field. 30–32, 115
e	Euler's number. 31, 35, 43, 45, 116, 122
E_D	Dielectric tensor. 119
E_F	Fermi energy. 34, 116, 133–136
η_SO	Spin orbit coupling factor. 31, 116, 117, 125, 133–136, 140
$\mathbf{F}$	Force. 115
f	Frequency. 32, 64, 65, 121, 124, 126, 127, 134, 139
g	Landé g-factor. 22, 28, 48, 112, 113, 119, 134
γ	Gyromagnetic ratio. 27, 28, 52

γ_{e} Electron gyromagnetic ratio. 112

$\mathcal{H}$ Heisenberg Hamiltonian. 27, 28, 52, 112, 114, 119, 134–136, 139
h Height. 100, 101, 130, 131
H_{C} Coercive field. 78
$\hbar$ Reduced Planck constant. 22, 23, 48, 114–116, 133–136

I Charge current. 34, 66, 75, 77, 87, 94
i Imaginary unit. 48, 114, 119

j Current density. 23, 24, 31, 38, 39, 44, 45, 87, 116, 133, 135
J_{ex} Exchange interaction coefficient. 27, 28

k Wave vector. 116, 120
k_{B} Boltzmann constant. 64

L Length. 38–42, 45, 49, 75, 77, 91–94, 106–108
ℓ Azimuthal quantum number. 32
λ Spin-orbit coupling. 115, 116
λ_{w} Hanle spin diffusion length. 48, 83
λ_{S} Spin diffusion length. 35, 38–42, 45, 48, 49, 69, 83, 94–96, 106, 107

M Local magnetisation. 23, 24, 27, 28, 32, 52, 119
$\mathbf{m}$ Magnetic moment. 120, 121, 129, 134, 135, 139
m_{e} Electron rest mass. 22, 23, 30, 83, 112–114, 134
m_j Secondary total angular momentum number. 32
μ Chemical potential. 31, 35, 37, 38, 43, 45, 48
μ_{B} Bohr magneton. 23, 28, 48
μ_{S} Spin magnetic moment. 22, 43, 45

N Refractive index. 119
n Unit vector. 116, 133–136
$N_{\uparrow/\downarrow}(E_{\mathrm{F}})$ Spin density of states at the Fermi energy. 34, 37
n_{e} Electron density. 42

Ω Angular frequency. 112–116, 133–136
ω_{L} Larmor frequency. 49, 83, 106, 107
ω_{C} Cyclotron frequency. 48, 83, 116, 133–136

$\hat{\mathbf{p}}$ Momentum operator. 30, 112
P_{i} Spin polarisation injection efficiency. 39–42, 94, 95
ϕ Analyser angle. 120, 121, 129
$\boldsymbol{\pi}$ Dirac matrix. 114
Ψ Wavefunction. 114

Q Magneto-optic constant. 119
q_{e} Electronic charge. 22, 23, 30, 37–39, 83, 112–116, 133–136

R Resistance. 26, 41, 64, 66, 67, 75, 94, 95, 124, 127
r Radius. 30, 42, 43, 45, 112, 114–116, 124, 133–136
R_{NL} Non-local resistance. 40–42, 49, 67, 78, 91, 94, 99–101, 106, 107
ρ Resistivity. 24, 25, 31, 37–41, 49, 71, 87, 95, 106, 107
ρ_{q} Charge density. 23

S Spin angular momentum. 22, 47, 112
s Spin quantum number. 22, 27, 28
$\boldsymbol{\Sigma}$ Spin operator. 114, 115
σ Pauli matrix. 108, 115

T Temperature. 31, 64, 94, 96, 117
t Time. 27, 28, 42, 43, 45, 49, 52, 83, 106, 107, 114, 127
τ Electron relaxation time. 49, 107
τ_{S} Spin relaxation time. 24, 25, 42, 45, 49, 116, 135
τ_{sf} Electron-spin averaged relaxation time. 37, 38, 48, 83
τ_{STT} Spin-transfer torque. 52
θ_{K} Kerr rotation. 119–121, 129
θ_{SH} Spin Hall angle. 116, 117

u Potential energy. 30

V Voltage. 38, 39, 64–68, 75, 77, 87, 121
v Velocity. 115
V_{NL} Non-local voltage. 67, 68
V_{pp} Peak to peak voltage. 125–127

w Width. 70, 73, 75–78, 82, 94, 96, 99, 102

x Distance. 34, 35, 37, 38, 48, 50, 70, 74

x_{90-10} Distance from 90% to 10% intensity across a beam cross section. 122, 123

List of abbreviations

AF	Antiferromagnetic. 27, 33
AMR	Anisotropic magneto-resistance. 14, 15
AP	Anti-parallel. 26
CMOS	Complimentary metal-oxide semiconductor. 16, 54
CMS	Cobalt-Manganese-Silicon (Co_2MnSi). 140
DC	Direct current. 52, 53, 69, 70, 81, 87, 122, 139
DRAM	Dynamic random access memory. 14
e-beam	Electron beam. 60
EBL	Electron beam lithography. 57, 60, 81
F	Ferromagnetic. 24–28, 30, 31, 33, 34
GMR	Giant magneto-resistance. 15, 16, 25, 26, 52
LCC	Leadless chip carrier. 63, 137
LLG	Landau-Lifshitz-Gilbert. 28, 48, 51
LSV	Lateral spin valve. 34, 36, 54, 71, 74–76, 79, 81, 82, 85, 86, 89–92, 97–99, 102, 103, 108, 109, 138, 140
MOKE	Magneto-optical Kerr effect. 86, 119–122, 128, 129, 132, 134, 139
MOSFET	Metal-oxide-semiconductor field-effect transistor. 81
MRAM	Magnetic random access memory. 14, 15
NM	Non-magnetic. 25, 26, 31, 34
NMR	Nuclear magnetic resonance. 113
P	Parallel. 26
PEEK	Polyether ether ketone. 63
PMMA	Poly(methyl methacrylate). 60

RA Resistance-area (product). 76
r.m.s. Root mean square. 64, 74, 96, 123, 138
r.p.m. Rotations per minute. 131

SEM Scanning electron microscope. 70, 72–74, 77, 79, 80, 82, 84–86, 88, 89, 101–103, 105
SRAM Static random access memory. 14
STEM Scanning transmission electron microscope. 57, 59
STNO Spin-transfer nano-oscillator. 52, 53
STT Spin-transfer torque. 28

TMR Tunnel magneto-resistance. 52

References

[1] E. Hall, "XVIII. On the "Rotational Coefficient" in Nickel and Cobalt," *Philos. Mag. Series 5*, vol. 12, no. 74, pp. 157–172, 1881.

[2] T. J. Seebeck, "Magnetische polarisation der metalle und erze durch temperaturdifferenz," *Abhandlungen der Königlichen Akademie der Wissenschaften zu Berlin*, pp. 265–373, 1825.

[3] Y. K. Kato, R. C. Myers, A. C. Gossard, and D. D. Awschalom, "Observation of the spin Hall effect in semiconductors," *Science*, vol. 306, no. 5703, pp. 1910–1913, 2004.

[4] K. Uchida, S. Takahashi, K. Harii, J. Ieda, W. Koshibae, K. Ando, S. Maekawa, and E. Saitoh, "Observation of the spin Seebeck effect," *Nature*, vol. 455, no. 7214, pp. 778–781, 2008.

[5] W. Thomson, "On the electro-dynamic qualities of metals:–effects of magnetization on the electric conductivity of Nickel and of Iron," *Proc. Roy. Soc. London*, vol. 8, pp. 546–550, 1856.

[6] O. W. Richardson, "A Mechanical Effect Accompanying Magnetization," *Phys. Rev. Series 1*, vol. 26, pp. 248–253, 1908.

[7] A. Einstein and W. J. de Haas, "Experimental proof of the existence of ampère's molecular currents," *Huygens Inst. - Roy. Netherlands Acad. of Arts and Sci., Proc.*, vol. 18, no. 1, pp. 696–711, 1915.

[8] M. N. Baibich, J. M. Broto, A. Fert, F. N. Van Dau, F. Petroff, P. Etienne, G. Creuzet, A. Friederich, and J. Chazelas, "Giant Magnetoresistance of (001)Fe/(001)Cr Magnetic Superlattices," *Phys. Rev. Lett.*, vol. 61, pp. 2472–2475, 1988.

[9] G. Binasch, P. Grünberg, F. Saurenbach, and W. Zinn, "Enhanced magnetoresistance in layered magnetic structures with antiferromagnetic interlayer exchange," *Phys. Rev. B*, vol. 39, pp. 4828–4830, 1989.

[10] K. Roy, S. Mukhopadhyay, and H. Mahmoodi-Meimand, "Leakage current mechanisms and leakage reduction techniques in deep-submicrometer CMOS circuits," *Proc. IEEE*, vol. 91, no. 2, pp. 305–327, Feb 2003.

[11] M. Buzzi, R. V. Chopdekar, J. L. Hockel, A. Bur, T. Wu, N. Pilet, P. Warnicke, G. P. Carman, L. J. Heyderman, and F. Nolting, "Single domain spin manipulation by electric fields in strain coupled artificial multiferroic nanostructures," *Phys. Rev. Lett.*, vol. 111, p. 027204, Jul 2013.

[12] N. Lei, T. Devolder, G. Agnus, P. Aubert, L. Daniel, J.-V. Kim, W. Zhao, T. Trypiniotis, R. P. Cowburn, C. Chappert *et al.*, "Strain-controlled magnetic domain wall propagation in hybrid piezoelectric/ferromagnetic structures," *Nature Commun.*, vol. 4, p. 1378, 2013.

[13] M. Johnson and R. H. Silsbee, "Interfacial charge-spin coupling: Injection and detection of spin magnetization in metals," *Phys. Rev. Lett.*, vol. 55, pp. 1790–1793, 1985.

[14] A. Fick, "Ueber Diffusion," *Ann. Phys. (Berlin)*, vol. 170, no. 1, pp. 59–86, 1855.

[15] S. Datta and B. Das, "Electronic analog of the electrooptic modulator," *Appl. Phys. Lett.*, vol. 56, no. 7, pp. 665–667, 1990.

[16] F. J. Jedema, A. T. Filip, and B. J. van Wees, "Electrical spin injection and accumulation at room temperature in an all-metal mesoscopic spin valve," *Nature*, vol. 410, pp. 345–348, 2001.

[17] S. J. Barnett, "Magnetization by Rotation," *Phys. Rev.*, vol. 6, pp. 239–270, 1915.

[18] E. S. M Matsuo, J Ieda and S. Maekawa, "Effect of mechanical rotation on spin currents," *Phys. Rev. Lett.*, vol. 106, p. 242501, 2011.

[19] M. Matsuo, J. Ieda, K. Harii, E. Saitoh, and S. Maekawa, "Mechanical generation of spin current by spin-rotation coupling," *Phys. Rev. B*, vol. 87, no. 18, p. 180402, 2013.

[20] M. Dyakonov and V. Perel, "Current-induced spin orientation of electrons in semiconductors," *Phys. Lett. A*, vol. 35, no. 6, pp. 459 – 460, 1971.

[21] J. E. Hirsch, "Spin Hall effect," *Phys. Rev. Lett.*, vol. 83, pp. 1834–1837, 1999.

[22] V. Sih, R. Myers, Y. Kato, W. Lau, A. Gossard, and D. Awschalom, "Spatial imaging of the spin Hall effect and current-induced polarization in two-dimensional electron gases," *Nature Phys.*, vol. 1, no. 1, pp. 31–35, 2005.

[23] H. Chudo, M. Ono, K. Harii, M. Matsuo, J. Ieda, R. Haruki, S. Okayasu, S. Maekawa, H. Yasuoka, and E. Saitoh, "Observation of Barnett fields in solids by nuclear magnetic resonance," *Appl. Phys. Exp.*, vol. 7, no. 6, p. 063004, 2014.

[24] R. Takahashi, M. Matsuo, M. Ono, K. Harii, H. Chudo, S. Okayasu, J. Ieda, S. Takahashi, S. Maekawa, and E. Saitoh, "Spin hydrodynamic generation," *Nature Phys.*, vol. 12, no. 1, pp. 52–56, 2016.

[25] P. I. Good and J. W. Hardin, *Sources of Error*. John Wiley and Sons, Inc., 2008, pp. 1–11.

[26] S. Maekawa, S. O. Valenzuela, E. Saitoh, and T. Kimura, Eds., *Spin Current*. Oxford University Press, 2012.

[27] S. Maekawa and S. Takahashi, *Spin Current*. Oxford University Press, 2012, ch. Spin Hall effect, pp. 194–208.

[28] H. N. Russell and F. A. Saunders, "New regularities in the spectra of the alkaline earths," *Astrophysical Journal*, vol. 61, p. 38, 1925.

[29] E. Saitoh, *Spin Current*. Oxford University Press, 2012, ch. Introduction, pp. 3–14.

[30] O. Stern, "A way towards the experimental examination of spatial quantisation in a magnetic field," *Zeitschrift für Physik D Atoms, Molecules and Clusters*, vol. 10, no. 2-3, pp. 114–116, 1988.

[31] R. Skomski and J. Coey, *Permanent Magnetism*, ser. Condensed Matter Physics. Taylor & Francis, 1999.

[32] A. Matthiessen and C. Vogt, "On the Influence of Temperature on the Electric Conducting-Power of Alloys," *Phil. Trans. Roy. Soc.*, vol. 154, pp. 167–200, 1864.

[33] N. F. Mott, "Electrons in transition metals," *Adv. Phys.*, vol. 13, no. 51, pp. 325–422, 1964.

[34] I. A. Campbell, A. Fert, and R. Pomeroy, "Evidence for two current conduction Iron," *Phil. Mag.*, vol. 15, no. 137, pp. 977–983, 1967.

[35] A. Fert and I. A. Campbell, "Two-Current Conduction in Nickel," *Phys. Rev. Lett.*, vol. 21, pp. 1190–1192, 1968.

[36] N. Mott, "The electrical conductivity of transition metals," in *Proc. Roy. Soc. London A: Math., Phys. Eng. Sci.*, vol. 153, no. 880. The Royal Society, 1936, pp. 699–717.

[37] S. M. Thompson, "The discovery, development and future of GMR: The Nobel Prize 2007," *J. Phys. D: Appl. Phys.*, vol. 41, no. 9, p. 093001, 2008.

[38] Y. Kajiwara, K. Harii, S. Takahashi, J. Ohe, K. Uchida, M. Mizuguchi, H. Umezawa, H. Kawai, K. Ando, K. Takanashi, S. Maekawa, and E. Saitoh, *Nature*, vol. 464, pp. 262–266, 2010.

[39] D. Ralph and M. Stiles, "Spin transfer torques," *J. Magn. Magn. Mater.*, vol. 320, no. 7, pp. 1190 – 1216, 2008.

[40] A. Hirohata and K. Takanashi, *J. Phys. D: Appl. Phys.*, vol. 47, p. 193001, 2014.

[41] G. E. Bauer, E. Saitoh, and B. J. van Wees, "Spin caloritronics," *Nature Mater.*, vol. 11, no. 5, pp. 391–399, 2012.

[42] A. Slachter, F. L. Bakker, J.-P. Adam, and B. J. van Wees, "Thermally driven spin

injection from a ferromagnet into a non-magnetic metal," *Nature Phys.*, vol. 6, no. 11, pp. 879–882, 2010.

[43] A. Hirohata, *Spin Current*. Oxford University Press, 2012, ch. Optically induced and detected spin current, pp. 194–208.

[44] Z. G. Yu and M. E. Flatté, "Electric-field dependent spin diffusion and spin injection into semiconductors," *Phys. Rev. B*, vol. 66, p. 201202, 2002.

[45] R. Fiederling, M. Keim, G. a. Reuscher, W. Ossau, G. Schmidt, A. Waag, and L. Molenkamp, "Injection and detection of a spin-polarized current in a light-emitting diode," *Nature*, vol. 402, no. 6763, pp. 787–790, 1999.

[46] Y. Ohno, R. Terauchi, T. Adachi, F. Matsukura, and H. Ohno, "Spin relaxation in GaAs(110) quantum wells," *Phys. Rev. Lett.*, vol. 83, pp. 4196–4199, Nov 1999.

[47] S. Garzon, I. Žutić, and R. A. Webb, "Temperature-Dependent Asymmetry of the Nonlocal Spin-Injection Resistance: Evidence for Spin Nonconserving Interface Scattering," *Phys. Rev. Lett.*, vol. 94, p. 176601, 2005.

[48] F. J. Jedema, M. S. Nijboer, A. T. Filip, and B. J. van Wees, "Spin injection and spin accumulation in all-metal mesoscopic spin valves," *Phys. Rev. B*, vol. 67, p. 085319, 2003.

[49] T. Kimura, J. Hamrle, and Y. Otani, "Estimation of spin-diffusion length from the magnitude of spin-current absorption: Multiterminal ferromagnetic/nonferromagnetic hybrid structures," *Phys. Rev. B*, vol. 72, p. 014461, 2005.

[50] A. V. Kimel, A. Kirilyuk, P. A. Usachev, R. V. Pisarev, A. M. Balbashov, and T. Raising, "Ultrafast non-thermal control of magnetization by instantaneous photomagnetic pulses," *Nature*, vol. 435, pp. 655–657, May 2005.

[51] T. Satoh, S.-J. Cho, R. Iida, T. Shimura, K. Kuroda, H. Ueda, Y. Ueda, B. A. Ivanov, F. Nori, and M. Fiebig, "Spin Oscillations in Antiferromagnetic NiO Triggered by Circularly Polarized Light," *Phys. Rev. Lett.*, vol. 105, p. 077402, 2010.

[52] R. J. Soulen Jr., J. M. Byers, M. S. Osofsky, B. Nadgorny, T. Ambrose, S. F. Cheng, P. R. Broussard, C. T. Tanaka, J. Nowak, M. J. S, A. Barry, and J. M. D. Coey, "Measuring the Spin Polarization of a Metal with a Superconducting Point Contact," *Science*, vol. 282, p. 85, 1998.

[53] A. Einstein, "Über die von der molekularkinetischen Theorie der Wärme geforderte Bewegung von in ruhenden Flüssigkeiten suspendierten Teilchen," *Ann. Phys. (Berlin)*, vol. 322, no. 8, pp. 549–560, 1905.

[54] I. Žutić, J. Fabian, and S. Das Sarma, "Spintronics: Fundamentals and applications," *Rev. Mod. Phys.*, vol. 76, pp. 323–410, 2004.

[55] F. Jedema, H. Heersche, A. Filip, J. Baselmans, and B. Van Wees, "Electrical detection of spin precession in a metallic mesoscopic spin valve," *Nature*, vol. 416, no. 6882, pp. 713–716, 2002.

[56] J. Hamrle, T. Kimura, Y. Otani, K. Tsukagoshi, and Y. Aoyagi, "Current distribution inside Py/Cu lateral spin-valve devices," *Phys. Rev. B*, vol. 71, no. 9, p. 094402, 2005.

[57] Y. Hanaoka, K. Hinode, K. Takeda, and D. Kodama, "Increase in Electrical Resistivity of Copper and Aluminum Fine Lines," *Mater. Trans.*, vol. 43, pp. 1621–1623.

[58] J. T. Batley, M. C. Rosamond, M. Ali, E. H. Linfield, G. Burnell, and B. J. Hickey, "Spin relaxation through Kondo scattering in Cu/Py lateral spin valves," *Phys. Rev. B*, vol. 92, p. 220420, Dec 2015.

[59] M. C. Rosamond, J. T. Batley, G. Burnell, B. J. Hickey, and E. H. Linfield, "High contrast 3D proximity correction for electron-beam lithography: An enabling technique for the fabrication of suspended masks for complete device fabrication within an UHV environment," *Microelectron. Eng.*, vol. 143, pp. 5 – 10, 2015.

[60] R. M. Abdullah, A. J. Vick, B. A. Murphy, and A. Hirohata, "Spin-current signal amplification by a geometrical ratchet," *J. Phys. D: Appl. Phys.*, vol. 47, no. 48, p. 482001, 2014.

[61] R. M. Abdullah, A. J. Vick, B. A. Murphy, and A. Hirohata, "Optimisation of geometrical ratchets for spin-current amplification," *J. Appl. Phys.*, vol. 117, no. 17, 2015.

[62] Y.-H. Zhu, B. Hillebrands, and H. C. Schneider, "Signal propagation in time-dependent spin transport," *Phys. Rev. B*, vol. 78, p. 054429, 2008.

[63] T. Valet and A. Fert, "Theory of the perpendicular magnetoresistance in magnetic multilayers," *Phys. Rev. B*, vol. 48, pp. 7099–7113, 1993.

[64] F. Yang, Z. Kang, X. Chen, and Y. Xue, "Large spin accumulation signal in half-metallic Co_2MnSi based lateral spin valve devices," *J. Phys. D: Appl. Phys.*, vol. 46, no. 32, p. 325003, 2013.

[65] R. M. Abdullah, "Spin Current Amplification by a Geometrical Ratchet Effect," Ph.D. dissertation, The University of York, The Department of Electronics, The University of York, York, 2015.

[66] X. Lou, C. Adelmann, S. A. Crooker, E. S. Garlid, J. Zhang, K. S. M. Reddy, S. D. Flexner, C. J. Palmstrøm, and P. A. Crowell, "Electrical detection of spin transport in lateral ferromagnet–semiconductor devices," *Nature Phys.*, vol. 3, pp. 197–202, 2007.

[67] S. P. Dash, S. Sharma, J. C. Le Breton, J. Peiro, H. Jaffrès, J.-M. George, A. Lemaître, and R. Jansen, "Spin precession and inverted Hanle effect in a semiconductor near a finite-roughness ferromagnetic interface," *Phys. Rev. B*, vol. 84, p. 054410, 2011.

[68] E. Sosenko, H. Wei, and V. Aji, "Effect of contacts on spin lifetime measurements in Graphene," *Phys. Rev. B*, vol. 89, p. 245436, 2014.

[69] T. Sasaki, T. Oikawa, T. Suzuki, M. Shiraishi, Y. Suzuki, and K. Tagami, "Electrical spin injection into Silicon using MgO tunnel barrier," *Appl. Phys. Express*, vol. 2, no. 5, p. 053003, 2009.

[70] M. Carey and B. Gurney, "Magnetoresistive sensor based on spin accumulation effect with terminal connection at back end of sensor," 2009, U.S. Patent 7,522,392.

[71] T. Sasaki, "Spin accumulation magnetic sensor," 2012, U.S. Patent 8,339,750.

[72] D. Sato and M. Yamada, "Spin accumulation magnetic read sensor," 2014, U.S. Patent 8,717,715.

[73] T. Boone, B. Gurney, and N. Smith, "Three-terminal design for spin accumulation magnetic sensor," 2014, U.S. Patent 8,760,817.

[74] L. Berger, "Emission of spin waves by a magnetic multilayer traversed by a current," *Phys. Rev. B*, vol. 54, pp. 9353–9358, 1996.

[75] J. Slonczewski, "Current-driven excitation of magnetic multilayers," *J. Magn. Magn. Mater.*, vol. 159, no. 1–2, pp. L1 – L7, 1996.

[76] S. E. Barnes, *Spin Current*. Oxford University Press, 2012, ch. Theory of spin-motive forces in ferromagnetic structures, pp. 65–86.

[77] S. E. Russek, W. H. Rippard, T. Cecil, and R. Heindl, *Spin-Transfer Nano-Oscillators*. CRC Press, 2010.

[78] Z. Zeng, G. Finocchio, and H. Jiang, "Spin transfer nano-oscillators," *Nanoscale*, vol. 5, pp. 2219–2231, 2013.

[79] T. Kimura, Y. Otani, and J. Hamrle, "Switching Magnetization of a Nanoscale Ferromagnetic Particle Using Nonlocal Spin Injection," *Phys. Rev. Lett.*, vol. 96, p. 037201, 2006.

[80] T. Seki, Y. Hasegawa, S. Mitani, S. Takahashi, H. Imamura, S. Maekawa, J. Nitta, and K. Takanashi, "Giant spin Hall effect in perpendicularly spin-polarized FePt/Au devices," *Nature Mater.*, vol. 7, no. 2, pp. 125–129, 2008.

[81] M. Buhl, A. Erbe, J. Grebing, S. Wintz, J. Raabe, and J. Fassbender, "Lateral spin transfer torque induced magnetic switching at room temperature demonstrated by X-ray microscopy," *Sci. Rep.*, vol. 3, p. 2945, 2013.

[82] V. E. Demidov, S. Urazhdin, H. Ulrichs, V. Tiberkevich, A. Slavin, D. Baither, G. Schmitz, and S. O. Demokritov, "Magnetic nano-oscillator driven by pure spin current," *Nature Mater.*, vol. 11, no. 12, pp. 1028–1031, 2012.

[83] A. Pfeiffer, S. Hu, R. M. Reeve, A. Kronenberg, M. Jourdan, T. Kimura, and M. Kläui, "Spin currents injected electrically and thermally from highly spin polarized co2mnsi," *Appl. Phys. Lett.*, vol. 107, no. 8, 2015.

[84] A. S. Edelstein and C. R. C., Eds., *Nanomaterials: Synthesis, Properties, and*

Applications. London: IOP Publishing, 2012.

[85] W. Chen and H. Ahmed, "Fabrication of high aspect ratio silicon pillars of <10 nm diameter," *Appl. Phys. Lett.*, vol. 63, no. 8, 1993.

[86] T. H. P. Chang, "Proximity effect in electron beam lithography," *J. Vac. Sci. Tech.*, vol. 12, no. 6, pp. 1271–1275, 1975.

[87] "JEOL JBX-6300FS Specifications," http://www.jeol.co.jp/en/products/detail/JBX-6300FS.html, accessed: 23/11/2014.

[88] M. L. I. and G. R., Eds., *Handbook of Thin Film Technology*. McGraw-Hill, 1970.

[89] W. S. Boyle and P. Kisliuk, "Departure from Paschen's Law of Breakdown in Gases," *Phys. Rev.*, vol. 97, p. 255, 1955.

[90] H. Nyquist, "Thermal agitation of electric charge in conductors," *Phys. Rev.*, vol. 32, pp. 110–113, 1928.

[91] M. B. Weissman, "1/f noise and other slow, nonexponential kinetics in condensed matter," *Rev. Mod. Phys.*, vol. 60, pp. 537–571, 1988.

[92] G. Liu, S. Rumyantsev, M. S. Shur, and A. A. Balandin, "Origin of 1/f noise in Graphene multilayers: Surface vs. volume," *Appl. Phys. Lett.*, vol. 102, no. 9, pp. –, 2013.

[93] Y. Blanter and M. Büttiker, "Shot noise in mesoscopic conductors," *Phys. Rep.*, vol. 336, no. 1–2, pp. 1 – 166, 2000.

[94] S. O. Valenzuela and T. Kimura, *Spin Current*. Oxford University Press, 2012, ch. Experimental observation of the spin Hall effect using electronics nonlocal detection, pp. 227–243.

[95] R. C. Weast, M. J. Astle, and W. H. Beyer, Eds., *Handbook of Chemistry and Physics*, 64th ed. CRC Press, Inc., 1984.

[96] T. Schrefl, J. Fidler, K. J. Kirk, and J. N. Chapman, "Domain structures and switching mechanisms in patterned magnetic elements," *J. Magn. Magn. Mater.*, vol. 175, pp. 193–204, 1997.

[97] D. M. C. Nicholson, W. H. Butler, W. A. Shelton, Y. Wang, X.-G. Zhang, G. M. Stocks, and J. M. MacLaren, "Magnetic structure and electronic transport in Permalloy," *J. Appl. Phys.*, vol. 81, pp. 4023–4025, 1997.

[98] F. Casanova, A. Sharoni, M. Erekhinsky, and I. K. Schuller, "Control of spin injection by direct current in lateral spin valves," *Phys. Rev. B*, vol. 79, p. 184415, 2009.

[99] B. Dieny, "Giant magnetoresistance in spin-valve multilayers," *J. Magn. Magn. Mater.*, vol. 136, no. 3, pp. 335 – 359, 1994.

[100] S. O. Valenzuela, D. J. Monsma, C. M. Marcus, V. Narayanamurti, and M. Tinkham, "Spin Polarized Tunneling at Finite Bias," *Phys. Rev. Lett.*, vol. 94, p. 196601, 2005.

[101] S. Takahashi and S. Maekawa, "Spin injection and detection in magnetic nanostructures," *Phys. Rev. B*, vol. 67, no. 5, p. 052409, 2003.

[102] T. Y. Chung and S. Y. Hsu, "Magnetization reversal in single domain Permalloy wires probed by magnetotransport," *J. Appl. Phys.*, vol. 103, no. 7, 2008.

[103] A. Hirohata, Y. Yamamoto, B. A. Murphy, and A. J. Vick, "Non-Destructive Junction Evaluation Using Decelerated Electron Beam," *Submitted to: Nature Commun.*, 2016.

[104] A. Hirohata, "Spin motor and rotary member," 2015, U.S. Patent App. 14/420,516.

[105] C. Redondo, B. Sierra, S. Moralejo, and F. Castano, "Magnetization reversal induced by irregular shape nanodots in square arrays," *J. Magn. Magn. Mater.*, vol. 322, no. 14, pp. 1969 – 1972, 2010.

[106] D. Allwood, Private Communication, 2013.

[107] H. Ohno, "Introduction to spintronics for integrated circuit applications," Spintech VII, Chicago, 2013.

[108] H. Fangohr, D. S. Chernyshenko, M. Franchin, T. Fischbacher, and G. Meier, "Joule heating in nanowires," *Phys. Rev. B*, vol. 84, p. 054437, Aug 2011.

[109] H. Zou and Y. Ji, "The origin of high surface spin-flip rate in metallic nonlocal spin valves," *Appl. Phys. Lett.*, vol. 101, no. 8, pp. –, 2012.

[110] S. Steenwyk, S. Hsu, R. Loloee, J. Bass, and W. P. Jr., "Perpendicular-current exchange-biased spin-valve evidence for a short spin-diffusion length in Permalloy," *J. Magn. Magn. Mater.*, vol. 170, no. 1–2, pp. L1 – L6, 1997.

[111] W. Pratt, S. Steenwyk, S. Hsu, W.-C. Chiang, A. Schaefer, R. Loloee, and J. Bass, "Perpendicular-current transport in exchange-biased spin-valves," *IEEE Trans. Magn.*, vol. 33, no. 5, pp. 3505–3510, 1997.

[112] T. Kimura, T. Sato, and Y. Otani, "Temperature Evolution of Spin Relaxation in a NiFe/Cu Lateral Spin Valve," *Phys. Rev. Lett.*, vol. 100, p. 066602, 2008.

[113] S. J. Barnett, "Gyromagnetic and Electron-Inertia Effects," *Rev. Mod. Phys.*, vol. 7, pp. 129–166, 1935.

[114] M. Matsuo, J. Ieda, E. Saitoh, and S. Maekawa, "Spin current generation due to mechanical rotation in the presence of impurity scattering," *Appl. Phys. Lett.*, vol. 98, no. 24, pp. –, 2011.

[115] S. O. Valenzuela and M. Tinkham, "Direct electronic measurement of the spin

Hall effect," *Nature*, vol. 442, no. 7099, pp. 176–179, 2006.

[116] O. Mosendz, V. Vlaminck, J. Pearson, F. Fradin, G. Bauer, S. Bader, and A. Hoffmann, "Detection and quantification of inverse spin Hall effect from spin pumping in Permalloy/normal metal bilayers," *Phys. Rev. B*, vol. 82, no. 21, p. 214403, 2010.

[117] V. Vlaminck, J. E. Pearson, S. D. Bader, and A. Hoffmann, "Dependence of spin-pumping spin Hall effect measurements on layer thicknesses and stacking order," *Phys. Rev. B*, vol. 88, no. 6, p. 064414, 2013.

[118] T. Kimura, Y. Otani, T. Sato, S. Takahashi, and S. Maekawa, "Room-temperature reversible spin Hall effect," *Phys. Rev. Lett.*, vol. 98, no. 15, p. 156601, 2007.

[119] M. Morota, Y. Niimi, K. Ohnishi, D. Wei, T. Tanaka, H. Kontani, T. Kimura, and Y. Otani, "Indication of intrinsic spin Hall effect in 4 d and 5 d transition metals," *Phys. Rev. B*, vol. 83, no. 17, p. 174405, 2011.

[120] C.-F. Pai, L. Liu, Y. Li, H. Tseng, D. Ralph, and R. Buhrman, "Spin transfer torque devices utilizing the giant spin Hall effect of Tungsten," *Appl. Phys. Lett.*, vol. 101, no. 12, p. 122404, 2012.

[121] J. Kerr, "XLIII. On rotation of the plane of polarization by reflection from the pole of a magnet," *Philos. Mag. Series 5*, vol. 3, no. 19, pp. 321–343, 1877.

[122] S. Bader, "SMOKE," *J. Magn. Magn. Mater.*, vol. 100, no. 1–3, pp. 440 – 454, 1991.

[123] J. A. C. Bland, M. J. Padgett, R. J. Butcher, and N. Bett, "An intensity-stabilised He-Ne laser for measuring small magneto-optic Kerr rotations from thin ferromagnetic films," *J. Phys. E: Sci. Instrum.*, vol. 22, p. 308, 1989.

[124] D. A. Allwood, G. Xiong, M. D. Cooke, and R. P. Cowburn, "Magneto-optical Kerr effect analysis of magnetic nanostructures," *J. Phys. D: Appl. Phys.*, vol. 36, no. 18, p. 2175, 2003.

[125] J. Dutson, J. Wu, K. O'Grady, N. Woolsey, Y. Kubota, and C. Platt, "Time dependence in perpendicular media with a soft underlayer," *IEEE Trans. Magn.*, vol. 40, no. 4, pp. 2504–2506, 2004.

[126] "Thorlabs DET36a operating manual."

[127] "Hamamatsu online resources," https://www.hamamatsu.com/resources/pdf/ssd/e02_handbook_si_photodiode.pdf, accessed: 12/09/2016.

[128] M. Martens, J. Schlegel, P. Vogt, F. Brunner, R. Lossy, J. Würfl, M. Weyers, and M. Kneissl, "High gain ultraviolet photodetectors based on AlGaN/GaN heterostructures for optical switching," *App. Phys. Lett.*, vol. 98, no. 21, p. 211114, 2011.

[129] "IBM research alliance produces industry's first 7nm node test chips,"

https://www-03.ibm.com/press/us/en/pressrelease/47301.wss#release, accessed: 14/03/2016.

[130] A. Hirohata, J. Sagar, L. R. Fleet, and S. S. Parkin, "Heusler alloy films for spintronic devices," in *Heusler Alloys*. Springer, 2016, pp. 219–248.